



**MARIA ADRIANA
MENDES FREITAS**

**Filmes de conversão baseados em hidróxidos
duplos lamelares (HDLs) para proteção de ligas de
alumínio para aplicações aeroespaciais**

**Layered double hydroxide (LDH)-based
conversion films for the corrosion protection of
aluminum alloys for aerospace applications**



**MARIA ADRIANA
MENDES FREITAS**

**Filmes de conversão baseados em hidróxidos
duplos lamelares (HDLs) para proteção de ligas
de alumínio para aplicações aeroespaciais**

**Layered double hydroxide (LDH)-based
conversion films for the corrosion protection of
aluminum alloys for aerospace applications**

Dissertation submitted to the University of Aveiro to fulfil the requirements for obtaining a Master's degree in Materials Engineering, held under the scientific guidance of Prof. João Tedim, assistant professor at the Department of Materials and Ceramic Engineering, University of Aveiro, Dr. Cristina Neves, postdoctoral researcher in SECoP at CICECO, University of Aveiro, Prof. Mikhail Zheludkevich, head of the Department of Corrosion and Surface Technology, Institute of Materials Research, Helmholtz-Zentrum Geesthacht and professor at the Institute of Materials Science, Kiel University, and Dr. Maria Serdechnova, postdoctoral researcher at Helmholtz-Zentrum Geesthacht.

Dedicated to the memory of Raquel.

The jury
President

Prof. Joaquim Manuel Vieira
Full professor at the Department of Materials and Ceramic Engineering, University of Aveiro

Dr. Jorge Augusto Oliveira Carneiro
Responsible for the R&D Department at Grestel - Produtos Cerâmicos, S.A.

Dr. Cristina Sofia dos Santos Neves
Postdoctoral researcher at SECoP, CICECO, University of Aveiro

Acknowledgments

First of all, I would like to express sincere gratitude to Prof. João Tedim, Prof. Mikhail Zheludkevich, Dr. Cristina Neves and Dr. Maria Serdechnova for their invaluable guidance, patience and enthusiastic encouragement. This project could not be completed without your specific expertise and generous support.

I must also address my deepest thanks to my colleagues from SECoP group for all the help, fruitful discussions and fun times at work. I would like to especially thank Dr. Marcela Reyes, Dr. Isabel Sousa, Dr. Adelaide Salvador and Daniel Vieira for their valuable contributions.

I would like to acknowledge the people from Helmholtz-Zentrum Geesthacht that contributed to this project in one way or another, particularly Christina Charalampidou, Anissa Bouali and Dr. Eduardo Silva, who have always found time to assist me whenever I needed.

I am also grateful for all the help provided by my colleagues, professors and remaining staff from the Department of Materials and Ceramic Engineering throughout every stage of my graduate studies. Prof. Augusto Lopes and Dr. Alexandra Vale are gratefully acknowledged.

Last but not least, I thank my family and friends for the endless, wholehearted support during all these years. To my parents, brother, grandparents - and all the others I dare not mention - thank you for your immense love and understanding.

palavras-chave

AA2024, corrosão, revestimentos, pré-tratamentos, filmes de conversão, hidróxidos duplos lamelares (HDLs), proteção ativa, inibidores

resumo

As ligas de alumínio são materiais amplamente utilizados para fabrico de elementos estruturais no setor aeroespacial. Dada a constante exposição das aeronaves a ambientes hostis e a suscetibilidade das ligas de alumínio à corrosão, várias estratégias têm sido implementadas de forma a proteger estes materiais da degradação causada por fenómenos corrosivos. A medida mais comum de prevenção da corrosão em ligas de alumínio 2024-T3 consiste na aplicação de um esquema de pintura multicamada, que inclui um pré-tratamento com crómio(VI) na sua composição. Os filmes de conversão à base de crómio hexavalente têm sido bastante utilizados para promover a adesão de camadas orgânicas posteriores e conferir proteção ativa ao substrato subjacente. Apesar de serem reconhecidos como os inibidores mais eficientes para as ligas de alumínio 2024, os cromatos não são considerados seguros do ponto de vista ambiental e saúde humana. Por essa razão, a sua utilização foi rigorosamente restringida na União Europeia. A necessidade de substituir os filmes de conversão baseados nestes compostos perigosos promoveu um intenso trabalho de investigação com o objetivo de desenvolver tecnologias mais ecológicas, que igualem os revestimentos à base de Cr(VI) em termos de eficácia. Os filmes de conversão baseados em hidróxidos duplos lamelares (HDLs) encontram-se entre as alternativas mais promissoras. A sua toxicidade reduzida, biocompatibilidade e preparação económica tornam-nos potenciais substitutos dos pré-tratamentos com cromatos. Além disso, estas estruturas com capacidade de permuta aniónica podem ser utilizadas não só para libertar de forma controlada inibidores de corrosão, como também para capturar espécies aniónicas agressivas, como por exemplo iões cloreto. No entanto, para que estes sistemas possam ser implementados na indústria aeroespacial, alguns aspetos carecem de melhoria. Além da relação custo-eficácia e reduzido impacto ambiental, os filmes de HDLs devem apresentar uma cobertura uniforme do substrato, uma adesão adequada ao mesmo e propriedades inibidoras de corrosão. A implementação de camadas de HDLs como pré-tratamentos para ligas de alumínio implica a otimização das condições envolvidas na sua preparação, o que requer a análise e comparação de diferentes métodos de síntese. O principal objetivo deste trabalho consistiu no desenvolvimento de filmes de conversão baseados em Zn/Al-HDLs em ligas de alumínio 2024-T3, com funcionalidade de proteção ativa e propriedades de adesão e cobertura melhoradas. Duas metodologias foram utilizadas para a sua síntese, nomeadamente o crescimento hidrotermal e a deposição eletroquímica, de forma a otimizar os parâmetros envolvidos e comparar a qualidade dos filmes obtidos em termos de cobertura, adesão ao substrato e propriedades anti corrosão através de técnicas de caracterização apropriadas.

keywords

AA2024, corrosion, coatings, pretreatments, conversion films, layered double hydroxides (LDHs), active protection, inhibitors

abstract

Aluminum and its alloys are widely used as constructional materials in the aerospace sector. Since aircrafts are often exposed to hostile environments and their alloying additions usually make aluminum alloys more susceptible to corrosion, several strategies have been applied to protect these materials against corrosion-caused degradation. The most common measure for prevention of corrosion in aluminum alloys 2024-T3 is based on the application of three-layered paint schemes, which include chromium(VI)-based pretreatments. Cr(VI)-based conversion films have been widely used to promote the adhesion of subsequent organic layers and confer active protection to the underlying substrate. Despite being the most efficient inhibitors for AA2024-T3, chromates are considered environmentally unsafe and can also affect human health. For this reason, the use of such compounds has been restricted under EU legislation. The need to replace hazardous chromate conversion coatings has prompted intense research toward the development of "greener", equally efficient technologies. Layered double hydroxide (LDH)-based conversion coatings have been found amidst the most promising alternatives. Their low-toxicity, biocompatibility and low-cost preparation make them potential substitutes for Cr(VI)-based pretreatments. Besides, these dual-function anion-exchanger structures can be used both for releasing anionic corrosion inhibitors and entrapping aggressive anionic species, such as chlorides. However, in order for these systems to meet the performance and reliability specifications required by the aerospace industry, some aspects still require further improvement. In addition to cost effectiveness and low environmental reactivity, it is important to ensure that LDH films exhibit a uniform coverage, proper adhesion to the substrate and good anti-corrosion performance. The industrial implementation of LDH layers as pretreatments for aluminum alloys entails the optimization of the conditions involved in their preparation, which requires the analysis and comparison of different synthesis routes. The present work aimed at developing Zn/Al LDH-based conversion films on AA2024-T3 substrates, with active protection functionality and enhanced adhesion and coverage characteristics. Two synthesis methodologies were employed, namely the hydrothermal growth and the electrochemical deposition, in order to optimize the involved parameters and compare the quality of the obtained conversion films in terms of their coverage, adhesion to the substrate and anti-corrosion performance through appropriate characterization techniques.

Contents

List of figures	xv
List of tables	xix
Chapter 1: State of the Art	1
1.1. Introduction	1
1.2. Corrosion in the aerospace industry	2
1.3. Aluminum alloy AA2024-T3	3
1.4. Corrosion protection of aluminum alloys	5
1.4.1. Corrosion inhibitors	6
1.4.2. Passive corrosion protection (barrier effect)	8
1.4.3. Active corrosion protection	9
1.5. Conversion coatings	10
1.6. Alternatives to chromate-based pretreatments	11
1.7. Layered Double Hydroxides (LDHs)	12
1.7.1. Synthesis methodologies of LDHs	13
1.7.1.1. Hydrothermal synthesis	14
1.7.1.2. Electrochemical deposition	14
1.7.1.3. Ion-exchange methodology	16
1.7.2. Applications of LDHs	17
1.8. Characterization techniques	18
1.8.1. X-ray diffraction	18
1.8.2. Scanning electron microscopy/energy dispersive spectroscopy (SEM/EDS)	19
1.8.3. Electrochemical impedance spectroscopy (EIS)	19
1.8.4. Adhesion tests	22
1.9. Objectives	23
Chapter 2: Experimental section	25
2.1. Materials	25

2.2. Preparation of LDH films	25
2.2.1. Pretreatment of AA2024-T3 plates	25
2.2.2. Synthesis of LDHs	26
2.2.2.1. Hydrothermal synthesis	26
2.2.2.2. Electrochemical deposition	27
2.2.3. Intercalation of corrosion inhibitors	28
2.3. Characterization techniques	28
2.3.1. X-ray diffraction	28
2.3.2. Scanning electron microscopy/energy dispersive spectroscopy (SEM/EDS)	29
2.3.3. Electrochemical impedance spectroscopy (EIS)	29
2.3.4. Adhesion tests	29
Chapter 3: Results and discussion	30
3.1. Hydrothermal synthesis	30
3.2. Electrochemical deposition	38
3.3. Characterization of coating properties for anticorrosion applications	48
3.3.1. Films prepared by hydrothermal treatment	48
3.3.2. Films prepared by electrochemical deposition	52
Chapter 4: Holistic overview and critical analysis of the systems developed	55
Chapter 5: Concluding remarks	58
Bibliographic references	59
Annex	68

List of figures

Figure 1 Airbus A350 XWB material breakdown ⁹	3
Figure 2 Potential - pH equilibrium diagram for the aluminum-water system at 25 °C ²⁰	5
Figure 3 Schematic of the passive oxide layer formed on aluminum surface ^{adapted from 2} . (image on the left) Diagram of chloride-induced pitting activity on aluminum ^{adapted from 6} . (image on the right)	6
Figure 4 Schematic (not to scale) of the coating system used in the aerospace industry ^{adapted from 3} . (image on the left) (image on the right) Schematic of the previous coating scheme with active functionality. (image on the right)	9
Figure 5 Schematic representation of hydrotalcite 3D structure ^{adapted from 93}	12
Figure 6 Scheme of the ordered octahedral sheet in a hydroxide layer ^{adapted from 93}	13
Figure 7 Scheme of (A) an LDH crystallite and LDH films with the <i>ab</i> -planes of the hexagonal platelets (B) parallel and (C) perpendicular to the substrate ^{adapted from 96}	14
Figure 8 Schematic representation of the ion exchange reaction.	16
Figure 9 XRD diffractogram of a Zn/Al-NO ₃ LDH ⁹³	19
Figure 10 Scanning electron micrographs of (A) Zn ₂ Al-NO ₃ LDH obtained by hydrothermal synthesis ⁷⁰ (B) Mg ₂ Al(OH) ₆ (CO ₃) _{0,5} ·H ₂ O prepared by the urea method ⁹⁵	19
Figure 11 Nyquist plot ¹²⁰	20
Figure 12 Bode magnitude and phase plots for the circuit depicted in Figure 13 ¹²¹	21
Figure 13 Electrical equivalent circuit model simulating simple corroding metal/electrolyte interface ¹²¹	21
Figure 14 (A) Three-step surface pretreatment apparatus in UAVR. (B) Untreated AA2024-T3 plate. (C) Pretreated AA2024-T3 plate. (D) (F) Three-step surface pretreatment apparatus in HZG.	25
Figure 15 Schematic illustration of electrochemical deposition apparatus.	28
Figure 16 XRD patterns obtained for LDH conversion films grown on the AA2024 substrates through hydrothermal synthesis (~ 100 °C, 4 h) using solutions with distinct concentrations of Zn(NO ₃) ₂	30
Figure 17 SEM images of LDH films synthesized hydrothermally (~ 100 °C, 4 h) using solutions with distinct concentrations of Zn(NO ₃) ₂ : 5 mM (A, B), 12,5 mM (C, D), 25 mM (E, F) and 50 mM (G, H).	31
Figure 18 XRD patterns obtained for LDH conversion films grown on the AA2024 substrates through hydrothermal treatment (~ 100 °C) using solutions with different concentrations of Zn(NO ₃) ₂ , for different immersion times.	32

Figure 19 XRD patterns obtained for LDH conversion films grown on the AA2024 substrates through hydrothermal treatment (~ 100 °C) using solutions with different concentrations of Zn(NO ₃) ₂ , for shorter immersion times.	32
Figure 20 SEM images of LDH films hydrothermally grown (~ 100 °C) on AA2024 substrates using a 50 mM Zn(NO ₃) ₂ solution and different immersion times: 5 min (A, B), 30 min (C, D) and 60 min (E, F).	33
Figure 21 SEM images of LDH films hydrothermally grown (~ 100 °C) on AA2024 substrates using a 500 mM Zn(NO ₃) ₂ solution and different immersion times: 1 min (A, B) and 5 min (C, D).	33
Figure 22 XRD patterns obtained for LDH conversion films grown on the AA2024 substrates through hydrothermal treatment (~ 100 °C) using solutions with different concentrations of Zn(NO ₃) ₂ and NaNO ₃ , for different immersion times.	34
Figure 23 XRD patterns obtained for LDH conversion films grown on the AA2024 substrates through hydrothermal synthesis (~ 100 °C) using a 500 mM Zn(NO ₃) ₂ + 2500 mM NaNO ₃ solution for shorter immersion times.	35
Figure 24 SEM images of LDH conversion films grown on the AA2024 substrates through hydrothermal synthesis (~ 100 °C) using a 10 mM Zn(NO ₃) ₂ + 50 mM NaNO ₃ solution for different immersion times: 5 min (A, B) and 30 min (C, D).	35
Figure 25 SEM images of LDH conversion films grown on the AA2024 substrates through hydrothermal synthesis (~ 100 °C) using a 50 mM Zn(NO ₃) ₂ + 250 mM NaNO ₃ solution for different immersion times: 5 min (A, B) and 30 min (C, D).	36
Figure 26 SEM images of LDH conversion films grown on the AA2024 substrates through hydrothermal synthesis (~ 100 °C) using a 200 mM Zn(NO ₃) ₂ + 1000 mM NaNO ₃ solution for different immersion times: 5 min (A, B) and 30 min (C, D).	36
Figure 27 SEM images of LDH conversion films grown on the AA2024 substrates through hydrothermal synthesis (~ 100 °C) using a 500 mM Zn(NO ₃) ₂ + 2500 mM NaNO ₃ solution for different immersion times: 1 min (A, B), 5 min (C, D) and 30 min (E, F).	36
Figure 28 XRD patterns obtained for LDH conversion films hydrothermally grown on the AA2024 substrates using a 500 mM Zn(NO ₃) ₂ + 2500 mM NaNO ₃ solution for different immersion times at distinct temperatures.	37
Figure 29 XRD patterns obtained for systems (A) LDH-NO ₃ -50/250 (black line) and LDH-VO _x -50/250 (red line) and (B) LDH-NO ₃ -500/2500 (black line) and LDH-VO _x -500/2500 (red line).	38
Figure 30 XRD patterns obtained for Zn/Al LDH films electrochemically deposited from solutions A (Zn ²⁺ :Al ³⁺ ratio = 1:0.33), B (Zn ²⁺ :Al ³⁺ ratio = 1:0.5), C (Zn ²⁺ :Al ³⁺ ratio = 1:0.67) and D (Zn ²⁺ :Al ³⁺ ratio = 1:0.75) with pH = 3.8, using different potentials. The depositions were carried out at room temperature (RT) during 5 min.	39

Figure 31 XRD patterns obtained for Zn/Al LDH films electrochemically deposited from solutions A ($Zn^{2+}:Al^{3+}$ ratio = 1:0.33), B ($Zn^{2+}:Al^{3+}$ ratio = 1:0.5), C ($Zn^{2+}:Al^{3+}$ ratio = 1:0.67) and D ($Zn^{2+}:Al^{3+}$ ratio = 1:0.75), with pH = 3.8, at -1.8V and -1.9V vs Ag/AgCl. The syntheses were carried out at RT during 5 min.	40
Figure 32 SEM images of the Zn/Al LDH conversion film electrochemically deposited from solution A (pH = 3.8). The applied potential was - 1.8 V vs Ag/AgCl. The deposition was carried out in RT conditions, during 5 min.	41
Figure 33 SEM images of the Zn/Al LDH conversion film electrochemically deposited from solution C (pH = 3.8). The applied potential was - 1.9 V vs Ag/AgCl. The deposition was carried out in RT conditions, during 5 min.	41
Figure 34 XRD patterns obtained for Zn/Al LDH films electrodeposited from solutions C - 3 , C - 4.2 , D - 3 , D and D - 4.2 at -1.8 V and -1.9V vs Ag/AgCl. The syntheses were carried out in RT conditions, during 5 min.	43
Figure 35 XRD patterns obtained for Zn/Al LDH films electrodeposited from a 12.5 mM $Zn(NO_3)_2$ (pH = 3), at different applied potentials, in RT conditions, during 15 min.	44
Figure 36 SEM images of the Zn/Al- NO_3 LDH conversion film electrodeposited from a 12.5 mM $Zn(NO_3)_2$ solution (pH = 3) at an applied potential of - 1.7 V vs Ag/AgCl. The deposition was carried out in RT conditions, during 15 min.	45
Figure 37 SEM images of the Zn/Al- NO_3 LDH conversion film electrodeposited from a 12.5 mM $Zn(NO_3)_2$ solution (pH = 3) at an applied potential of - 1.9 V vs Ag/AgCl. The deposition was carried out in RT conditions, during 15 min.	45
Figure 38 XRD patterns obtained for Zn/Al LDH films electrodeposited from a 12.5 mM $Zn(NO_3)_2$ solution (pH = 3), at an applied potential of -1.8 V and -1.9 V vs Ag/AgCl, in RT conditions, during different times.	46
Figure 39 SEM images obtained for the LDH conversion film electrochemically deposited on a AA2024 substrate from a 12,5 mM $Zn(NO_3)_2$ solution (pH = 3). The deposition was carried out at - 1,8 V vs Ag/AgCl, in RT conditions, during 5 min.	47
Figure 40 XRD patterns obtained for LDH-ED-1/0.75, before (1) and after (2) anion exchange reaction.	47
Figure 41 Optical microscope images of the hydrothermally grown Zn/Al LDH films after the cross-cut test: LDH- NO_3 -50/250 (A , B and C) LDH- NO_3 -500/2500 (D , E and F).	48
Figure 42 Bode and Nyquist representations of EIS spectra acquired for AA2024-T3, LDH- NO_3 -50/250, LDH- NO_3 -500/2500, LDH- VO_x -50/250, and LDH- VO_x -500/2500 in a 0.05 NaCl solution for different immersion times.	49
Figure 43 Bode representation of EIS spectra acquired for AA2024-T3, LDH- NO_3 -50/250, LDH- NO_3 -500/2500, LDH- VO_x -50/250, and LDH- VO_x -500/2500 after 90 min and 21 days of immersion in a 0.05 NaCl solution.	50

Figure 44 Optical photographs obtained for AA2024-T3, LDH-NO ₃ 50/250, LDH-NO ₃ 500/2500, LDH-VO _x 50/250, and LDH-VO _x 500/2500 after different immersion periods in a 0.05 NaCl solution.	51
Figure 45 Optical microscope images of the system LDH-ED-1/0.75 after the cross-cut test.	52
Figure 46 Bode and Nyquist representations of EIS spectra acquired for AA2024-T3, LDH-ED-1/0.75 and LDH-ED-1/0.75-V in a 0.05 NaCl solution for different immersion times.	53
Figure 47 Bode representation of EIS spectra acquired for AA2024-T3, LDH-ED-1/0.75 and LDH-ED-1/0.75-V after 90 min and 21 days of immersion in a 0.05 NaCl solution.	53
Figure 48 Optical photographs obtained for AA2024-T3, LDH-ED-1/0.75 and LDH-ED-1/0.75-V after different immersion periods in a 0.05 NaCl solution.	54
Figure A1 XRD patterns obtained for LDH conversion films grown on the AA2024 substrates through hydrothermal synthesis (~ 100 °C, 30 min) using solutions with 50 mM Zn(NO ₃) ₂ and varying concentrations of NaNO ₃	68
Figure A2 SEM/EDS data acquired for system LDH-VO _x -50/250.	68
Figure A3 SEM/EDS data acquired for system LDH-VO _x -500/2500.	69
Figure A4 SEM images obtained for the LDH conversion film electrochemically deposited on a AA2024 substrate from a 12,5 mM Zn(NO ₃) ₂ solution (pH = 3). The deposition was carried out at – 1,8 V vs Ag/AgCl, in RT conditions, during 10 min.	69
Figure A5 SEM images obtained for the LDH conversion film electrochemically deposited on a AA2024 substrate from a 12,5 mM Zn(NO ₃) ₂ solution (pH = 3). The deposition was carried out at – 1,8 V vs Ag/AgCl, in RT conditions, during 15 min.	70
Figure A6 SEM images obtained for the LDH conversion film electrochemically deposited on a AA2024 substrate from a 12,5 mM Zn(NO ₃) ₂ solution (pH = 3). The deposition was carried out at – 1,9 V vs Ag/AgCl, in RT conditions, during 5 min.	70
Figure A7 SEM images obtained for the LDH conversion film electrochemically deposited on a AA2024 substrate from a 12,5 mM Zn(NO ₃) ₂ solution (pH = 3). The deposition was carried out at – 1,9 V vs Ag/AgCl, in RT conditions, during 15 min.	71
Figure A8 SEM/EDS data acquired for system LDH-ED-1/0.75-V.	71
Figure A9 Photograph taken after removal of the tape when performing the cross-cut test on system LDH-ED-1/0.75.	72

List of tables

Table 1 Nominal composition of AA2024-T3 alloy ²	4
Table 2 Common electrical components used in equivalent circuit models ¹²⁰	22
Table 3 Classification of cross-cut test results ^{122 123}	23
Table 4 Synthesis conditions used to hydrothermally grow LDH films on AA2024 substrates from Zn(NO ₃) ₂ solutions.	26
Table 5 Synthesis conditions used to hydrothermally grow LDH films on AA2024 substrates from Zn(NO ₃) ₂ + NaNO ₃ solutions.	27
Table 6 Composition of plating solutions A - D	28

Chapter 1: State of the Art

1.1. Introduction

The impact of corrosion, a naturally-occurring process usually affecting metallic structures, can be witnessed on a daily basis since metal alloys are nearly everywhere. Due to their unique combination of mechanical properties, production cost and low density, aluminum alloys are widely used for skinning and structural applications in the aerospace sector. Given the importance and magnitude of corrosion impact in this industry and the fact that the replacement of corroded structures is far more costly than the application of corrosion prevention measures, several strategies have been used to protect such structures against corrosion-related degradation. The most common measure for prevention of corrosion in aluminum alloys is based on the application of a three-layered paint scheme on the surface of aircraft skins and other components, which consists of a pretreatment, a primer and a topcoat. Being the most important part of any coating process, on par with surface preparation, the pretreatment is crucial to ensure proper adhesion between the substrate and the top layers. Up to the present, the most efficient pretreatments for AA2024-T3 and other aluminum alloys include chromium(VI) compounds due to their self-healing nature, ease of application and efficient/cost ratio. However, chromates are considered environmentally unsafe and, for this reason, their toxicity and carcinogenic nature outweigh their usability. Since EU legislative restrictions have enforced limitations to the use of such compounds, the development of environmentally cleaner and socially friendly approaches is a scientific and technological issue of utmost importance and intensive research has been carried out in order to replace harmful chromates with “greener”, equally efficient technologies. Conversion coatings based on layered double hydroxides (LDHs) have been found amidst the most promising candidates. These dual-function anion-exchanger structures can be used both for releasing anionic corrosion inhibitors and entrapping aggressive anionic species, such as chlorides. Their low-toxicity, biocompatibility and low-cost preparation make them potential substitutes for Cr(VI)-based coatings. However, in order for these systems to meet the performance and reliability specifications required by the aerospace industry, some aspects still require further improvement. In addition to cost effectiveness and low environmental reactivity, it is important to ensure that LDH films exhibit a uniform coverage, proper adhesion to the substrate and good anti-corrosion performance^{1 2 3 4}.

This work emerged from the necessity to bridge the gap between the industrial needs and currently existing corrosion protection systems, aiming at developing Zn/Al-VO_x LDH conversion films directly on aluminum AA2024-T3 surface, with active protection functionality and enhanced adhesion and coverage characteristics. Such films are intended to be incorporated as pre-treatment layers in anti-corrosion coating schemes used in aerospace industry in order to improve the adhesion between the substrate and the organic overcoatings. They will not only provide an additional physical barrier that isolates the substrate from corrosive environments, but also decrease the corrosion of aluminum given their active protection functionality and controlled release abilities. This feature is achieved by the intercalation of inhibiting species - e.g. vanadates - in the inorganic hosting structures. Two different synthesis methodologies of LDHs were employed in this work, namely the hydrothermal growth and the electrochemical deposition, in order to optimize the involved parameters - time, temperature, pH, among

others - and compare the quality of the obtained conversion films in terms of their coverage, adhesion to the substrate and anti-corrosion performance through appropriate characterization techniques. The active compounds were incorporated into LDHs through the anion-exchange reaction. The above-described work was developed at University of Aveiro (UAVR), in Portugal, in collaboration with Helmholtz-Zentrum Geesthacht (HZG), in Germany.

1.2. Corrosion in the aerospace industry

Corrosion is a process usually associated to metallic structures, described as the gradual degradation or loss of a material and/or its properties as a result of chemical and electrochemical reactions of its exposed surface with the surrounding environment^{3, 5}. Although this phenomenon is considered as old as the discovery of metals, it has been overlooked in the past. It was only in the last six decades that scientists and engineers gave the proper attention to this matter given the irreversible consequences and enormous costs associated with such destructive process⁶.

The general process of metallic corrosion is characterized by two half-reactions: the anodic reaction corresponds to the metal oxidation (Equation 1), whereas the cathodic reaction refers to water reduction (Equation 2 and 3) or oxygen reduction (Equations 4 and 5) and results in an increase in pH near the metallic surface. During corrosion, the occurrence of more than one reduction reaction is possible⁵.



water reduction under acidic conditions:



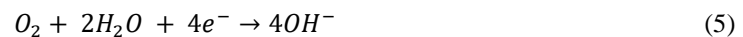
water reduction under neutral/basic conditions:



oxygen reduction under acidic conditions:



oxygen reduction under neutral/basic conditions:



Since metal alloys are nearly everywhere and the negative impact of corrosion can be witnessed on a daily basis, it is imperative to understand in depth its mechanisms in order to develop effective corrosion protection measures. It is possible to list different types of corrosion that affect the aluminum alloys. The most frequently cited include: general attack, pitting, intergranular/exfoliation, galvanic, crevice, filiform, erosion corrosion; environmentally-assisted cracking (EAC) - corrosion fatigue, stress corrosion cracking and hydrogen embrittlement -, and fretting fatigue⁷.

Today, one of the most prominent areas in which these lightweight materials play a crucial role is the aerospace industry. Due to their unique combination of mechanical properties, production cost and low density, aluminum alloys are virtually present in every sector of the aircraft, missile and spacecraft

industry. Aluminum and its alloys used onboard space vehicles are often exposed to hostile environments in emergency conditions, pre launching phase or prolonged storage for reusable spacecrafts⁴. In order to improve the properties of these alloys, it is mandatory to include certain elements in their formulation. However, such alloying additions make aluminum more susceptible to localized corrosion, specifically in media containing chlorides. Several studies proved the occurrence of severe corrosion in harsh contexts - i.e., the marine atmosphere at coastal launch sites - in the presence of intermetallic compounds such as Al_7CuFe_2 , Al_6MnFe_2 , $(\text{Al,Cu})_x(\text{Fe,Mn})_y\text{Si}$, Al_2CuMg , AlCuFeMn and $(\text{Mn,Fe})_3\text{SiAl}_{12}$ ^{2 8}. Given the importance and magnitude of corrosion impact in the aerospace industry, it is no surprise that a massive investment has been made to prevent it. Furthermore, the replacement of corroded structures is far more costly than the application of corrosion prevention measures combined with the selection of well-accepted materials².

In contrast to previous years, most of the structural elements of civil and military aircraft are currently manufactured mostly with polymeric composites. In the case of Airbus cornerstones A300 and A310, less than 5% of the total structural weight was made up of composites during their pioneering production runs. In turn, the aircraft materials of Airbus A350 XWB, the newest member of the company's wide-body family, reach a composite fraction of 52% and an aluminum/aluminum-lithium fraction of 20% (Figure 1). Nonetheless, metal alloys are still among the most common materials in the aerospace industry, namely titanium, aluminum and aluminum-lithium alloys. Whereas a large part of the fuselage is built with Carbon Fibre Reinforced Polymers (CFRP), a considerable number of structural elements remain built by aluminum alloys, such as the front fuselage, central wing box and fuselage frames. Security is one of the major priorities in this industry and several years of study and experience are required for a material to be fully accepted and applied. Aluminum has already undergone this laborious process and there is vast knowledge regarding this material, which allows it to be well established in the industry^{9 10}.

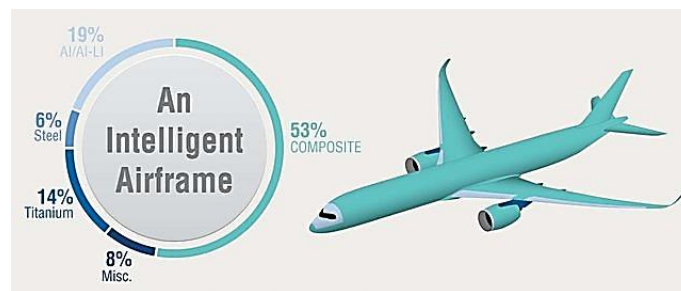


Figure 1 Airbus A350 XWB material breakdown⁹.

Since aircraft and aerospace applications require very specific features, there is a wide variety of aluminum alloys and tempers specially developed for this industry, as demonstrated in the following examples: high-purity aluminum (space mirror); 2024, alclad 2024, 7050 and 7475 sheet (wing and fuselage skin); 2024, 2124, 2314, 7050 stiffened extrusions (wing structures); 2197, 7049, 7050a and 7175 (bulkhead); 2618 (engine components), among others¹¹.

1.3. Aluminum alloy AA2024-T3

Aluminum alloy 2024-T3, the heat-treatable wrought aluminum alloy chosen as the metal substrate for this project, has been extensively used as an aircraft alloy due to its high strength, excellent resistance to fatigue and low density. The addition of alloying elements, namely copper and magnesium, and the heat treatment play a major role in the enhancement of such properties⁴. The chemical composition of the alloy is described below (Table 1).

Table 1 Nominal composition of AA2024-T3 alloy².

	Al	Cu	Mg	Mn	Si	Cr	Fe	Zn
Wt. %	98	4.4	1.5	0.6	0.5	0.1	0.5	0.25

A four-digit numerical designation system is used to classify both wrought and cast aluminum alloys according to their major alloying element, while the temper designation system – capital letter followed by one or more digits - indicates the sequence of mechanical or thermal treatments undergone by the alloy. The latter follows the former and it is separated from it by a hyphen. In the case of AA2024-T3, the first digit suggests that copper is the principal alloying addition, although other elements, such as magnesium and manganese, are also included. Regarding the 2XXX-7XXX alloys, the second digit suggests an alloy modification. If it is zero, as in the case of 2024-T3, it indicates that the alloy is the original one, while numbers from 1 to 9 are attributed successively as the original alloy undergoes modifications. The two remaining digits have no significance, serving only to distinguish the different alloys in the same group. Lastly, T3 implies the metal was heat treated and subsequently cold-worked to improve strength, and its mechanical properties were stabilized by room temperature ageing.

Although being high-strength materials, the 2XXX alloy series are less corrosion resistant when compared to alloys of other series with a significantly lower content of copper. The alloying additions cause several changes in the aluminum microstructure and consequently in its features. Despite creating a desirable combination of mechanical properties for the alloy, such inclusions may worsen other characteristics. Once added to the aluminum, these elements combine with one another and with aluminum itself to form intermetallic compounds, which can be soluble or not in the surrounding microstructure. In the case of AA2024-T3, the second-phase particles are generally Al-Cu-Mg and Al-Cu-Mn-Fe-containing phases. The former is known as S-phase, with Al_2MgCu nominal composition, while the latter is mainly represented by $\text{Al}_6(\text{Cu-Mn-Fe})$ and $\text{Al}_2\text{Cu}_2\text{Fe}$ intermetallic phases. These intermetallics usually have a distinct electrochemically activity when compared to each other and with pure aluminum. Hence, local anodic and cathodic sites in the metal are created, and the microgalvanic coupling between those heterogeneities and the matrix surrounding them contribute to the occurrence of localized corrosion. This changes the general electrochemical behaviour of the alloy and, as a result, its corrosion resistance is negatively affected. When elements like Cu and Fe are contained in such inclusions, these become more noble when compared with pure aluminum and thus act as cathodes. In turn, S-phase, which may account up to approximately 60% of the constituent particles, may behave differently. When the alloy is exposed to aggressive environments, this intermetallic compound appears to be active in respect to the matrix phase and exhibits severe dealloying. This process involves the

dissolution of the more active elements and, as a consequence, the formation of Cu-rich particle remnants, which changes the electrochemically behaviour of S-phase in AA2024 from anodic to cathodic and promotes severe localized pitting activity^{12 13 14 15 16 17 18}.

1.4. Corrosion protection of aluminum alloys

Despite being a highly reactive metal with a low standard reduction potential ($\text{Al}^{3+} + 3\text{e}^- \rightarrow \text{Al}$, $E^\circ = -1.66 \text{ V}$), aluminum owes its excellent corrosion resistance in neutral environment to the thin invisible oxide layer naturally formed on its surface. Aluminum alloys rely on this amorphous oxide film as a self-protection characteristic against corrosion when exposed to atmosphere, in normal conditions. However, this protective layer can be destroyed when in contact with specific substances or under such conditions that self-repair cannot occur and corrosion takes place.

The theoretical potential - pH domains for immunity, corrosion, and passivation of aluminum are represented on Figure 2. According to the Pourbaix diagram shown below, aluminum is protected by the hydrated aluminum oxide film in the pH range from 4 to approximately 9. It must be noted, however, that passivity of aluminum in neutral solutions can be altered under certain circumstances: the metal tends to pit in chloride-containing solutions, for example. Beyond the limits of its passive range, under highly acidic or alkaline conditions, aluminum corrodes and Al^{3+} and AlO_2^- ions are formed respectively. Corrosion rates of aluminum in the alkaline region greatly increase with pH (Al^{3+} is readily complexed by OH^- , forming AlO_2^-)^{2 19}.

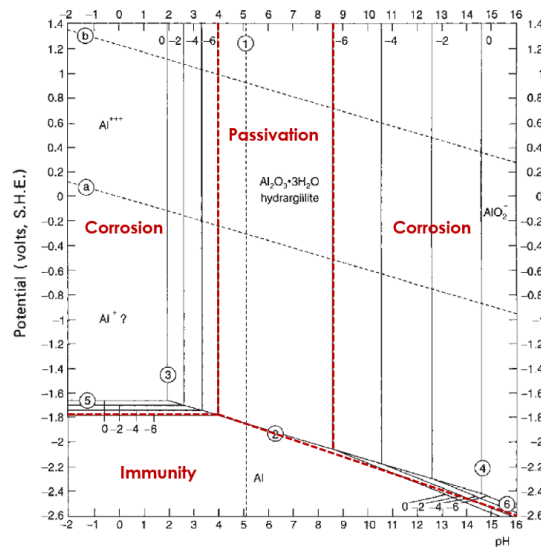


Figure 2 Potential - pH equilibrium diagram for the aluminum-water system at 25°C²⁰.

On heat-treatable alloys, the passive oxide film is generally heterogenous given the occurrence of microcracks due to rapid temperature excursions (Figure 3, image on the left), which leads to local film breakdown and the initiation of localized pitting corrosion. This form of corrosion occurs predominantly in solutions containing chlorides and affects all types of alloys, the ones containing copper being the least resistant to it. The right-hand image on Figure 3 illustrates a simplified mechanism of the pitting activity of AA2024-T3 in a chloride-containing solution.

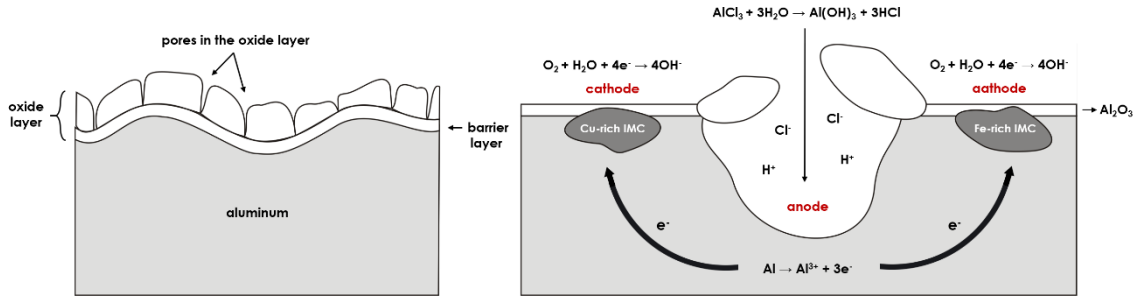


Figure 3 Schematic of the passive oxide layer formed on aluminum surface^{adapted from 2} (image on the left). Diagram of chloride-induced pitting activity on aluminum^{adapted from 6} (image on the right).

Chloride ions are known to compromise the integrity of the protective oxide layer and deteriorate its passivity. The breakdown of passivity is followed by the initiation of a localized electrochemical process, which is divided into anodic and cathodic parts. The depassivated area - the exposed metal - forms the anode where the oxidation reaction takes place. Here, electrochemically active aluminum is removed from the alloy in the form of Al^{3+} ions and electrons are transferred to the bulk alloy, which provides the electron transfer between anode and cathode. Simultaneously, the reduction of dissolved oxygen and formation of hydroxide ions occur at the more noble sites in the alloy, such as Cu- or Fe-containing intermetallic particles, which act as cathodes. In acidic solutions, however, the reaction of hydrogen evolution may also occur. As corrosion progresses, more aluminum is dissolved and the pit cavity grows. Given the high concentration of Al^{3+} cations within the pit, chlorides are attracted into it in order to maintain charge neutrality. As a consequence, hydrochloric acid is produced and the pH of the solution near the anode significantly decreases, which promotes further dissolution of aluminum. Hence, the entire process becomes autocatalytic^{5 12 21}.

The propagation of pitting further into the metal surface can lead to the occurrence of failures that may cause significant damage. Given the recurrent exposure of aircraft equipment to chlorides, the protection of aluminum alloys from pitting and other destructive types of corrosion is of utmost importance. Depending on the corrosion-causing factors and the nature of the metal to be protected, different corrosion-preventive strategies can be applied, either alone or combined. There are multiple ways to differentiate and organise them according to distinct criteria. For a better understanding of the anti-corrosion measures at play in this project, three main types will be addressed: the addition of corrosion inhibitors to corrosive media, protection schemes designed to function as physical barriers (passive protection) and the inclusion of inhibiting species on coating formulations (active protection in addition to the barrier effect).

1.4.1. Corrosion inhibitors

The corrosion rate of metals can be significantly decreased when certain chemicals are added to the corrosive medium. The inorganic and organic substances that, when added in low concentrations to the solution in contact with the exposed metal, effectively retard its corrosion are called inhibitors. In contrast to catalysts, inhibitors are spent in the partial electrochemical reactions, slowing down either or both processes (oxidation and/or reduction reactions). Inhibitors can be used at distinct pH conditions, from acid to alkaline. The chemical composition of the corrosive environment, pH, temperature and the

nature of the metal are among the critical factors determining the corrosion inhibitors efficiency. Increased inhibitor concentration generally leads to a more efficient inhibiting effect.

Inhibiting compounds can be classified differently according to different criteria. Considering their influence on the electrochemical reactions occurring when a metal is corroding, inhibitors can be classified as cathodic, passivating (anodic) or mixed type inhibitors. Cathodic inhibitors either affect the cathodic reaction itself, slowing it down, or selectively precipitate on cathodic areas, limiting the diffusion of species prone to reduction to these areas. On addition of species like calcium bicarbonate $\text{Ca}(\text{HCO}_3)_2$, zinc salts (ZnSO_4 , ZnCl_2), polyphosphates or phosphonates, the corrosion potential is displaced to more negative values. In turn, passivating (anodic) inhibitors react with the metal surface and form passive layers of oxides, hydroxides, or salts, thus suppressing the anodic reaction of metal dissolution. Hence the name “passivating” inhibitors: they cause a large anodic shift of the corrosion potential, forcing the metallic surface into the passivation range. This is the most effective and, consequently, the most frequently used type of corrosion-inhibiting compounds. They are, for instance, chromates, phosphates, silicates, nitrites, nitrates, carbonates, molybdates, borates, hydroxides and benzoates. Mixed type inhibitors affect the anodic and cathodic processes simultaneously. Inhibiting compounds can also be divided into organic or inorganic, according to their chemical nature. In general, inorganic inhibitors exhibit either cathodic or anodic action, whereas the organic ones are commonly mixed-type inhibitors. The protective mechanism of organic inhibitors is based in the formation of a hydrophobic layer of adsorbed molecules on the metallic surface, which provides a barrier against metal dissolution. The most common types of organic inhibitors include amines, amides and sulfonates. Another organisation scheme concerns the protective layer formed as a result of the interaction between the corrosion inhibiting species and the metal surface, and regroups such species as oxide-film, precipitation-film and adsorption-film type inhibitors. Oxide film inhibitors, as their name suggests, either form a passive oxide layer on the metal surface or fix the deteriorated native oxide film. Precipitation film inhibitors are compounds that cause the formation of precipitates on the metallic surface, thereby providing a protective layer. Adsorption film inhibitors are mostly organic corrosion inhibiting species that are either physisorbed and chemisorbed on the metal surface, changing its nature and inhibiting the metal corrosion.

It is very rare to use a single inhibitor. More often, a combination of different species is used in order to increase anti-corrosive effectiveness. A synergism is often observed between different inhibitors and the environment being controlled, and multi-inhibitor systems are widely used in commercial formulations. Furthermore, inhibiting compounds can be either distributed on the corrodent solution or dispersion, or included in a protective coating scheme, such as pigments in paints^{22 23 24 25}.

Up to the present, the most efficient inhibitors for AA2024-T3 and other aluminum alloys are Cr(VI) compounds. For several decades, chromate-based pretreatments and pigments have been widely applied as anti-corrosive materials for aluminum in the aerospace sector. When the exposed metal begins to corrode, released chromate ions can diffuse into the active corrosion sites and “heal” the affected area by forming a mixed layer of Cr(III) oxyhydroxides and aluminum hydroxides, thereby retarding the rate of the electrochemical process. The strong inhibiting action of chromium compounds on aluminium alloys is associated with the suppression of the localized cathodic process, which occurs on copper and iron-containing intermetallics. The application of the chromate-based coatings on the metallic substrates

is followed by the slow leaching of the chromium species, when in contact to aqueous media. Such species are responsible for healing scratches and other effects by migrating to the defected areas in the metal surface and reacting with active corroding sites. This reduces the electrochemical activity on the surface, passivating the metal. Chromate-based films protect metallic structures against corrosion so effectively that it is possible to hinder the corrosive activity even with a slight amount of chromium-containing compounds.

Nonetheless, EU legislative restrictions have enforced limitations to the use of such compounds due to their toxicity and carcinogenic nature. Although the aerospace and aeronautics industries have been exempted from EU legislation, the development of environmentally cleaner and socially friendly approaches is a scientific and technological issue of utmost importance. Since then, intensive research has been carried out in order to replace harmful chromates with “greener”, equally efficient inhibitors and inhibitor mixtures for the corrosion protection of aluminum used in aerospace structures^{3 4 2 26}. Among the possible alternatives, such as phosphates, cerium compounds and molybdates, vanadates were found to be one of the most promising candidates. Their inhibition mechanism seems to involve the formation of an adsorbed passive layer that blocks reactive sites on IMCs, and thus prevents the oxygen from being reduced. Given the clear evidence of their efficiency as corrosion inhibitors of AA2024^{27 28 29 30 31}, vanadates were the selected anions to be used in this work.

1.4.2. Passive corrosion protection (barrier effect)

Another possible strategy to protect metallic surfaces from corrosion involves the application of coating schemes that are intended to provide a physical barrier that isolates the substrate from the corrosive environment, restricting the penetration of aggressive compounds. The coating formulation generally consists of multiple layers grown or applied on a given surface in order decrease the corrosion rate of the underlying metal. Considering that any film is inhomogeneous and permeable to the electrolyte, multilayered systems are usually more effective since they decrease the porosity of the coating scheme. A uniform coverage without discontinuities, a good adhesion to the substrate, and an appropriate thickness are some of the imperative requirements to ensure an effective performance. It is also important to ensure that the coating formulation is chemically stable in various conditions and has good barrier properties (low diffusion of corrosive species). Organically-based protective schemes are the most widely used systems providing barrier protection^{3 6}.

In the aerospace industry, it is a typical procedure to apply on the surface of aircraft skins and some structural parts the three-layered scheme illustrated on Figure 4 (image on the left), which consists of a pretreatment, a primer and a topcoat. In order to achieve improved stability and adhesion, it is important to ensure that the metallic surface is homogenous and free of contaminants before the application of any film. The presence of impurities affects the adhesion of subsequent layers, which tend to delaminate, and promotes the occurrence of corrosion in the weakened interface, compromising the performance of the coating scheme. Therefore, it is crucial to ensure a thoroughly cleaned surface. The preparation of aluminum and its alloys usually involve the following steps: after cleaning the surface with an organic solvent (e.g. acetone), which removes most of organic contaminants, the metal is immersed in a mildly-inhibited alkaline bath; in order to eliminate the remaining grease and eradicate topological defects, the surface is then micro etched in an alkaline solution; once the cleaning is completed, the

surface is covered with a grey-to-black deposit, insoluble in the previous solution, which is removed by chemically etching the metal in an acidic bath. Rinsing between and after the above-mentioned stages is crucial for preventing cross-contamination from one bath to another and ensuring a complete removal of excess reagents from the treated surface^{32 33}.

On a par with the surface preparation, pretreatment plays a major role in any coating process. While the former provides a uniform, contaminant-free surface, the latter is responsible for enhancing the adhesion between the substrate and the deposited/grown films through the chemical bonds established between them. The pretreatment also serves as an additional barrier, thus providing further corrosion protection of the metal. The primer layer usually contains multi-purpose additives, such as pigments, that impart different properties to the system. It also promotes the adhesion of the subsequent topcoat, which provides an additional barrier against environmental aging and aesthetic functions⁷.

1.4.3. Active corrosion protection

The aging process of coatings under service life conditions as a result of weathering and external actions (e.g. scratches) inevitably culminate in the formation of defects. Barrier coatings fail to protect the underlying metal when the system is damaged and the unprotected surface becomes exposed to corrosive agents and aggressive media. Formulations designed for passive protection are unable to hinder the access of undesirable species to the metallic interface and, once corrosion starts, the protective layer is no longer able to protect the defective zone and prevent further propagation of the defect. Hence, an active functionality in addition to the time-limited barrier protection is crucial in order to provide long-term protection - and, consequently, longer operating life - and extension of the periods between maintenance of service parts. Coating schemes providing active protection act on the electrochemical reactions that cause corrosion, as illustrated below (Figure 4).

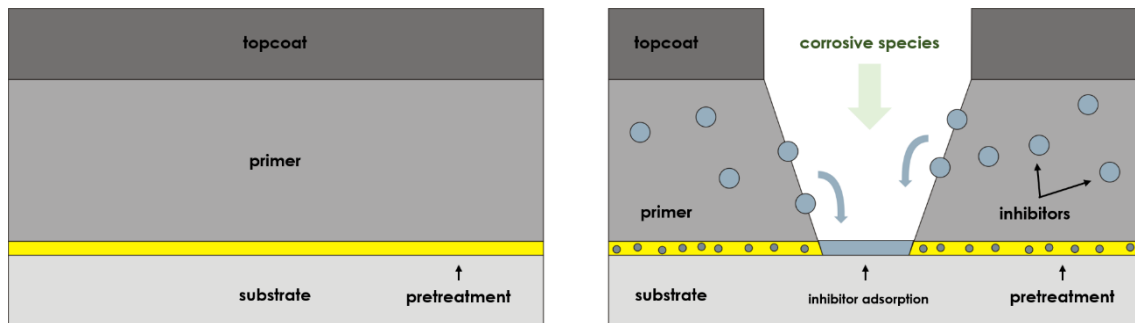


Figure 4 Schematic (not to scale) of the coating system used in the aerospace industry^{adapted from 3} (**image on the left**). Schematic of the previous coating scheme with active functionality. (**image on the right**).

As seen from the image on the right, the active protection functionality is achieved by the incorporation of corrosion inhibitors into the coating formulation. When a damage is inflicted to the protective scheme and its barrier properties fail, an environmentally induced corrosion attack takes place. As a consequence, inhibitors diffuse to the defected area and form a protective thin film, which protects the metal from further corrosion either by physically blocking or by delaying the electrochemical processes.

The growing interest in this self-repair ability after chemical or mechanical degradation, inspired by biological self-healing mechanisms, has led to the development of “smart” coatings combining passive functionality and active response to intrinsic or extrinsic stimuli (changes occurring in the coating itself, such as scratches and cracks, or in the surrounding environment, such as temperature or pH variations, respectively). Hence, this relatively recent concept emerges as the most promising approach to achieve the active protection functionality^{34 35}. Several strategies have been proposed in order to obtain systems with such characteristics. One of the reported strategies involves the addition of micro- and nanoreservoirs loaded with corrosion inhibitors in sol-gel films³⁶ or industrial organic coating formulations³⁷ in order to provide active protection on demand to the underlying substrate. A nanocontainer (or nanoreservoir) consists of a nanosized structure with active agents trapped in a porous core and/or a shell that prevent the direct contact between those substances and the surrounding environment. Thus, these structures are capable of entrapping the corrosion inhibitors and only release them when triggered by specific phenomena and/or conditions. The release of the active compounds on demand depends on specific stimuli, which range from local change of pH to simple desorption¹. However, there is a limit regarding the amount of nanocontainers that can be dispersed in the film without affecting its performance negatively and, consequently, the loading of active species in the coating is limited as well³⁵.

A study carried out by a Tedim et al.³¹ proposed a methodology based on the synergistic combination of distinct active species. The inhibition effect of the developed coatings has proved more effective than that offered by the individual systems, showing that the combination of different types of nanocontainers can be used as a route to enhance the active corrosion protection.

Another possibility regarding the encapsulation and release of inhibitors from a coating layer involves taking advantage of the intrinsic characteristics of specific polymers to capture and actively release the active species in a controlled and efficient manner (which would solve the question of low loading). In this context, Kendig and colleagues³⁸ proposed the application of inhibiting anion-doped conducting polymer coatings on aluminum alloy 2024 substrate. The authors explored the electrochemical potential of the corroding surface in order to release the active species. In other words, the electrochemical activity at the defect sites controlled the active protection. Furthermore, Zheludkevich et al.^{39 40 41 42} proposed a novel bi-layer protective coating composed of a “green” chitosan-based pre-layer covered by a sol-gel film. The former was doped with cerium cations, serving as a reservoir for the corrosion inhibitors. The obtained coating system showed well-defined self-repair properties.

Regardless of the good corrosion performance of the previously mentioned protective systems, high-performance coatings are required to meet various parameters, one of them being adhesion. As stressed earlier, the quality of the whole protective scheme relies on the surface cleaning procedures and the pretreatment. Usually, the adhesion between active metals, such as aluminum alloys, and organic coatings is enhanced through the development of an intermediate inorganic layer, namely conversion films³⁵.

1.5. Conversion coatings

The term conversion coatings describes *in-situ* formed adherent surface layers, which are so-called because they convert the naturally-produced oxide layer into a thin layer with distinct chemical and structural properties. These intermediate layers are the result of a chemical reaction that takes place between selected reagents in solution and the metallic surface. The resultant barrier, which must be more chemically and structurally resistant to dissolution by corrosive agents, is responsible for reducing the active surface area and, consequently, delaying the transport of aggressive species. This ultimately prevents the formation of corrosion cells and strengthens the whole protective system.

There is a multitude of reasons why conversion films are an excellent option when it comes to increase corrosion resistance of metallic substrates, especially when allied to organic coatings: besides promoting the adhesion of overcoatings, they also act as electrically insulating barrier layers and provide active corrosion inhibition by lowering the rate of the oxygen reduction reaction or by passivating the metallic substrate.

As already stated, there are different varieties of conversion coatings, namely phosphate, oxide and chromate coatings. Regarding their resistance, chromate-based pretreatments are far superior when compared to either oxide or phosphate coatings and are currently the most prevalent treatment in use due to their self-healing nature, ease of application and efficient/cost ratio^{3 2 24}. However, the same properties that make chromium compounds superior corrosion inhibitors also make them environmentally unsafe and, for this reason, the toxicity of chromates outweighs their usability. Therefore, it is fundamental to find viable alternative surface treatments that meet the performance and reliability specifications required by the aerospace industry, in order to bridge the gap between the industrial needs and currently existing corrosion protection systems^{4 26}.

1.6. Alternatives to chromate-based pretreatments

The great need to replace chromate conversion coatings has prompted research toward less toxic or more eco-friendly technologies capable of promoting adhesion of subsequent organic layers and providing active corrosion protection to distinct metallic substrates. Among the several “greener” protective schemes that have been proposed over the past few years are chromate-free chemical conversion coatings based on cerate^{43 44 45 46 47 48 49}, phosphates^{50 51}, permanganates,^{52 53 54 55} and fluozirconate and fluotitanate^{56 57 58}. Vanadates⁵⁹ and cerium salts^{43 44 60 61 62 63} were studied as alternative pretreatment candidates for systems with active protection functionality. Molybdates were also considered as possible less toxic corrosion inhibitors for aluminum^{64 65 66}.

In this context, Layered Double Hydroxides (LDHs) have been investigated as potential replacement for Cr(VI)-based protective coatings since the publication of the pioneering works of Buchheit and colleagues^{67 68 69}. LDHs are dual-function anion-exchanger structures that can be used both for releasing anionic corrosion inhibitors and entrapping aggressive anionic species, such as chlorides¹. LDHs have drawn a great deal of attention to their composition, ability to store different functional species and impact on the barrier properties of hybrid and organic coatings. Among their overall strengths, one can highlight their low-toxicity, biocompatibility and low-cost preparation^{34 70}. The

formation of LDHs-based conversion films on distinct metal substrates, namely aluminum^{35 71 72 73 74 75 76 77}, magnesium^{78 79 80 81}, steel⁸² and zinc⁸³, have been reported by several authors. The following chapters provide a briefly review on layered double hydroxides' chemical and structural properties, synthesis methodologies and applications.

1.7. Layered Double Hydroxides (LDHs)

Layered double hydroxides (LDHs) have been known for over 150 years since the discovery in 1842 of the first natural mineral belonging to this family of materials – hydrotalcite. Its stoichiometry, $[\text{Mg}_6\text{Al}_2(\text{OH})_{16}]\text{CO}_3 \cdot 4\text{H}_2\text{O}$, was first correctly determined by Manasse⁸⁴ in 1915 and the initial studies on the synthesis, stability, solubility and structure determination of these layered materials date back to 1930 and were mainly performed by Feitknecht⁸⁵. The major structural characteristics of LDHs were only disclosed in the 1960s through the crystal X-ray diffraction (XRD) studies on mineral samples carried out by Allmann⁸⁶ and Taylor^{87 88}. Although the basic features regarding their structure are clearly determined, detailed structural aspects remain the subject of debate in the literature. The endless possibilities concerning the composition of LDHs reflects on the wide variety of properties and applications that can be assigned to different materials. A proper understanding of both structural chemistry of LDHs and the kinetics involved in their formation process makes it possible to develop distinct materials with unique properties specially tailored for specific purposes.

LDHs are crystalline inorganic structures composed by the stacking of positively-charged, mixed-metal hydroxides ($\text{M}(\text{OH})_2$ brucite-like layers), intercalating charge-balancing anionic species and water molecules as shown in Figure 5. The metal cations have similar radii and are coordinated by six oxygen atoms forming the octahedral units, which stack together by hydrogen bonding between the hydroxyl groups of adjacent sheets^{89 90 91 92}.

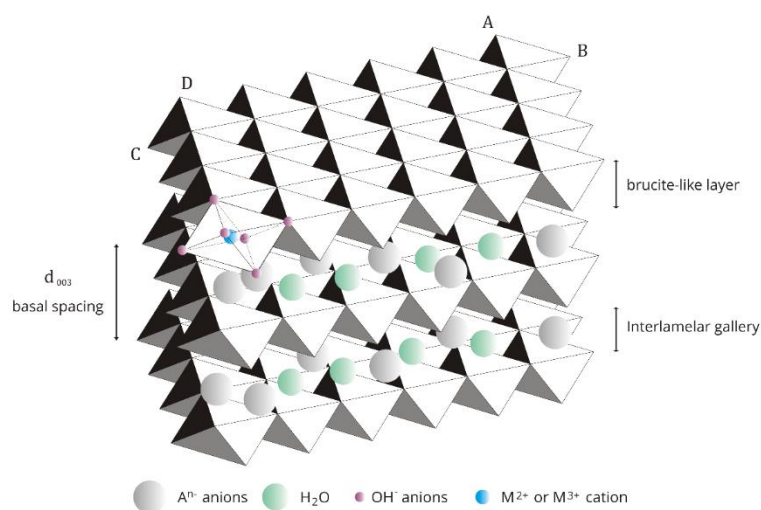


Figure 5 Schematic representation of hydrotalcite 3D structure^{adapted from 93}.

Figure 6 displays a schematic representation of the ordered octahedral sheet in a brucite-like layer. Each alternate shaded triangle contains a central cation. The parameter a (or b) denotes the distance between immediate OH^- ions in the same side layer or between two nearest metal cations (equivalent to the length AB in Figure 5) and usually falls within the range of 0.30 to 0.31 nm⁹³.

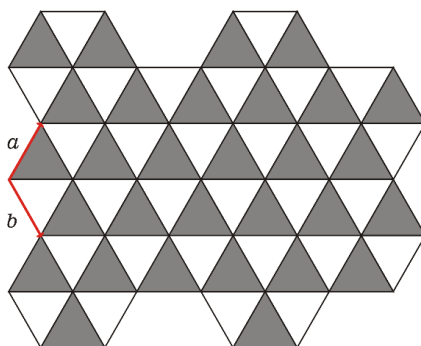
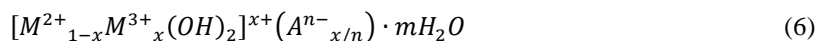


Figure 6 Scheme of the ordered octahedral sheet in a hydroxide layer^{adapted from 93}.

The electrostatic interactions and hydrogen bonds between the layers and the content of the interlamellar space are responsible for keeping the layers together⁹⁰.

The countless possibilities regarding the identity and relative proportions of the di- and trivalent cations, as well as the identity of the interlayer ions translate into the wide diversity of materials described by the following generic formula:



where, M^{2+} and M^{3+} represent the divalent and trivalent cations (whose ionic radius is not significantly different from that of Mg^{2+}); x is the ratio between di- and trivalent metals $M^{3+}/M^{2+} + M^{3+}$; A^{n-} is any charge compensating anion (organic or inorganic) with the valence n , and m is the amount of water present in the interlamellar region⁸⁹.

In LDHs, the interlamellar domain consists mostly of various anions and water molecules. There is almost no limitation when it comes to the nature of such anions, as long as these species do not abstract the metal cations from the brucite-like layers. The anions can be incorporated into the interlayer region during the formation of the lamellar structure, or by further anionic exchange, given the exchangeability of these charge-compensating compounds, which act as pillars between hydroxide layers. Also noteworthy is the influence of the ionic radii of such anions in the thickness of the interlayers since different effective diameters determine different thickness values⁹⁰⁻⁹³. The interactions between the guests and the host structure - respectively, anions and hydroxide layers - are based on electrostatic interactions and hydrogen bonding between the OH^- surface groups and the anionic species⁹⁵.

1.7.1. Synthesis methodologies of LDHs

As mentioned previously, LDHs are natural-occurring materials, although they can also be obtained synthetically. Hydrotalcite was first synthesized in laboratory in 1942 by Feitknecht⁸⁵, 100 years after it was first reported by Hochstetter⁹⁴. Over the last 80 years, several synthetic techniques have been successfully employed in order to prepare LDHs, either in a powdered form or as thin films on various substrates. The fabrication of these layered structures into films can be achieved through a physical deposition procedure or an *in situ* growth method. The former is a two-step approach that involves the preparation of LDHs crystallites in suspension *via* the conventional coprecipitation route, for instance, and the subsequent generation of the corresponding film using appropriate deposition techniques, such as

layer-by-layer (LBL) assembly, sol-gel spin-coating and the solvent evaporation technique. Despite being very flexible, in that there are no major limitations regarding the LDH composition and the identity of the underlying material, such methods produce films with poor adhesion between the LDH crystallites and the substrate. Films grown *in situ*, in turn, exhibit better adhesion to the substrate due to the chemical bonding between the two phases. One-step *in situ* methods are also not limited by the shape of the substrate.

LDH crystallites tend to exhibit a hexagonal platelet morphology. As depicted in the scheme below (Figure 7 - A), the *ab*-face of each hexagon is much bigger than its thickness (*c*-axis). While LDH films prepared by physical deposition methods are usually oriented with the *ab*-plane of the crystallites parallel to the substrate, the ones obtained through *in situ* techniques tend to grow with their *ab*-face perpendicular to the substrate (Figure 7 - B and C)⁹⁶.

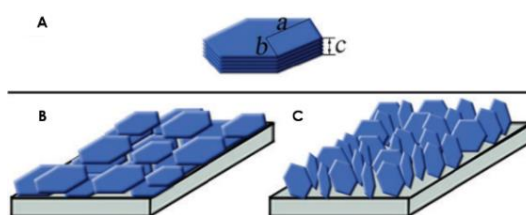


Figure 7 Scheme of (A) an LDH crystallite and LDH films with the *ab*-planes of the hexagonal platelets (B) parallel and (C) perpendicular to the substrate^{adapted from 96}.

While many other approaches have been described in literature, hereinafter emphasis will be given to those of most significance to this work, namely the hydrothermal synthesis and the electrochemical deposition, both *in situ* growth methodologies. The ion-exchange methodology will also be addressed.

1.7.1.1. Hydrothermal synthesis

The hydrothermal methodology is usually employed to obtain well-crystallized LDHs. It can be either used as a post-synthesis treatment to improve the crystallinity of LDH coprecipitated powders, or as a stand-alone procedure to obtain LDH phases with a well-defined hexagonal morphology of crystallites. It usually involves the heating of a closed stainless-steel reactor (autoclave) containing the aqueous suspension of the LDH precursor, at high temperatures, for an extended period of time. The crystallization process is highly dependent on the temperature conditions and the synthesis time^{90 97}. This well-known and established method has been used to obtain various LDH phases from distinct sources, using varying synthetic conditions^{35 70 78 98 99 100 101 102 103 104 105}.

1.7.1.2. Electrochemical deposition

Electrochemical deposition is a widely used technique to synthesize LDHs films on different substrates due to its simplicity of setup, reduced equipment cost and capability to deposit large-scale components. This methodology overcomes the limitations of other methods such as the hydrothermal growth, which requires high temperature conditions and long treatment periods. In addition to being less

time consuming, the electrochemical approach can be performed at room temperature. Besides, it allows the control of the film properties and deposition rate by current or potential bias¹⁰⁶.

Generally, electrochemical deposition involves a conventional three-electrode setup and it occurs at the interface of an electronically conductive substrate (the working electrode) and an electrolyte solution - usually a nitrate or sulfate solution - containing the appropriate metal ions to be deposited. Nitrate/sulfate-reduction process takes place concurrently with water reduction, generating hydroxide ions that elevate the local pH on the working electrode, which leads to the precipitation of the corresponding LDHs. The deposition process takes place by applying to the working electrode a specific potential in order to reduce the metal salt to its zero valent state. Typically, this methodology comprises the following phases: transfer of the metal species in solution to the substrate surface, electron transfer, formation of metal ad-atoms via adsorption, nucleation and growth of 2D or 3D metal structures and, if the growth process is not interrupted at this stage, the expansion of the 3D bulk metal phase. The main variables influencing the purity and crystallinity of the obtained LDH materials are the applied potential, the pH value of the plating solution, the metal type and the M^{2+}/M^{3+} ratio^{107 108}.

This simple and cost-effective route has been used to prepare LDHs with various compositions¹⁰⁸. Scavetta *et al.*¹⁰⁹ reported the electrodeposition of Co/Al thin films with variable thickness and Co/Al ratios. Syu *et al.*¹¹⁰ has successfully electrodeposited an optically transparent Li-Al LDH-based film on a AZ31 Mg alloy in a Li^+/Al^{3+} aqueous solution. Gupta *et al.*¹¹¹ reported the potentiostatic deposition of a nanostructured CoNi-LDH on stainless steel electrodes at -1.0 V vs. Ag/AgCl using different molar ratios of $Co(NO_3)_2$ e $Ni(NO_3)_2$ in distilled water. The electrochemical synthesis of Zn/Co-LDH films using zinc sulfate heptahydrate ($ZnSO_4 \cdot 7H_2O$) and cobalt(II) sulfate was studied by Li *et al.*¹¹².

Whereas the successful electrochemical deposition of Zn/Al- NO_3 LDHs on magnesium¹⁰⁶ and gold-coated glass¹¹³ has already been reported, it has never been performed on aluminum 2024-T3. Generally, the divalent versus trivalent cations ratio, $M^{2+}:M^{3+}$, required to prepare a well-ordered, stable LDH phase varies between 1:0.25 and 1:0.67. In the specific case of Zn/Al LDHs, the relative proportion of the Zn^{2+} and Al^{3+} cations usually ranges from 1:0.33 to 1:0.5⁹⁰. The electrodeposition of zinc-based LDHs is not straightforward since it is greatly associated with the deposition of other impurity phases, namely zinc metal, zinc oxide and zinc hydroxide. It is therefore crucial to suppress their formation in order to obtain a pure phase of Zn/Al LDH. The deposition of the LDH is achieved by reducing the nitrate ions to generate hydroxides (Equation 8). On the other hand, the reduction of Zn^{2+} will lead to the formation of zinc metal (Equation 7). The standard reduction potentials of both ions are shown below:



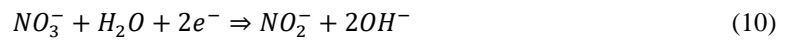
$$E_0 = -0.763 \text{ V } (-0.962 \text{ V vs Ag/AgCl 4M KCl})$$



$$E_0 = 0.01 \text{ V } (-0.189 \text{ V vs Ag/AgCl 4M KCl})$$

Since the first reaction requires a more negative potential, the selected potential must be suitable to reduce the NO_3^- ions but insufficient to reduce the Zn^{2+} . The reduction potentials may be affected by the NO_3^- and Zn^{2+} concentrations or the pH of the plating solution. Hence, it is important to consider such factors when determining the deposition potential. According to the literature^{106 113}, the purer, better ordered Zn/Al LDH phases were obtained when the deposition potential was significantly lower than those mentioned above. For that reason, the electrochemical synthesis of the LDH conversion films was performed at applied potentials ranging between -1.9 V and -1.5 vs Ag/AgCl.

As for zinc oxide, preventing its deposition is trickier given that it results from the reduction of NO_3^- , the same reaction that gives rise to the parent compound of Zn/Al LDHs, Zn(OH)_2 . The difference between their formation relies in the dehydration process, as demonstrated below:



Nonetheless, it has been proven that higher deposition temperatures promote ZnO generation¹¹³. The investigation of optimal conditions for the electrodeposition of Zn/Al-LDHs on AA2024 was therefore carried out at room temperature.

1.7.1.3. Ion-exchange methodology

LDHs are one of the most important classes of inorganic ion exchangers and their ion-exchange capacity has been extensively used to prepare several LDH phases through anionic replacement reactions. This method, first proposed by Bish¹¹⁴, is particularly useful for the preparation of non-carbonate LDHs. As the name suggests, in this approach, the guest species to be incorporated are exchanged with the interlayer anions, as schematically illustrated below (Figure 8).

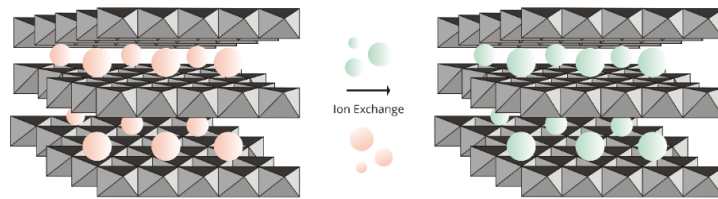


Figure 8 Schematic representation of the ion exchange reaction.

Typically, ion exchange is carried out by adding the LDH precursor to the solution containing the desired anion in excess. The extent of such reaction is determined by multiple factors, including:

1. Affinity for guest anions: the LDH precursor should contain anions with weak electrostatic interactions with the positively-charged sheets in order to facilitate the subsequent anionic exchange. In general, that exchange is favoured by higher charge densities and lower ionic radius. Thus, the easiness of such reaction for monovalent and divalent anions occurs according to the following order, respectively:

$\text{OH}^- > \text{F}^- > \text{Cl}^- > \text{Br}^- > \text{NO}_3^- > \text{I}^-$ and $\text{CO}_3^{2-} > \text{HPO}_4^{2-} > \text{SO}_4^{2-}$. Given the ease with which nitrate and chloride anions are exchanged, nitrate and chloride LDHs are commonly used as precursors for anionic exchange reactions.

2. Exchange medium: in specific solvent mediums, the interlamellar space of LDHs can be expanded to some extent, which favours the exchange process. Organic anions are more easily exchanged in organic solvents, while an aqueous medium makes it easier to exchange inorganic anions.

3. pH value: the lower the pH of the reaction solution, the weaker the interaction between interlamellar anions and the brucite-like layers. The release of the outgoing anions is therefore favoured by low pH values.

4. Chemical composition of the LDH sheets: the charge density and the hydration state of the sheets depend on their chemical composition, which in turn influence the ion exchange process.

This methodology, especially used to synthesize non-carbonate LDHs, have been applied to intercalate a wide range of organic and inorganic anions, such as: carboxylates, surfactant ions, phosphonates, β -cyclodextrin derivatives, poly(ethylene oxide) derivatives, polystyrene sulfonate, pharmaceutically active species, biomolecules, amino acids, glyphosate anions, and dye anions (organic anions); metal oxo species, polyoxometalates, phosphate ions, and metal complex ions (inorganic anions)^{89 90}.

1.7.2. Applications of LDHs

Given their high chemical versatility and anionic exchange capacity, LDHs are considered promising materials with a wide range of applications in the most diverse areas. These cationic clay-like structures represent an inexpensive, versatile and potentially recyclable source of a wide range of catalyst supports, catalyst precursors or actual catalysts⁸⁹. Some of the latest advances in the applications of LDHs in heterogeneous catalysis can be found in the review by Fan and co-workers¹¹⁵. Considering their large surface area, high anion-exchange capacities and flexible interlamellar space, which can accommodate a wide variety of materials, LDHs have been widely used to remove negatively charged species by either surface adsorption or anion-exchange. For instance, LDHs are excellent cost-effective adsorbents used in water treatment and their applications in such context have been reviewed by several authors^{116 117}. Regarding their applicability in electrochemistry, Shao and colleagues¹⁰⁸ have reported the latest developments in the design, preparation and evaluation of LDH materials toward electrochemical energy storage and conversion. As for the fields of biology and medicine, researches have focused on the incorporation and controlled release of pharmaceutically active compounds from LDH materials. Powdered LDHs have proved to be an excellent option as green carriers or hosts for genes and drugs. In addition to their biocompatibility, low (or inexistent) toxicity and alkaline character, LDHs chemical composition can vary and they have the ability to intercalate anionic drugs⁸⁹. A recent review carried out by Bi and co-workers¹¹⁸ covers some of the latest developments in the use of LDHs for controlled drug release and delivery. From a corrosion-relevant perspective, LDHs have been widely used as an effective replacement for conventional pre-treatments on industrially relevant metallic substrates. LDHs are either

utilized as smart nanocontainers/reservoirs for corrosion inhibitors that can be included as pigments in self-healing protective coatings^{27 31 119}, or as conversion layers directly grown on distinct substrates^{35 70 75 83 98 99}.

1.8. Characterization techniques

The structural features and composition of LDHs influence their physicochemical properties which, in turn, will determine the applicability of such materials. It is therefore of utmost importance to characterize these materials as fully as possible. There is a wide variety of characterization techniques that can be used to identify and analyse LDHs. This section includes a brief introduction on the basic principles of the techniques used to characterize the LDH-containing samples and the specific information provided by such tools. These are: X-Ray Diffraction (XRD), Scanning Electron Microscope (SEM), Energy Dispersive Spectroscopy (EDS), Electrochemical Impedance Spectroscopy (EIS) and adhesion tests.

1.8.1. X-ray diffraction

Among the several methods used to analyse the structure and crystal chemistry of LDHs, special mention should be made of X-ray diffraction, a tool that allows the estimation of the lattice parameters of the unit cell. Such features can be determined through the study of the position and intensity of the diffraction peaks in the obtained XRD pattern⁹⁰.

XRD patterns of preferentially ordered LDH-containing samples usually contain a set of strong basal reflections ($00l$ indices) at low angles, assuming a rhombohedral symmetry, related to the successive orders of the basal repeat distance, d_{00l} , normal to the ($00l$) plane: 003, 006, etc. For a given n -layer polytype, this basal spacing (recall Figure 5), which corresponds to the thickness of the hydroxide layer plus the interlamellar space, equals $nd(00l)$ (n, l being integers) and thus can be determined using the following formula: $d_{00l} = (d_{003} + 2d_{006} + \dots + nd_{00(3n)})/n$. Being c a multiple of d_0 , we have $c = nd_{00l}$. In the XRD patterns of non-oriented LDH-containing samples, one can find, in addition to the $00l$ reflections, nonbasal reflections (hkl indices), whose positions depend on the lattice parameters. Most LDHs, both natural and synthetic, are characterized by a hexagonal unit cell defined by the following parameters: $a = b \approx 3 \text{ \AA}$, $c = nc_0$, $\alpha = \beta = 90^\circ$, $\gamma = 120^\circ$. Such parameters can be generally determined through a couple of well-defined reflections within the interval $60\text{-}65^\circ 2\theta$ (Cu-K α radiation). Given that $a = 2d(110)$, the position of the (110) reflection at high angle - around $60^\circ 2\theta$ for Cu-K α radiation - can be used to determine the value of the parameter a , corresponding to the distance between two adjacent metal cations. Finally, the stacking pattern of the brucite-like layers can be determined through the positions of the ($01l$) and ($10l$) reflections at intermediate angles. Having determined a and c as mentioned above, one can calculate the number of layers along the unit-cell c axis using the following equation:

$$1/d^2(hkl) = 4(h^2 + hk + k^2)/3a_0^2 + l^2/c^2 \quad (13)$$

Figure 9 shows the XRD diffraction pattern of a Zn/Al-NO₃ LDH. Given the limited crystallinity of synthetic LDHs, an extensive investigation of their structure usually requires the use of distinct, complementary techniques^{89 90 93 95}.

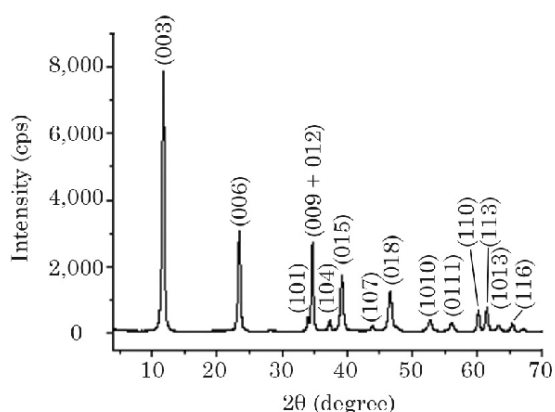


Figure 9 XRD diffractogram of a Zn/Al-NO₃ LDH⁹³.

1.8.2. Scanning electron microscopy/energy dispersive spectroscopy (SEM/EDS)

The surface characterization of LDHs can be performed by means of different techniques, being electron microscopy one of them, which allows the analysis of the shape of LDH crystallites and how they aggregate. In general, the LDH crystallization process involves the formation of hexagonal-shaped platelet-like crystals (Figure 10 - B). Whereas this morphology is typically associated with compounds containing inorganic anions, LDHs with organic interlayer species present distinct shapes and sizes, e.g., ribbon- and barlike particles. Regarding their size, the typical diameter of an LDH carbonate particle equals 1 μm. Among the several factors that affect the structural characteristics of LDH particles, one may highlight the synthesis methodology, given the influence of the reaction time, temperature, concentration of reactants, the solvent from which the material is synthesized and postpreparative treatments on the crystallinity of such structures^{90 93 95}.

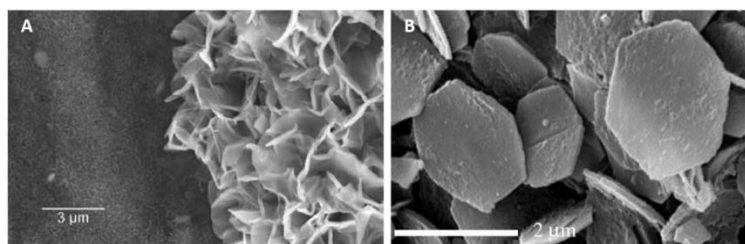


Figure 10 Scanning electron micrographs of (A) Zn₂Al-NO₃ LDH obtained by hydrothermal synthesis⁷⁰ and (B) Mg₂Al(OH)₆(CO₃)_{0.5}·H₂O prepared by the urea method⁹⁵.

In addition to high resolution images of the surface topography, it is also possible to identify the elemental composition of the analysed sample with an EDS system attached to the Scanning Electron Microscope.

1.8.3. Electrochemical impedance spectroscopy (EIS)

Among the several electrochemical methods can be used to acquire information regarding corrosion mechanisms and the efficacy of anti-corrosion systems is electrochemical impedance spectroscopy (EIS). This widely-known laboratory technique allows the determination of the corrosion rate of a metal, through the measurement of the electrical impedance of the metal-electrolyte interface when an alternating potential is applied, which in turn generates an alternating current response - hence the name AC impedance. It is commonly used to assess the efficacy of chemical inhibitors and protective films in specific environments.

EIS involves the application of a low-amplitude AC potential - typically ranging from 0.1 Hz and 100 kHz - to an electrochemical cell at a number of discrete frequencies, ω , and the subsequent measurement of the resulting current at each frequency. A low-excitation voltage is used so that the cell's response is pseudo-linear. In other words, the electric response to the sinusoidal potential will be a sinusoid with the same frequency but shifted in phase by a certain amount, the phase angle, θ , which depends on the circuit parameters. Electrochemical impedance, $Z(\omega)$, is therefore defined as the frequency-dependent, complex-valued proportionality factor between the voltage signal and the current response in a corroding cell,

$$Z(\omega) = \frac{E(\omega)}{i(\omega)} \quad (14)$$

where E is the applied potential, $E = E_0 \sin(\omega t)$; i is the current density, $i = i_0 \sin(\omega t + \theta)$; Z is the impedance ($\Omega\text{-cm}^2$); and t is the time (seconds). It is important to note that impedance is a complex number described by the frequency-dependent modulus, $|Z|$, and the phase angle, θ , or, as an alternative, by the real and imaginary components, Z' and Z'' respectively. After calculating Z as a function of frequency, one is able not only to estimate corrosion rates through the analysis of the resulting spectrum, but also to understand the underlying physicochemical processes occurring in the cell and across the corroding metal-electrolyte interface. In addition to an electrochemical cell of known geometry, impedance measurements require a reference and a counter electrodes and proper instrumentation capable of assessing and recording the electrical response over a range of AC excitation frequencies.

The impedance data obtained may be processed and presented in distinct formats. If the real and imaginary parts of the expression $Z(\omega)$ are plotted on the X- and Y-axis respectively (Z'' versus Z'), one gets a Nyquist plot (Figure 11).

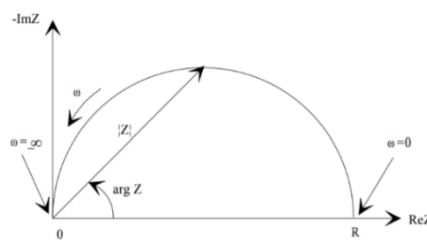


Figure 11 Nyquist plot¹²⁰.

It should be noted that, in this plot, the Y-axis is negative and that each point represents the impedance value at a specific frequency. It is, however, impossible to know what frequency was used to record each point. Low frequency figures are on the right side of the plot, whereas the higher frequency data are on the left. As shown in Figure 11, impedance can be depicted as a vector of length $|Z|$, with the phase angle, θ , being the angle formed between such vector and the X-axis ($arg Z$). While this plot contains one semicircle, which is indicative of a single “time constant”, electrochemical impedance plots usually comprise several semicircles, and that is to say, several “time constants”.

Another widespread impedance representation method is the Bode plot, where both the absolute values of impedance, $|Z|$, and the phase angle are plotted as functions of log frequency (Figure 12). Contrarily to the Nyquist plot, Bode plot displays information regarding the frequency.

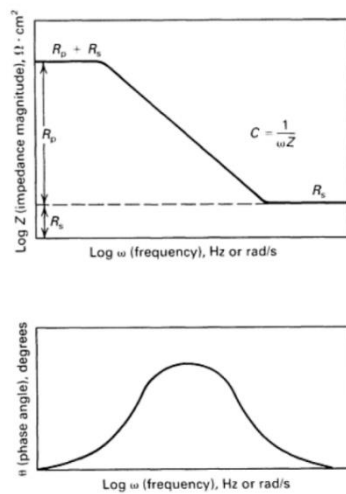


Figure 12 Bode magnitude and phase plots for the circuit depicted in Figure 13¹²¹.

The Bode plot from Figure 12 results from the electrical circuit illustrated below (Figure 13), which is the most elementary case of the equivalent electrical circuit model for an active corroding system, and comprises the solution/electrolyte resistance R_s , polarization resistance, R_p , and the double layer capacitance, C .

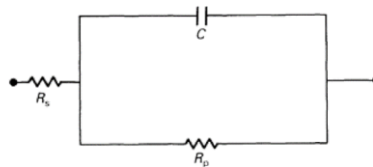





Figure 13 Electrical equivalent circuit model simulating simple corroding metal/electrolyte interface¹²¹.

Impedance data is commonly analyzed and interpreted by fitting using electrical equivalent circuits, which represent an analogy to the physical and chemical mechanisms within the studied system. The elements most commonly used in such circuits are listed in the table below (Table 2). These are trivial electrical components based on the physical electrochemistry of the cell. It is important to emphasize that most EIS models usually consist of several elements combined in a network, either in

series or in parallel, and only a few electrochemical cells can be modeled using a single equivalent circuit component.

Table 2 Common electrical components used in equivalent circuit models¹²⁰.

Element	Symbol	Current vs Voltage	Impedance
Resistor (R)		$E = IR$	$Z = R$
Inductor (L)		$E = L \frac{di}{dt}$	$Z = j\omega L$
Capacitor (C)		$I = C \frac{dE}{dt}$	$Z = \frac{1}{j\omega C}$

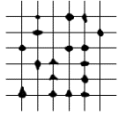
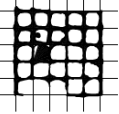
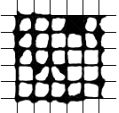
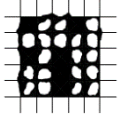
Despite the many benefits offered by this technique, there are several shortcomings to take into account: the lengthy measurement of an impedance spectrum, the need to maintain the system in study at a steady state (otherwise, unreliable results will be obtained) and the complexity involved in the analysis and interpretation of the EIS data^{19 22 120 121}.

1.8.4. Adhesion tests

The methods used to assess the adhesion between a given coating and the underlying substrate generally involve the application of either perpendicular forces at the interface plane or lateral stresses. Therefore, they can fall into one of the following categories respectively: direct pull-of methods (ISO 4624) or cross-cut methods (ISO 2409). Both procedures provide information regarding the stability of the substrate-coating bonds and how such bonds deteriorate when undergone to extraneous tensions.

The most commonly used approach to detach a coating through the application of lateral loads is the cross-cut test. This methodology involves scribing a grid pattern into the coating down to the underlying substrate, generally with a single-blade cutting tool. The number of cuts in each direction of the grid pattern must be six and their spacing, which must be equal, depends on the coating thickness and the substrate type. According to the standard specifications, the spacing of the cuts must be as follows: 1mm spacing for coatings up to 60 μm in thickness and hard substrates, 2mm spacing for coatings up to 60 μm in thickness and soft substrates, 2mm spacing for coatings ranging from 61 to 120 μm in thickness for both hard and soft substrates, and 3mm spacing for coatings ranging from 121 to 250 μm in thickness for both hard and soft substrates. In order to evaluate the obtained results and measure adhesion, one must take into account the amount of flaking, i.e., the amount of coating detached from the cross-cut surface. By doing so, it is possible to systematize results according to a six-unit classification as shown in Table 3^{122 123}.

Table 3 Classification of cross-cut test results^{122 123}.

Classification	Description	Cross-cut area
0	The edges of the cuts are smooth. No material has detached from the substrate.	-
1	Detachment of small flakes of the coating where the cuts intersect. Around 5% of the cross-cut area is affected.	
2	The coating has detached from the surface along the edges and/or the intersections of the cuts. Around 5-15% of the cross-cut area is affected.	
3	A significant part of the coating has detached from the surface along the edges of the cuts and it has flaked partly or wholly on distinct parts of the squares. Around 35% of the cross-cut area is affected.	
4	Severe detachment of material from the substrate. Around 35-65% of the cross-cut area is affected.	
5	Any degree of detachment that exceeds the amount of flaking corresponding to the previous classification. A cross-cut area greater than 65% is affected.	-

The cross-cut test has been primarily designed for determining the adhesion of organic coatings, such as varnishes and paints, applied on conversion films (or directly on the metallic substrate). However, this method has been used by some authors to assess the adhesion of LDH coatings alone^{71 72 80 106 124} and therefore it will be used here as a reference to measure the adhesion of the obtained LDH films to the AA2024-T3 substrates.

1.9. Objectives

This work aimed at developing Zn/Al-VO_x LDH conversion films directly on aluminum AA2024-T3 surface, with active protection functionality and enhanced adhesion and coverage characteristics. Such films are intended to be incorporated as intermediate layers in anti-corrosion coating formulations used in aerospace industry. The industrial implementation of LDH layers as pretreatments for aluminum alloys entails the optimization of the conditions involved in their preparation, which requires the analysis and comparison of different synthesis routes. Thus, two different methodologies were employed, namely the hydrothermal growth and the electrochemical deposition, in order to optimize the involved parameters - time, temperature, pH, among others - and compare the quality of the obtained conversion films in terms of their coverage, adhesion to the substrate and anti-corrosion performance through appropriate characterization techniques. More specifically, the main objectives of this work were:

1. Surface preparation of AA2024-T3 plates through proper cleaning procedures;

2. Hydrothermal growth of Zn/Al-NO₃ conversion films on the pretreated AA2024-T3 plates and subsequent nitrate-vanadate exchange reaction;
3. Electrochemical deposition of Zn/Al-NO₃ conversion films on the pretreated AA2024-T3 plates and subsequent nitrate-vanadate exchange reaction;
4. Structural, morphological and chemical characterization of LDH-containing samples through X-ray diffraction (XRD) and Scanning Electron Microscopy with Energy Dispersive Spectroscopy (SEM-EDS);
5. Adhesion assessment of the LDH layers through the cross-cut test;
6. Electrochemical characterization of the obtained films, before and after the intercalation of corrosion inhibitors, through Electrochemical Impedance Spectroscopy (EIS).
7. Critical analysis and comparison of the systems developed

Chapter 2: Experimental section

This chapter aims to describe the materials and methodologies used to clean and pre-treat the AA2024-T3 plates, synthesize the Zn/Al LDHs and intercalate the corrosion inhibitors, as well as the techniques utilized to characterize the LDH-containing samples.

2.1. Materials

- Aluminum alloy AA2024 plates with nominal composition of Al 90.7 - 94.7%; Mg 1.2 - 1.8%; Cu 3.8 - 4.9 %; Fe max 0.5%; Mn 0.3 - 0.9%; Si max 0.5%; Zn max 0.25%; Ti max 0.15%; Cr max 0.1%; other metals 0.20% were provided by Aero Consultants, France;

- Metaclean™ T2001, Bonderite® C-AK 4215 NC-LT AERO, Bonderite® C-AK ALUM ETCH 2 AERO (known as Turco® Aluminetch #2) and Bonderite® C-IC SMUTGO NC AERO (known as Turco Liquid Smut-Go® NC) were provided by Henkel;

- Zinc nitrate hexahydrate, $Zn(NO_3)_2 \cdot 6H_2O$, $\geq 99\%$; aluminum nitrate nonahydrate, $Al(NO_3)_3 \cdot 9H_2O$, $\geq 98,5\%$; sodium metavanadate, $NaVO_3$, $\geq 99,9\%$; sodium hydroxide, $NaOH$, $\geq 98\%$; sodium nitrate, $NaNO_3$, $\geq 99\%$ and nitric acid, NO_3 , $\geq 99.999\%$ were obtained from Sigma-Aldrich and Fluka, and used as received, without further purification.

2.2. Preparation of LDH films

2.2.1 Pre-treatment of AA2024-T3 plates

In UAVR, the pretreatment of the aluminum sheet was performed as follows: after being cut into 4×2.5 cm plates, the AA2024-T3 was surface treated using an industrial-like three-step procedure adapted from reference 31 (Figure 14). This was the selected method since it has been proved as the most effective one when compared to other laboratory-based methodologies in what concerns the removal of intermetallic particles and machined layer from the manufacturing process⁹⁸.



Figure 14 (A) Three-step surface pretreatment apparatus in UAVR. (B) Untreated AA2024-T3 plate. (C) Pretreated AA2024-T3 plate. (D) (E) Three-step surface pretreatment apparatus in HZG.

Before starting the pretreatment, the plates were cleaned with acetone in order to degrease their surface and remove particulates. The procedure involved the following steps: (1) alkaline cleaning in Metaclean™ T2001 at 60-70 °C for 15 minutes; (2) alkaline etching in Bonderite® C-AK ALUM ETCH 2 AERO at 60±5 °C for 45 seconds; (3) acid etching in Bonderite® C-IC SMUTGO NC AERO at room temperature for 7 minutes. Between each treatment, the plates were washed with deionized water, as well as in the end of the procedure. In HZG, the procedure involved the exact same steps (Figure 13 - D and F), the only differences being the chemical used for alkaline cleaning (Bonderite® C-AK 4215 NC-LT AERO) and the size of the AA2024-T3 plates (3 × 2 cm).

2.2.2. Synthesis of LDHs

2.2.2.1. Hydrothermal synthesis

The synthesis of Zn/Al-NO₃ LDH conversion films was performed through similar procedures to those described in references 35 and 70, which involved the growth of LDHs directly from the substrate through an *in situ* hydrothermal crystallization method. All the solutions were prepared with decarbonated water in an attempt to limit the intercalation of carbonate anions, which leads to the formation of carbonate-intercalated LDH structures not prone to ion-exchange reaction with most anions. The surface-treated AA2024-T3 specimens were immersed in two distinct decarbonated aqueous solutions - one containing Zn(NO₃)₂·6H₂O (pH ≈ 8, adjusted with NaOH 0.1 M) and the other Zn(NO₃)₂·6H₂O and NaNO₃ (pH ≈ 6, adjusted with NaOH 0.1 M) - under stirring-assisted hydrothermal treatment at different temperatures ($T < 100$ °C) for different time periods (Tables 4 and 5 detail all the conditions tested). Subsequently, the plates were thoroughly washed with deionized water and dried in air. The rinse stage following conversion coating is crucial to ensure the removal of precipitated salts and loosely attached film in order to improve further overcoating processes, surface wetting, and adhesion.

Table 4 Synthesis conditions used to hydrothermally grow LDH films on AA2024 substrates from Zn(NO₃)₂ solutions.

[Zn(NO ₃) ₂] (mM)	Temperature (°C)	Time (min)	pH
5	100	240	≈ 8
12.5		240	
		60	
25		120	
		240	
		5	
50		15	
		30	
		60	
		120	
		240	
500		1	
		2	
		3	
		4	
	5		

Table 5 Synthesis conditions used to hydrothermally grow LDH films on AA2024 substrates from $\text{Zn}(\text{NO}_3)_2 + \text{NaNO}_3$ solutions.

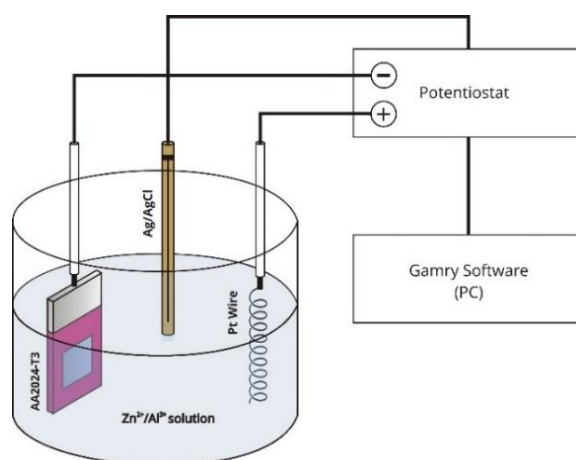
[Zn(NO ₃) ₂] (mM)	[Na(NO ₃)] (mM)	Temperature (°C)	Time (min)	pH
10	50	100	5	≈ 6
			15	
			30	
50	250	100	5	
			15	
			30	
200	1000	100	5	
			15	
			30	
500	2500	30	15	
			30	
			60	
		50	100	15
				30
				60
		80	100	15
				30
				60
				1
				2
				3
100	100	4		
		5		
		15		
			30	

2.2.2.2. Electrochemical deposition

As in the case of the hydrothermal synthesis, the electrochemical deposition was performed according to procedures found in literature (references 106 and 113) and involved two main different approaches. Firstly, the Zn/Al-NO₃ LDH conversion films were electrodeposited using an aqueous nitrate solution, prepared with deionized water, containing different ratios and concentrations of $\text{Zn}(\text{NO}_3)_2 \cdot 6\text{H}_2\text{O}$ as the Zn^{2+} source and $\text{Al}(\text{NO}_3)_3 \cdot 9\text{H}_2\text{O}$ as the Al^{3+} source, with varying pH values (Table 6). The pH of solutions A - D was adjusted by adding either HNO_3 or NaOH in order to obtain more or less acidic plating baths. A conventional three-electrode setup was used. Working electrodes were the pretreated AA2024-T3 plates. A platinum coil was used as the counter electrode, while the reference one was a Ag/AgCl electrode in a 4 M KCl solution, against which the potentials reported herein were applied (Figure 15). Potentiostatic electrodepositions were carried out at room temperature (25 - 30 °C), without stirring, using different potentials ($-1.9 \text{ V} \leq E \leq -1.5 \text{ vs Ag/AgCl 4M KCl}$) for distinct time periods (5, 10 and 15 minutes). After each deposition, the resulting surface was thoroughly rinsed with deionized water and dried under a gentle stream of hot air.

Table 6 Composition of plating solutions A - D.

Solution	[Zn(NO ₃) ₂]	[Al(NO ₃) ₃]	Zn ²⁺ :Al ³⁺ ratio	pH
A	15 mM	5 mM	1:0.33	3.8
B	15 mM	7.5 mM	1:0.5	3.8
C - 3				3
C	12.5 mM	7.5 mM	1:0.67	3.8
C - 4.2				4.2
D - 3				3
D	12.5 mM	9.4 mM	1:0.75	3.8
D - 4.2				4.2

**Figure 15** Schematic illustration of electrochemical deposition apparatus.

The second approach was similar to the previous one, the difference relying in the composition of the plating solution, which only contained 12,5 mM of Zn(NO₃)₂·6H₂O (the working electrode being the Al³⁺ source).

2.2.3. Intercalation of corrosion inhibitors

Once the LDH layers were grown in the aluminum substrates, the ion exchange was performed. Zn/Al-VO_x LDHs were obtained through the immersion of the Zn/Al-NO₃ coated specimens in a 0.1 M NaVO₃ solution with a specific pH (8-9) for 30 minutes under hydrothermal treatment (T ~ 50 °C). The solution was prepared by dissolving NaVO₃ in deionized water and adjusting the pH with 0.1 M NaOH.

2.3. Characterization techniques

2.3.1. X-ray diffraction

The phase content and crystal structure of the LDH-containing samples were evaluated through XRD analysis. In HZG, the diffraction data was collected on a PANalytical X'Pert Powder diffractometer with Ni-filtered Cu K α radiation, operating at 40 kV and 40 mA, at room temperature, with a sample rotation of 20 r.p.m. and an incident angle of 3°. The 2 θ angles were scanned over an angular range of 5

to 70°, with a step size of 0.02° and a dwell time of 1 s per increment. In UAVR, XRD analysis was performed in a Philips X'Pert diffractometer, using the same conditions.

2.3.2. Scanning electron microscopy/energy dispersive spectroscopy (SEM/EDS)

In HZG, the morphological and chemical data of the coated samples was acquired using a Tesca Vega3 SB Scanning Electron Microscope integrated with an energy dispersive X-ray microanalyzer (EDS), with an electron beam energy of 10-15 kV, a working distance ranging from 5 to 15 mm and beam intensity between 8 and 15. In UAVR, SEM/EDS measurements were performed using a Hitachi S-4100 microscope with an electron beam energy of 25 kV. Prior to imaging, the samples were coated with a thin conductive layer of gold or carbon in order to minimize charging problems.

2.3.3. Electrochemical impedance spectroscopy (EIS)

EIS measurements were performed in a three-electrode cell placed in a Faraday cage to avoid the interference of external electromagnetic fields. A platinum foil and a saturated calomel electrode were used as the counter and reference electrodes respectively, the coated aluminum sample being the working electrode (exposed area of *ca.* 1cm²). The electrolyte was a 0.05 M NaCl aqueous solution. The measurements were carried out using a Gamry FAS2 Femtostac with a PCI4 Controller. The selected frequency ranged from 10⁵ to 10⁻² Hz, with a 10 mV of sinusoidal perturbation with 7 points per frequency decade. All the spectra were recorded at open circuit potential.

2.3.4. Adhesion tests

The adhesion of the Zn/Al-NO₃ LDH conversion films was evaluated using a cross-cut test, with a TQC Cross Cut Adhesion Test KIT CC3000, according to ISO 2409. Two sets of 6 cuts with a spacing of 1 mm between each pair of adjacent blades were made perpendicularly to each other in the film, penetrating through the substrate. The resulting right-angle lattice pattern was then brushed and, lastly, an adhesive tape was applied to the cross-cut area in parallel to one of the cutting directions. The tape was rapidly removed within 300 seconds at as close to a 180° angle as possible. Evaluations were based on the visual assessment of the grid area, by rating the adhesion in accordance with the scale illustrated in Table 3. Despite the efforts to ensure the tests were carried out in a consistent manner, there may have been some variations regarding the cutting and the angle and rate of tape removal, which may have compromised the accuracy and precision of the results obtained. It is also important to note that, given the limited coated area, the test was performed only once in each sample.

Chapter 3: Results and discussion

3.1. Hydrothermal synthesis

Having the optimization of the hydrothermal growth of Zn/Al LDH films on AA2024-T3 as a primary purpose, the effect of distinct synthesis variables was investigated in order to reach the optimum conditions to produce *in situ* grown LDH layers with improved quality in terms of their coverage, adhesion and anti-corrosive properties.

Effect of zinc nitrate concentration and time of hydrothermal treatment

At first, the focus was given to the influence of the concentration of reactants. Four solutions with different concentrations of $\text{Zn}(\text{NO}_3)_2$ – 5 mM, 12.5 mM, 25 mM and 50 mM –, with a pH around 8, were then used as reaction media. The temperature was kept around 100°C during the 4-hour immersion. The XRD spectra of the resulting Zn/Al LDH conversion films are shown below (Figure 16), where the peaks ascribed to the AA2024 substrate are highlighted with an asterisk.

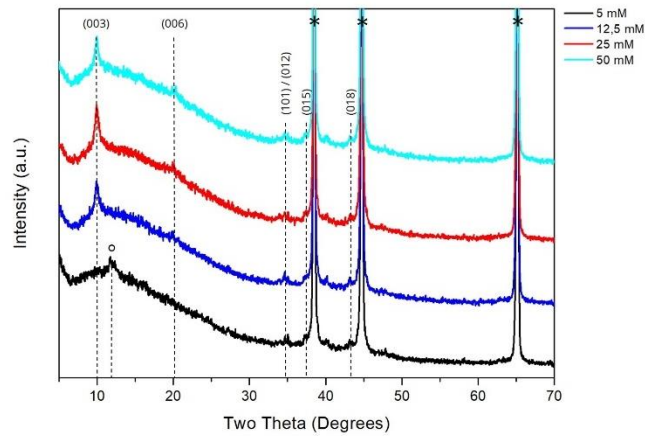


Figure 16 XRD patterns obtained for LDH conversion films grown on the AA2024 substrates through hydrothermal synthesis ($\sim 100^\circ\text{C}$, 4 h) using solutions with distinct concentrations of $\text{Zn}(\text{NO}_3)_2$.

The characteristic (003) and (006) reflections (at $2\theta \approx 10^\circ$ and $2\theta \approx 20^\circ$ respectively) suggest the presence of the nitrate-containing Zn/Al LDH when higher concentrations of $\text{Zn}(\text{NO}_3)_2$ were used. Additional peaks ascribed to the Zn/Al- NO_3 phase can also be observed at $2\theta \approx 35^\circ$, $2\theta \approx 37^\circ$ and $2\theta \approx 43^\circ$ ⁶². The non-basal peak corresponding to the (110) reflection ($2\theta \approx 60 - 65^\circ$) is possibly masked by the peaks generated by the substrate¹¹⁹. When the most diluted solution was utilized, only a small diffraction peak around $2\theta \approx 12^\circ$ (marked as **o** on Figure 16) was observed, suggesting that a CO_3 -intercalated Zn/Al LDH phase was formed⁷⁰. The morphology of the obtained conversion films was investigated by SEM and is presented in Figure 17.

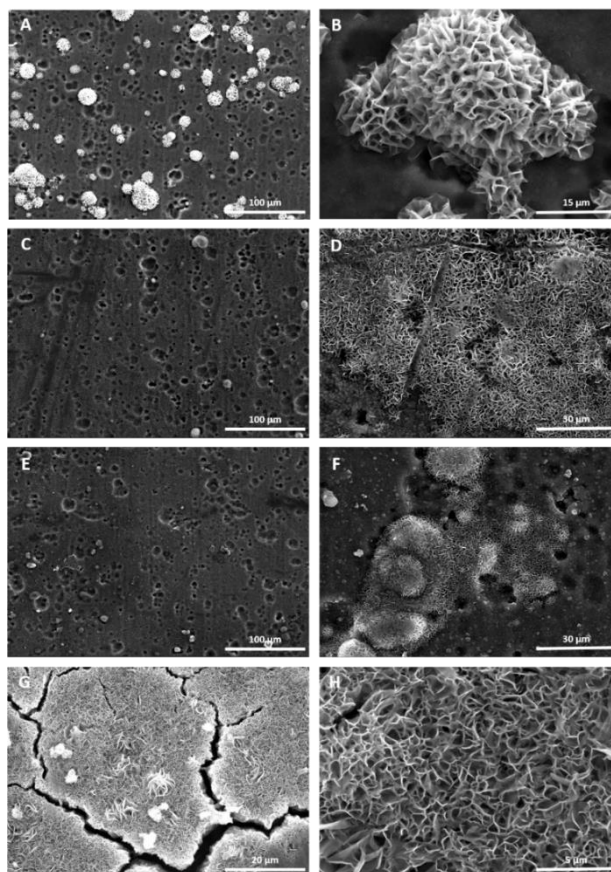


Figure 17 SEM images of LDH films synthesized hydrothermally ($\sim 100\text{ }^{\circ}\text{C}$, 4 h) using solutions with different concentrations of $\text{Zn}(\text{NO}_3)_2$: 5 mM (A, B), 12,5 mM (C, D), 25 mM (E, F) and 50 mM (G, H).

From the observation of the images above, it is possible to notice the influence of Zn^{2+} concentration in the thickness and distribution of the obtained layers. Higher Zn^{2+} concentrations led to more compact and evenly distributed films throughout the surface, whereas more diluted media seem to be associated with poorer substrate coverage by micro-sized island-like LDHs, which is consistent to the results reported in literature^{35 70 99}. The cracks observed in Figure 17 - G may be associated either with the drying process or the lateral stresses induced by the high number of platelets per unit of area or solvent evaporation under vacuum conditions during SEM analysis¹³.

Further experiments focused on the influence of time on the formation of the Zn/Al LDH films using more concentrated Zn^{2+} solutions and significantly shorter immersion times. Figures 18 and 19 illustrate the XRD patterns of the resulting coatings.

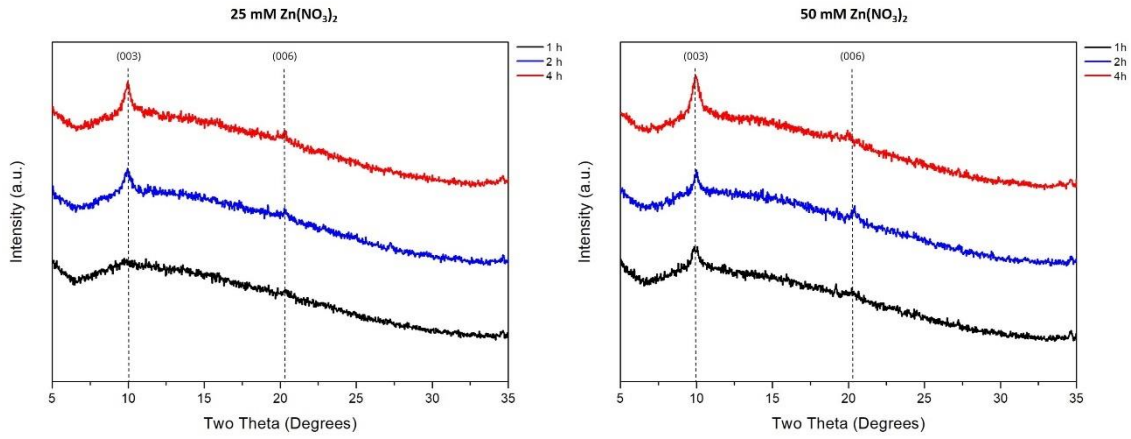


Figure 18 XRD patterns obtained for LDH conversion films grown on the AA2024 substrates through hydrothermal treatment ($\sim 100\text{ }^{\circ}\text{C}$) using solutions with different concentrations of $\text{Zn}(\text{NO}_3)_2$, for different immersion times.

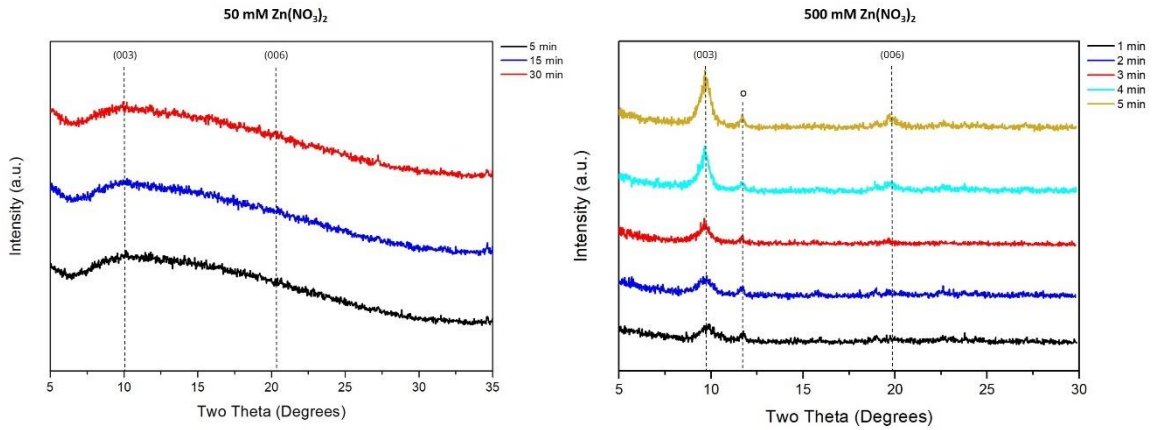


Figure 19 XRD patterns obtained for LDH conversion films grown on the AA2024 substrates through hydrothermal treatment ($\sim 100\text{ }^{\circ}\text{C}$) using solutions with different concentrations of $\text{Zn}(\text{NO}_3)_2$, for shorter immersion times.

By analysing the acquired diffraction data, it appears that as the $\text{Zn}(\text{NO}_3)_2$ concentration increases, the growth of Zn/Al LDHs becomes feasible for increasingly shorter times, which seems to be confirmed by the SEM images presented below (Figures 20 and 21). Once again, a small diffraction peak attributed to a carbonate-containing LDH is visible (highlighted as **o** on Figure 19 - B). The fact that the synthesis was performed under atmospheric conditions may have led to partial carbonation of the samples³⁵.

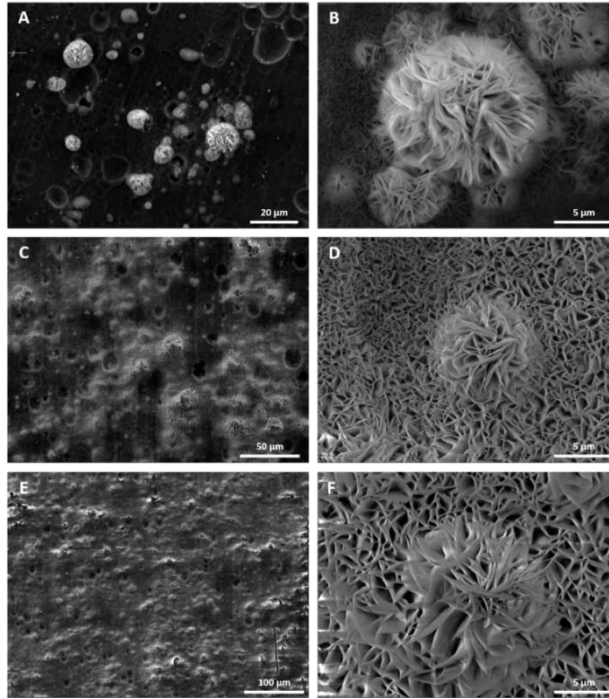


Figure 20 SEM images of LDH films hydrothermally grown ($\sim 100\text{ }^{\circ}\text{C}$) on AA2024 substrates using a 50 mM $\text{Zn}(\text{NO}_3)_2$ solution and different immersion times: 5 min (A, B), 30 min (C, D) and 60 min (E, F).

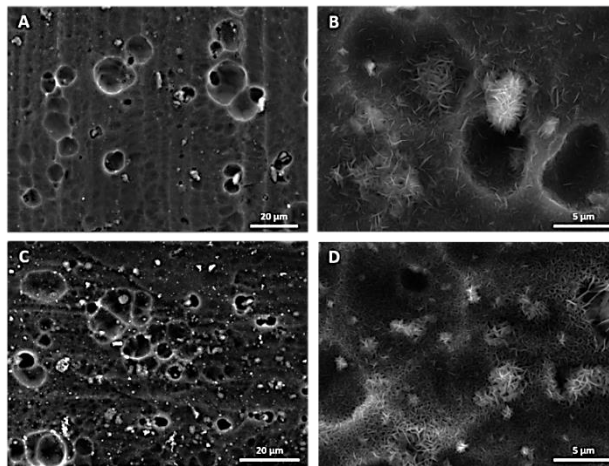


Figure 21 SEM images of LDH films hydrothermally grown ($\sim 100\text{ }^{\circ}\text{C}$) on AA2024 substrates using a 500 mM $\text{Zn}(\text{NO}_3)_2$ solution and different immersion times: 1 min (A, B) and 5 min (C, D).

It can be observed from Figure 20 – B, D and F that LDH layers can grow directly on top of the AA2024 surface as flower-like protrusions with flake morphology and that longer synthesis times lead to bigger, more developed flakes and wider coverage of the substrate. Such flower-like shape with nano-flakes is consistent with previous results reported in literature^{35 70 98 99}. On the other hand, the films depicted on Figure 21 appeared more uniformly distributed, though with underdeveloped flakes. The layers prepared under more diluted conditions or shorter times appear to be rather thin since the microstructure, in particular the “craters” resulting from the removal of intermetallics during the pretreatment are still visible (Figure 20 - A and C and Figure 21 - A - D).

As one of the major goals of this work is to achieve films with optimized adhesion properties between the substrate, LDH layer and overcoating, it was decided to privilege the formation of a less dense, thinner and evenly distributed LDH layer instead of isolated agglomerates with more developed flakes. Thus, subsequent syntheses were carried out for very short periods, with the most concentrated reaction media ($[\text{Zn}(\text{NO}_3)_2] > 50 \text{ mM}$).

Effect of sodium nitrate concentration

Sodium nitrate was added to the $\text{Zn}(\text{NO}_3)_2$ solution in order to prevent the development of phases containing anions other than NO_3^- by shifting the ion exchange equilibrium and promoting the intercalation of nitrates in the LDH interlamellar space. Also, higher NaNO_3 concentrations decrease the solubility of carbon dioxide in aqueous solutions (“salting-out effect”)¹²⁵. The lower the CO_2 concentration in solution, the lower the probability of obtaining carbonate-containing LDH phases.

After finding the most appropriate ratio between the two reactants to form the more crystalline and pure Zn/Al LDH phase (Figure A1, in the Annex) - $\text{Zn}(\text{NO}_3)_2 : \text{NaNO}_3 = 1:5$ - three solutions containing distinct concentrations of $\text{Zn}(\text{NO}_3)_2$ and NaNO_3 were used to grow the conversion coatings. Their concentration ranged from 50 to 500 mM and 250 and 2500 mM respectively and the AA2024 plates were immersed in the solutions from 1 up to 30 minutes. The temperature conditions were kept the same ($\sim 100 \text{ }^\circ\text{C}$). The diffractograms of the obtained films are presented below (Figures 22 and 23).

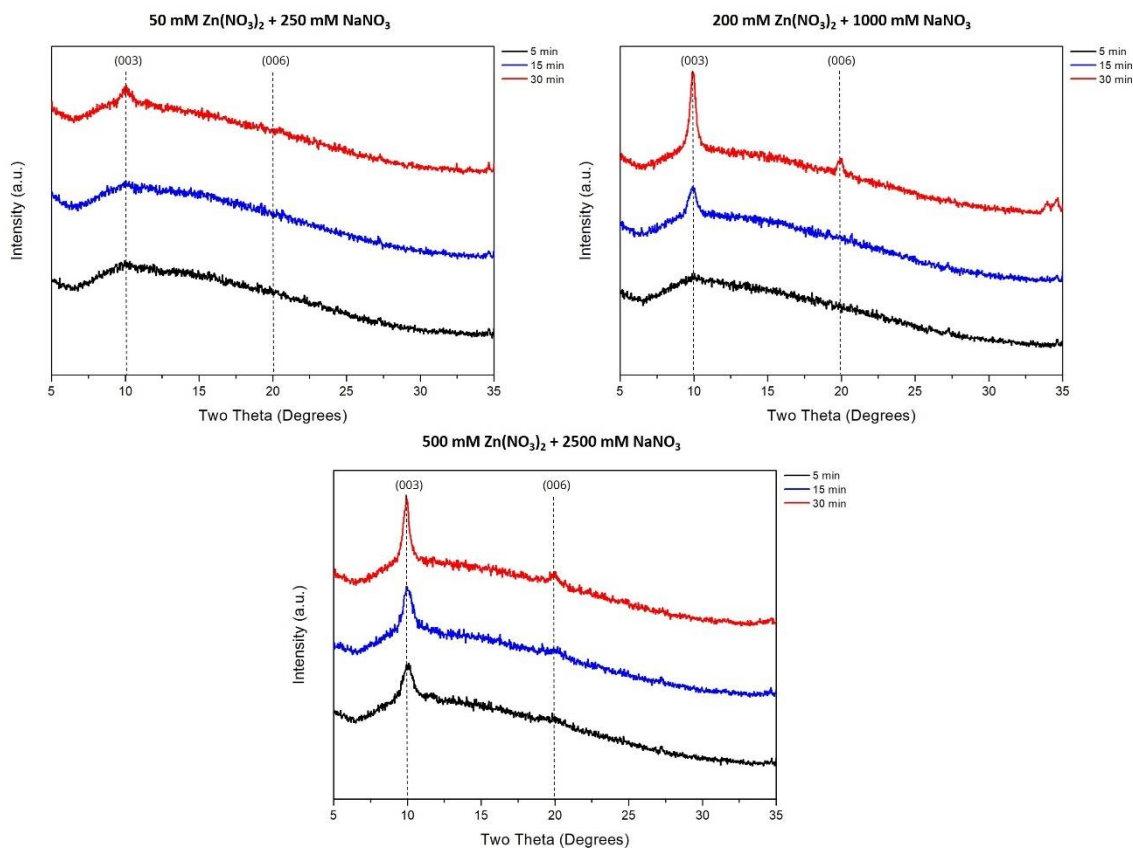


Figure 22 XRD patterns obtained for LDH conversion films grown on the AA2024 substrates through hydrothermal treatment ($\sim 100 \text{ }^\circ\text{C}$) using solutions with different concentrations of $\text{Zn}(\text{NO}_3)_2$ and NaNO_3 , for different immersion times.

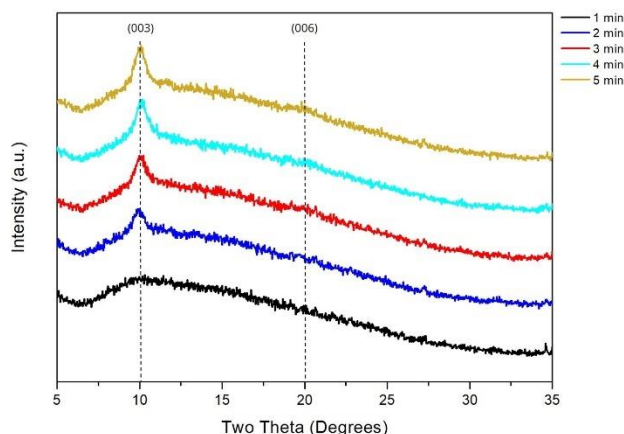


Figure 23 XRD patterns obtained for LDH conversion films grown on the AA2024 substrates through hydrothermal synthesis ($\sim 100\text{ }^{\circ}\text{C}$) using a $500\text{ mM Zn(NO}_3)_2 + 2500\text{ mM NaNO}_3$ solution for shorter immersion times.

It is clear that for such short immersion times, a $\text{Zn(NO}_3)_2$ concentration equal or superior to 200 mM is crucial to form crystalline LDH phases. The XRD spectra related to more diluted concentrations exhibit broader, less intense peaks which are seemingly associated with poorly crystallized/developed Zn/Al LDHs. Contrastingly, the films synthesized under higher concentrations of Zn^{2+} exhibit enhanced LDH peaks. Besides, the addition of NaNO_3 appears to have yielded the expected results given the absence of peaks suggesting the presence of Zn/Al LDH phases other than nitrate-intercalated ones.

In the SEM images presented below, it is possible to observe that the lamellar-like nanoplatelets are already perpendicularly oriented to the underlying substrate at an early stage of growth (Figures 24 - B and 25 - B), which is in agreement with what has been described in the literature¹⁰⁰. Moreover, Figures 26 and 27 confirm the uniform growth of a thin, defect-free LDH layer across the whole surface of the AA2024 plates, without major agglomerates, when the more concentrated solutions are used.

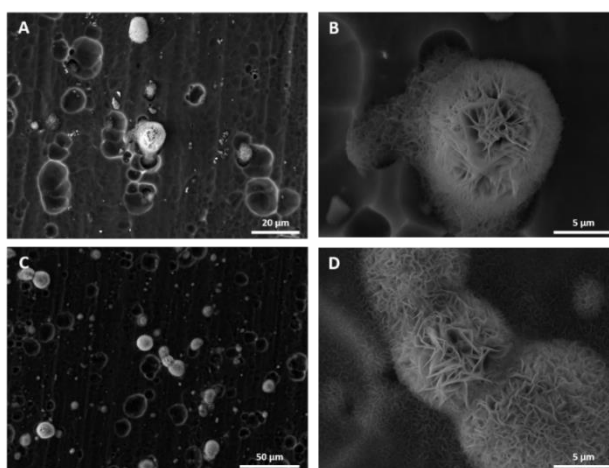


Figure 24 SEM images of LDH conversion films grown on the AA2024 substrates through hydrothermal synthesis ($\sim 100\text{ }^{\circ}\text{C}$) using a $10\text{ mM Zn(NO}_3)_2 + 50\text{ mM NaNO}_3$ solution for different immersion times: 5 min (A, B) and 30 min (C, D).

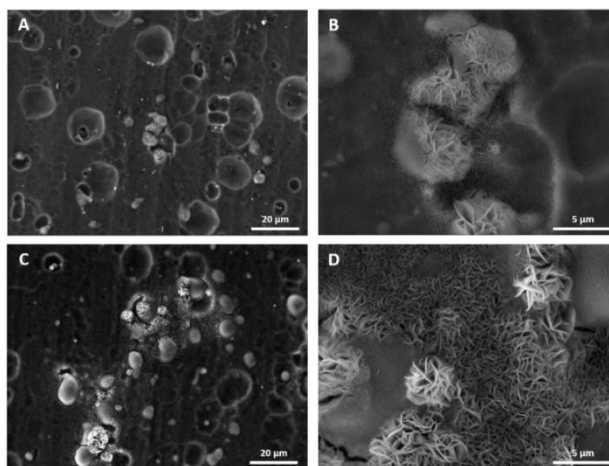


Figure 25 SEM images of LDH conversion films grown on the AA2024 substrates through hydrothermal synthesis ($\sim 100\text{ }^{\circ}\text{C}$) using a $50\text{ mM Zn(NO}_3)_2 + 250\text{ mM NaNO}_3$ solution for different immersion times: 5 min (**A, B**) and 30 min (**C, D**).

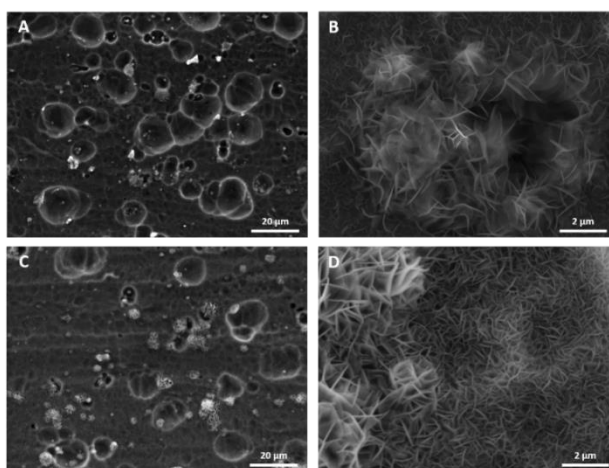


Figure 26 SEM images of LDH conversion films grown on the AA2024 substrates through hydrothermal synthesis ($\sim 100\text{ }^{\circ}\text{C}$) using a $200\text{ mM Zn(NO}_3)_2 + 1000\text{ mM NaNO}_3$ solution for different immersion times: 5 min (**A, B**) and 30 min (**C, D**).

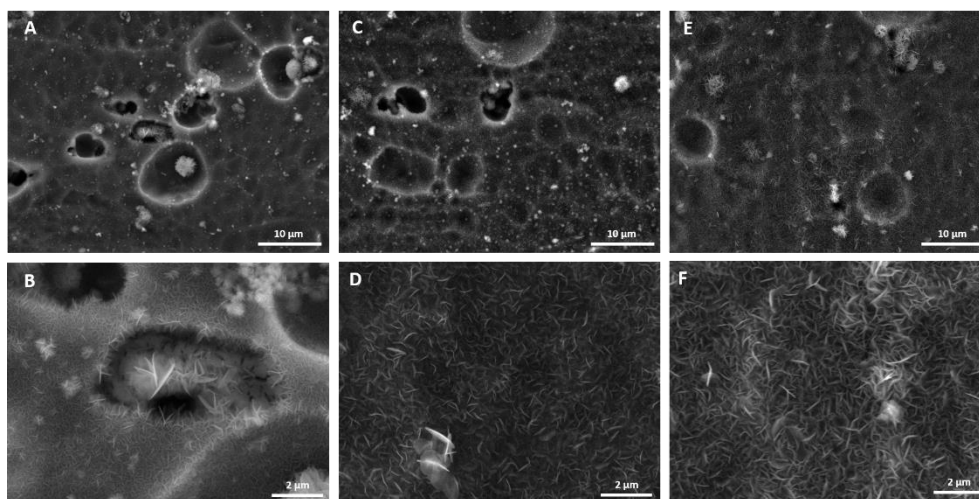


Figure 27 SEM images of LDH conversion films grown on the AA2024 substrates through hydrothermal synthesis ($\sim 100\text{ }^{\circ}\text{C}$) using a $500\text{ mM Zn(NO}_3)_2 + 2500\text{ mM NaNO}_3$ solution for different immersion times: 1 min (**A, B**), 5 min (**C, D**) and 30 min (**E, F**).

Effect of temperature during hydrothermal treatment

The influence of the bath temperature was also taken into consideration for optimization processes and, as confirmed by the diffraction data presented below (Figure 28), it has a significant effect on the growth of the Zn/Al LDHs. The more crystalline LDH phases were obtained with the combination of higher temperatures and longer immersion times, as expected. Nonetheless, it is possible to have LDH peaks with half the temperature ($T \sim 50 \text{ }^\circ\text{C}$) - and significantly shorter times (30 - 60 min) - than those normally used to hydrothermally synthesize LDH-based conversion films ($T \sim 100 \text{ }^\circ\text{C}$, 4 hours)^{35 70 98 99}, as proven by the XRD spectra in Figure 28.

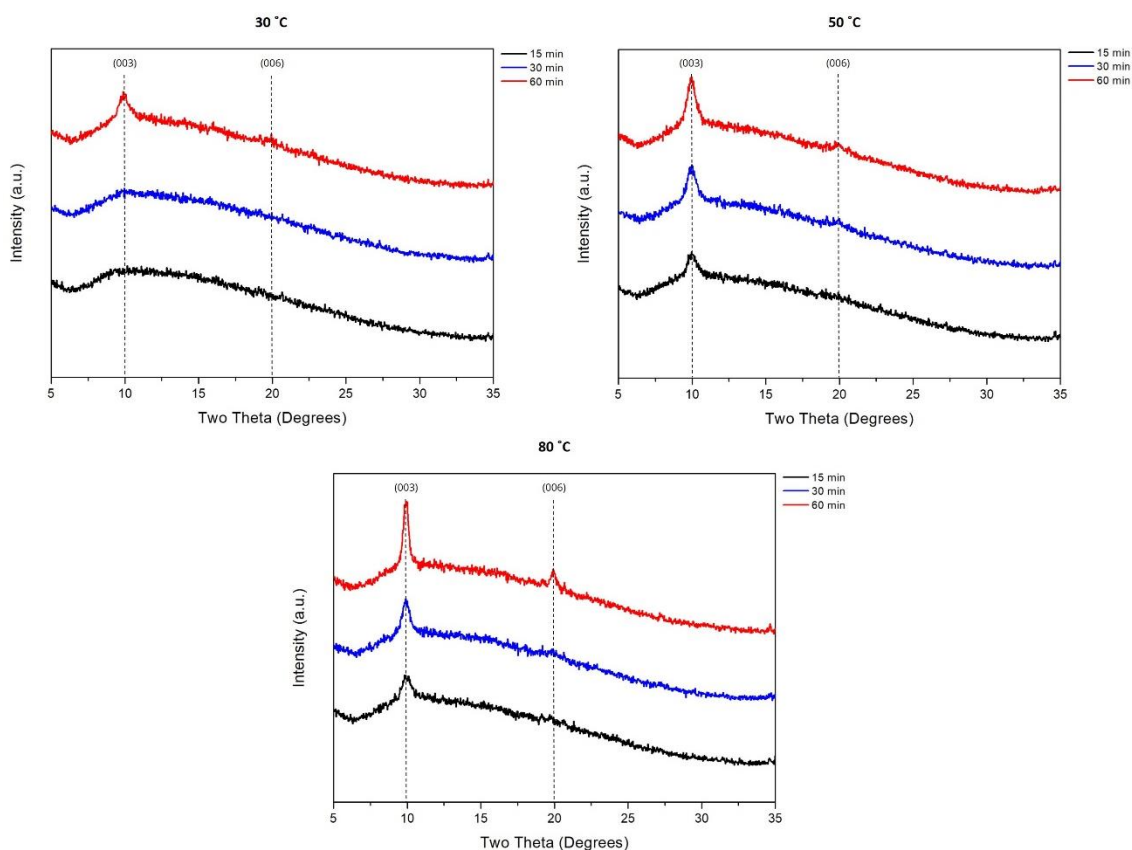


Figure 28 XRD patterns obtained for LDH conversion films hydrothermally grown on the AA2024 substrates using a 500 mM $\text{Zn}(\text{NO}_3)_2$ + 2500 mM NaNO_3 solution for different immersion times at distinct temperatures.

Intercalation of corrosion inhibitors in the LDH structure

After investigating the most favourable conditions to obtain the Zn/Al LDH film with the desired properties in terms of structure and morphology, the anion exchange reaction took place. Considering that the best results were achieved when the two-reactant solution was used and the temperature was set at around $100 \text{ }^\circ\text{C}$, two systems were selected to undergo the anion exchange: the one hydrothermally grown from a 50 mM $\text{Zn}(\text{NO}_3)_2$ + 250 mM NaNO_3 for 30 minutes (lower concentration + longer synthesis time) and the other obtained from a 500 mM $\text{Zn}(\text{NO}_3)_2$ + 2500 mM NaNO_3 for 5 minutes (higher concentration + shorter synthesis time), hereinafter referred to as systems LDH- NO_3 -50/250 and LDH- NO_3 -500/2500. The Zn/Al- VO_x^{IV} LDHs were prepared by taking advantage of the inherent ion-exchanging capability of these structures through a nitrate-vanadate replacement process. The vanadate ions were originated from

the sodium metavanadate (NaVO_3) solution in which the LDH-coated plates were immersed. The XRD patterns of the Zn/Al LDH films before and after the immersion are presented below (Figure 29). The vanadate-intercalated counterparts of systems LDH- NO_3 50/250 and LDH- NO_3 500/2500 are henceforth designated as LDH- VO_x -50/250 and LDH- VO_x -500/2500 respectively.

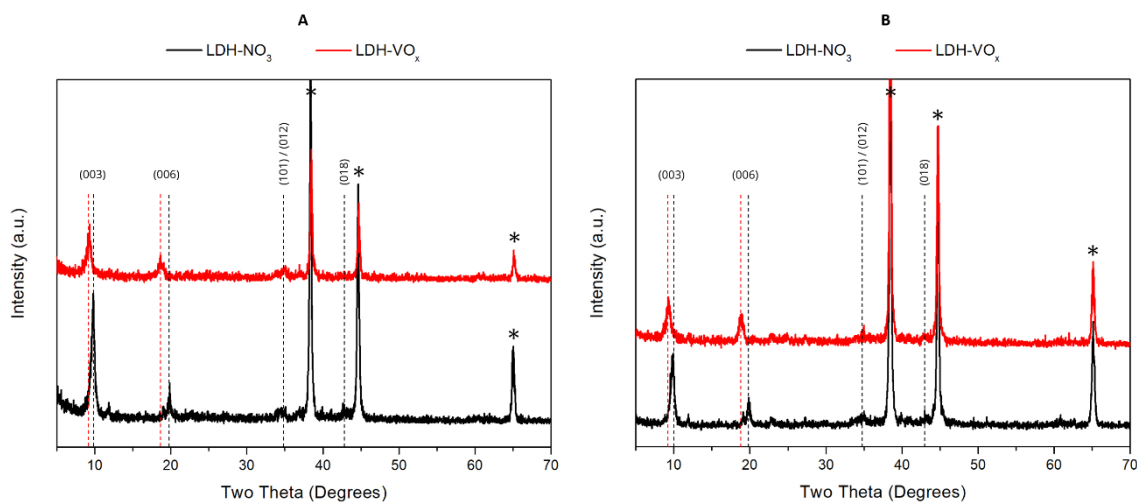


Figure 29 XRD patterns obtained for systems (A) LDH- NO_3 -50/250 (black line) and LDH- VO_x -50/250 (red line) and (B) LDH- NO_3 -500/2500 (black line) and LDH- VO_x -500/2500 (red line).

The diffraction reflections (003) and (006) prior to anion exchange indicate the presence of a Zn/Al- NO_3 LDH film. After the anionic replacement, there is a shift of those reflections towards a lower angle, which can be ascribed to the intercalation of species larger than nitrates (i.e. vanadates, VO_x^{n-}) in the interlayer galleries and the consequent increase in the basal spacing³¹. This observation is supported by the EDS data (Figures A2 and A3, in the Annex), which confirms the presence of vanadium in these samples. Moreover, the decrease in intensity upon anion exchange can be due to a higher atomic scattering factor for vanadium in Zn/Al- VO_x in comparison with that for nitrogen in Zn/Al- NO_3 ¹¹⁹. As evidenced by Figures A2 and A3, the flake-like morphology remains unaltered.

3.2. Electrochemical deposition

Effect of applied potential ($\text{Zn}(\text{NO}_3)_2$ and $\text{Al}(\text{NO}_3)_3$ in solution)

Considering the works available in the literature and described in section 1.7.1.2. of the introduction, the first syntheses were performed with different solutions containing several ratios and concentrations of $\text{Zn}(\text{NO}_3)_2$ and $\text{Al}(\text{NO}_3)_3$ (solution A, $\text{Zn}^{2+}:\text{Al}^{3+} = 1:0.33$; solution B, $\text{Zn}^{2+}:\text{Al}^{3+} = 1:0.5$; solution C, $\text{Zn}^{2+}:\text{Al}^{3+} = 1:0.67$; solution D, $\text{Zn}^{2+}:\text{Al}^{3+} = 1:0.75$) and different fixed potentials ($-1.9 \text{ V} \leq E \leq -1.5 \text{ V}$ vs Ag/AgCl). Table 6 details the composition of each solution. The pH value of the plating solutions was adjusted to 3.8. The deposition time was carried out for 5 minutes and all the experiments were conducted at room temperature. Figure 30 shows the XRD patterns of the obtained Zn/Al LDH conversion films.

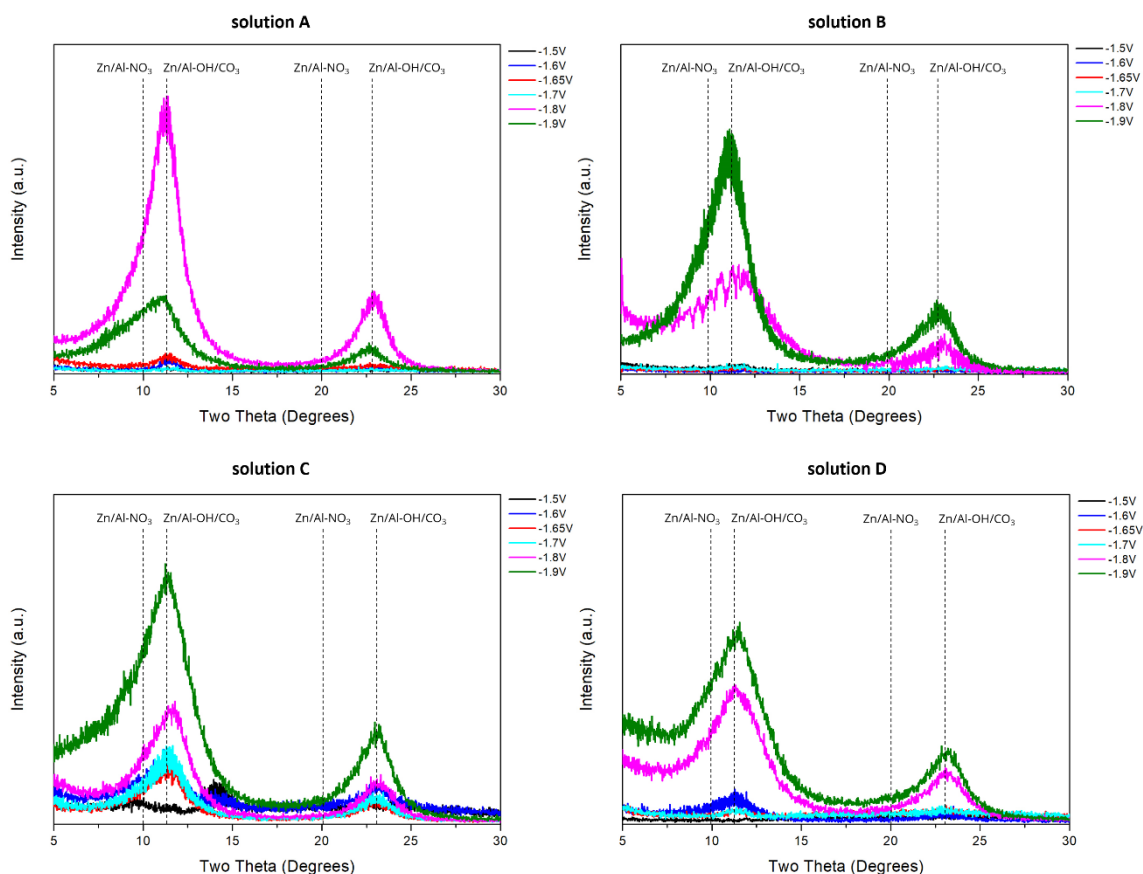


Figure 30 XRD patterns obtained for Zn/Al LDH films electrochemically deposited from solutions **A** ($\text{Zn}^{2+}:\text{Al}^{3+}$ ratio = 1:0.33), **B** ($\text{Zn}^{2+}:\text{Al}^{3+}$ ratio = 1:0.5), **C** ($\text{Zn}^{2+}:\text{Al}^{3+}$ ratio = 1:0.67) and **D** ($\text{Zn}^{2+}:\text{Al}^{3+}$ ratio = 1:0.75), with pH = 3.8, using different potentials. The depositions were carried out at room temperature (RT) during 5 min.

In this first stage, the main purpose was to investigate the effect of the applied potential and the composition of the plating solution on the formation of Zn/Al LDH as the major phase. Thus, the focus was set on the (003) and (006) reflections of the LDH phase, neglecting the occurrence of undesired impurities.

With regard to the $\text{Zn}^{2+}:\text{Al}^{3+}$ ratio, one observes that the sharpest and more intense peaks of the (003), (006) planes were obtained with solution **A**, with an applied potential of -1.8 V vs Ag/AgCl. However, it is possible to obtain LDH phases at less negative potentials when there is a higher content of aluminum in solution (solution **C** and **D**), albeit with less intense and asymmetric reflections. Given the angle position of the (003) and (006) reflections (centred around $2\theta = 11\text{-}12^\circ$ and $2\theta = 22\text{-}24^\circ$, respectively), no nitrate-intercalated LDH seems to have been formed. Instead, it appears that the obtained phase consists of a Zn/Al LDH intercalated either with OH^- or CO_3^{2-} ions since both were available in the plating solutions. This assumption was made based on the calculation of the d -spacing value and the c parameter ($c = 3d$) – 0.737-0.804 nm and 2.211-2.412 nm respectively - which correlate with those published in literature for the same type of hydroxide- or carbonate-intercalated Zn/Al structures¹²⁶.

Concerning the deposition potential, it is clear that increasingly enhanced LDH basal peaks are related with more negative potentials and that almost any deposition does not occur at the most positive ones. Figure 31 shows the diffraction patterns depicted on Figure 30 corresponding to the Zn/Al LDH films obtained using the most negative potentials (-1.8V and -1.9V vs Ag/AgCl), scanned over a wider angular range ($5-50^\circ 2\theta$).

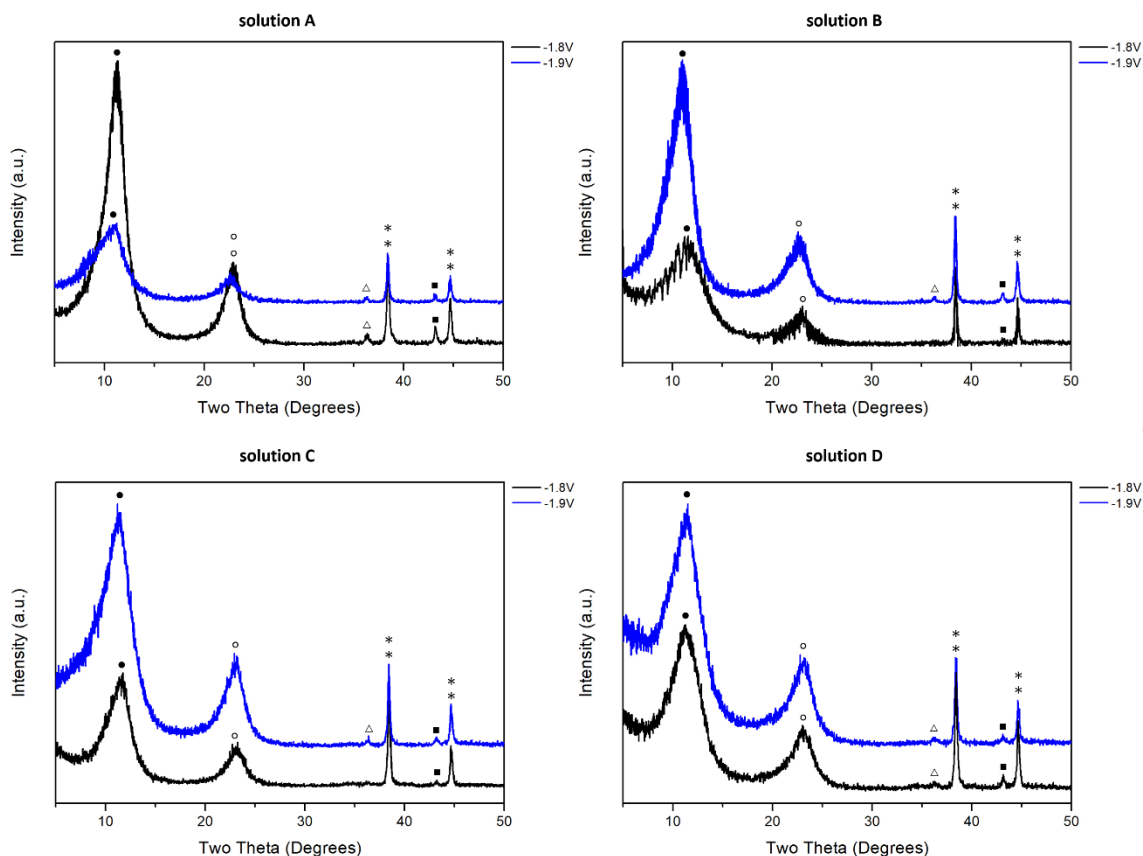


Figure 31 XRD patterns obtained for Zn/Al LDH films electrochemically deposited from solutions **A** ($\text{Zn}^{2+}:\text{Al}^{3+}$ ratio = 1:0.33), **B** ($\text{Zn}^{2+}:\text{Al}^{3+}$ ratio = 1:0.5), **C** ($\text{Zn}^{2+}:\text{Al}^{3+}$ ratio = 1:0.67) and **D** ($\text{Zn}^{2+}:\text{Al}^{3+}$ ratio = 1:0.75), with pH = 3.8, at -1.8V and -1.9V vs Ag/AgCl. The syntheses were carried out at RT during 5 min. The marked peaks are generated by the following: LDH (●) (003) reflection ○ (006) reflection); AA2024 substrate (*); ZnO (Δ) (101) reflection); $\text{Zn}(\text{OH})_2 \cdot 0.5\text{H}_2\text{O}$ (■).

By analysing the presented diffractograms, it is possible to notice the presence of the zinc-related impurities. Despite having Zn/Al LDH as the major phase, most of the deposited films also contain zinc oxide and hydrated zinc hydroxide, $(\text{Zn}(\text{OH})_2 \cdot 0.5\text{H}_2\text{O})^{113}$. The deposition of zinc metal, in turn, does not seem to have occurred. Regarding the films synthesized from solution **A**, as the potential gets more negative, the peaks attributed to both LDH phase and impurities become less intense. As for solutions **B** and **C**, the diffraction patterns revealed enhanced reflections of the (003) and (006) LDH planes for the most negative potential. The intensity of $\text{Zn}(\text{OH})_2$ peaks, in turn, was slightly increased and ZnO appeared when the deposition potential reached -1.9V vs Ag/AgCl¹²⁷. Concerning solution **D**, the formation of hydroxide phases - both LDH and $\text{Zn}(\text{OH})_2$ - became more favourable at more positive potentials in comparison with solutions **B** and **C**. With an applied potential of -1.9V vs Ag/AgCl, the diffractogram showed well-defined LDH peaks and trace amounts of ZnO and $\text{Zn}(\text{OH})_2$. Hence, with the exception of the latter case, using higher Al^{3+} concentrations in the plating solution seems the most

effective approach to promote the suppression of undesired zinc-containing impurities and the formation of purer Zn/Al LDH phases, confirming what has been reported by Yarger *et al.*¹¹³. The latter also seems to be positively affected by lower deposition potentials. Figures 32 and 33 show SEM images of the Zn/Al LDH conversion films electrochemically deposited using solutions A and C, at -1.8 V and -1.9 V vs Ag/AgCl respectively.

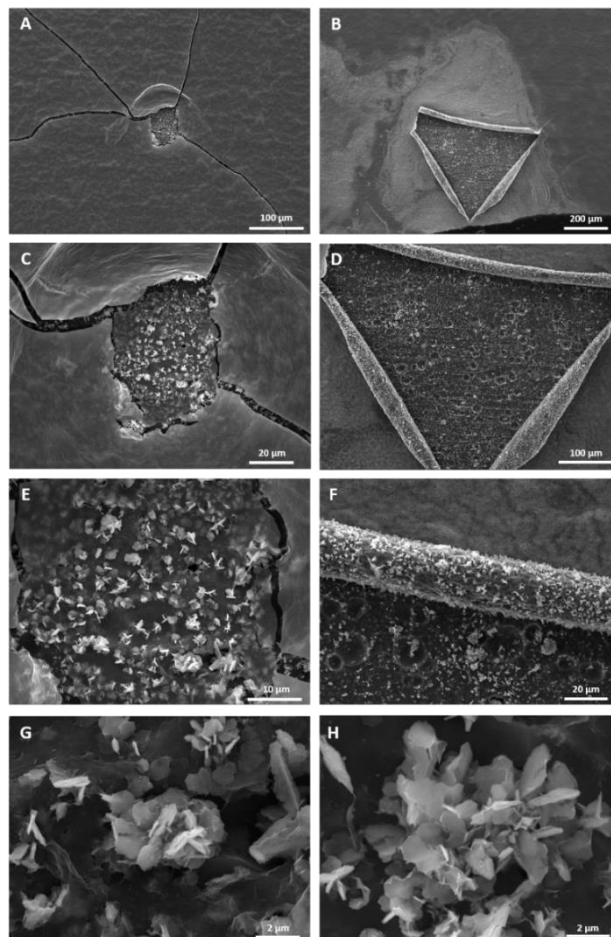


Figure 32 SEM images of the Zn/Al LDH conversion film electrochemically deposited from solution A (pH = 3.8). The applied potential was -1.8 V vs Ag/AgCl. The deposition was carried out in RT conditions, during 5 min.

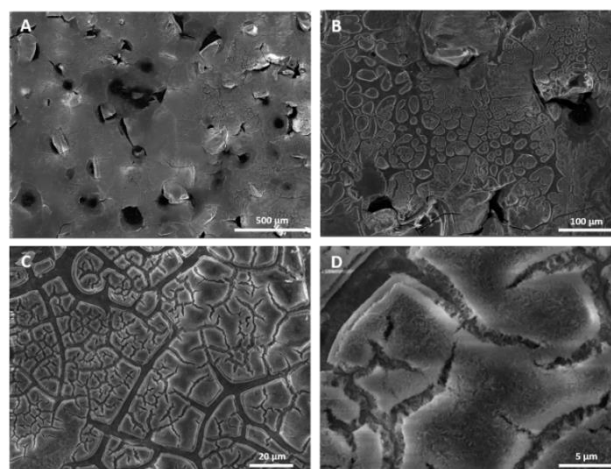


Figure 33 SEM images of the Zn/Al LDH conversion film electrochemically deposited from solution C (pH = 3.8). The applied potential was -1.9 V vs Ag/AgCl. The deposition was carried out in RT conditions, during 5 min.

It can be seen from the Figure 32 - A and C that the obtained film presented a uniformly distributed structure with some cracked areas. Upon finer-scale observation, it was possible to note poorly-defined hexagonal-shaped particles covering the surface underneath what seems to be an outer layer delaminating (Figure 32 - E - H). In contrast to the hydrothermally grown films, the electrodeposited LDH layers appear thicker, denser and more compact since the “craters” resulting from the removal of intermetallics during the pretreatment are not visible, at least in the non-delaminated area. Regarding the orientation of the LDH crystallites, most platelets seem to grow with their *ab*-faces perpendicular to the substrate (recall Figure 7), although not as markedly as in the case of the films prepared by hydrothermal treatment. The film electrodeposited from solution C, at the most negative potential, had a significantly ruptured surface, as shown in Figure 33, which appears to indicate that using the most negative applied potential result in less uniform, more cracked coatings. Considering water stability region at 25°C²⁰, at an applied potential of -1.9 V vs Ag/AgCl (which corresponds to -1.7 V vs SHE), water reduction takes place, forming gaseous hydrogen ($H_2O + 2e^- \Rightarrow H_2(g) + 2OH^-(aq)$) and its liberation may explain the pronounced network of cracks. Nitrates reduction (Equation 10) can also contribute to the disruption of the deposited films since it also results in the production of OH⁻ ions, which is accompanied by a simultaneous increase in hydrogen gas evolution^{106 128}. Taking into account the major difference between the concentration of water and nitrates (approximately 55 M and 12.5 mM + 7.5 mM respectively), water reduction had a more significant contribution to the cathodic generation of hydroxide ions and hydrogen bubbling in relation to the reduction of NO₃⁻. These results suggest that changing the applied potential alters the rate of OH⁻ generation and therefore the local pH in the metal-solution interphase, which in turn affects the precipitation rates of Zn²⁺ and Al³⁺ ions and the formation of Zn/Al LDH phases. The LDH layers deposited from the other solutions, at -1.8 V and -1.9 V vs Ag/AgCl, exhibited a similar morphology to those depicted in Figures 32 and 33 and, for that reason, their SEM images were not included here.

Effect of plating medium pH (Zn(NO₃)₂ and Al(NO₃)₃ in solution)

In view of the findings stated above, the solutions with higher aluminum content were chosen to investigate the effect of the solution pH on the formation of the Zn/Al LDH phase. Thus, the pH of solutions C and D was readjusted by adding either HNO₃ or NaOH in order to obtain more or less acidic plating baths. The deposition time and the temperature conditions were kept unaltered. Figure 34 shows the XRD spectra of the Zn/Al LDH conversion films electrodeposited on the AA2024 substrates at -1.9 V and -1.8 V vs Ag/AgCl, using solutions C - 3, C, C - 4.2, D - 3, D and D - 4.2 described in Table 6.

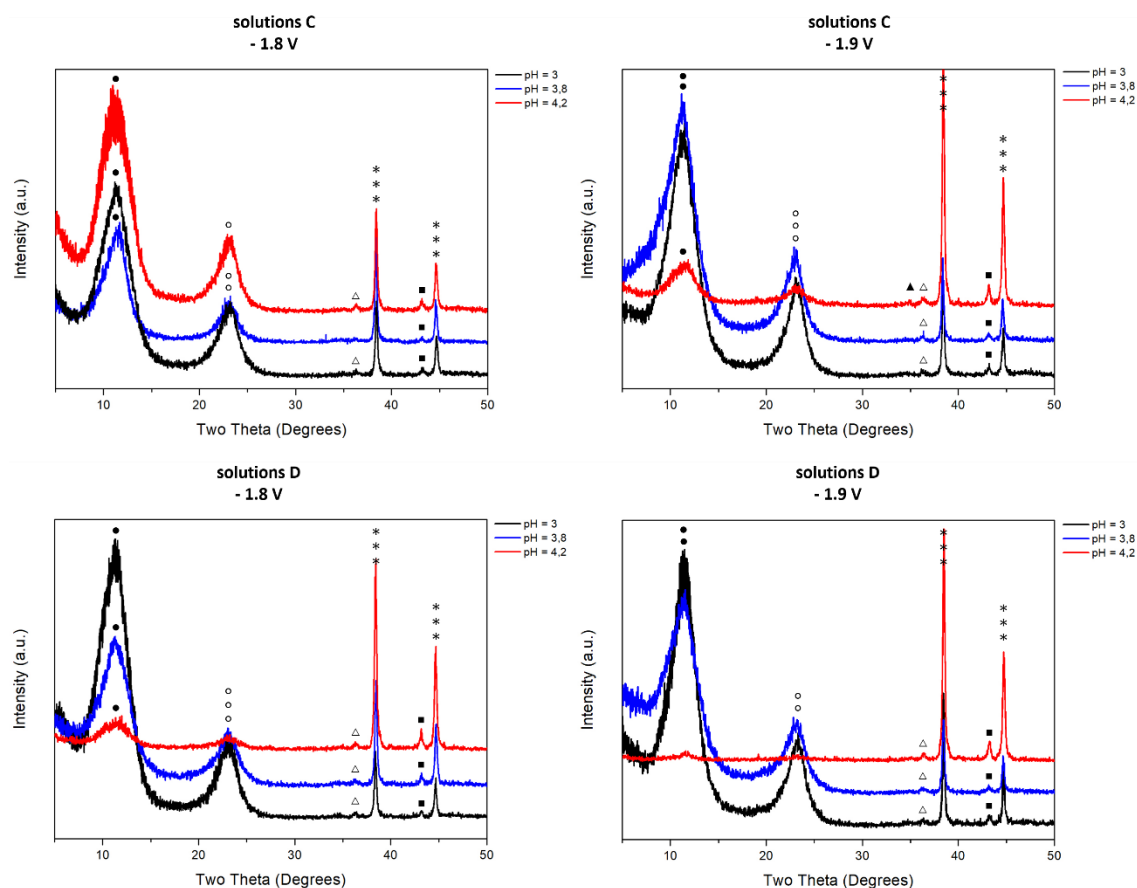


Figure 34 XRD patterns obtained for Zn/Al LDH films electrodeposited from solutions **C - 3**, **C - 4.2**, **D - 3**, **D - 4.2** at -1.8 V and -1.9V vs Ag/AgCl. The syntheses were carried out in RT conditions, during 5 min. The marked peaks are generated by the following: **LDH** (● (003) reflection ○ (006) reflection); **AA2024** substrate (*); **ZnO** (△ (101) reflection); **Zn(OH)₂·0.5H₂O** (■).

A general overview of the presented diffractograms makes it evident that a pH of 4.2 is the less suitable to form pure and crystalline LDH phases and suppress the deposition of impurities, except in the case when the film was synthesized at -1.8 V from solution **C - 4.2**. When the most acidic plating baths were used, no significant changes were observed in the peaks ascribed to ZnO and Zn(OH)₂·0.5H₂O when the applied potential and Al³⁺ concentration were varied. On the other hand, the sharper and more intense LDH peaks were produced when the films were electrodeposited from solutions with the lowest pH, thus ruling out the intermediate pH value. The sharp and symmetrical diffraction peaks indicate the well-crystallized layered structure of the Zn/Al LDHs.

According to the potential - pH equilibrium diagram for the aluminum-water system at 25°C (recall Figure 2), the oxide layer naturally formed on aluminum surface tends to dissolve in acidic media, forming Al³⁺ ions. For this reason, when the electrodeposition process occurs in a plating bath with a pH of 3, first (i.e. before starting the electrodeposition process) there will be an increase in Al³⁺ concentration due to dissolution of the substrate, followed by co-precipitation of Zn²⁺ and Al³⁺ in the metal-solution interface as soon as an appropriate negative potential starts to be applied, thereby causing water and nitrates reduction and leading to a local increase in the pH near the metallic substrate. Under these conditions, precipitation of Zn²⁺ and Al³⁺ occurs only near the working electrode vicinity. Contrastingly, in solutions whose pH was increased with addition of NaOH, the aluminum oxide layer in AA2024

becomes more stable and the amount of Al^{3+} ions coming from the substrate decreases. At the same time, available Al^{3+} ions from the nitrate salt used to prepare the plating solutions will start to precipitate not only in the vicinity of the working electrode but also in the bulk solution due to the increase in pH, which might explain the poor results obtained when the pH was adjusted to 4.2. Bearing this in mind, a pH of 3 appears to be close to the optimum pH to form a pure and crystalline Zn/Al LDH phase, which is in agreement with results reported in the literature for the same type of electrodeposited LDHs¹⁰⁶. Therefore, only one system was chosen to be tested in terms of its adhesion to the aluminum substrate and corrosion resistant properties: the LDH film electrochemically deposited from a 12.5 mM $\text{Zn}(\text{NO}_3)_2$ + 9.4 mM $\text{Al}(\text{NO}_3)_3$ solution ($\text{Zn}^{2+}:\text{Al}^{3+}$ ratio = 1:0.75), with a pH of 3, at -1.8 V vs Ag/AgCl, for 5 minutes (hereinafter named as LDH-ED-1/0.75).

Effect of applied potential ($\text{Zn}(\text{NO}_3)_2$ in solution)

The second approach to electrochemically deposit Zn/Al LDH conversion films, as explained earlier, involved a similar procedure, the only difference being the composition of the plating bath. It consisted of an aqueous solution only containing 12.5 mM $\text{Zn}(\text{NO}_3)_2$ as source of Zn^{2+} ions, with pH = 3 (in this case, the AA2024 substrate is the only source of Al^{3+} species). Likewise, the experiments were carried out at room temperature, at fixed potentials of -1.9 V, -1.8 V and -1.7 V vs Ag/AgCl. Regarding the synthesis duration, and presuming that aluminum cations would not be so readily available as in the previous procedure, it was decided to use longer deposition times - 15 minutes - in order to ensure the formation of the Zn/Al LDH layer. Figure 35 demonstrates the XRD patterns of the resulting films.

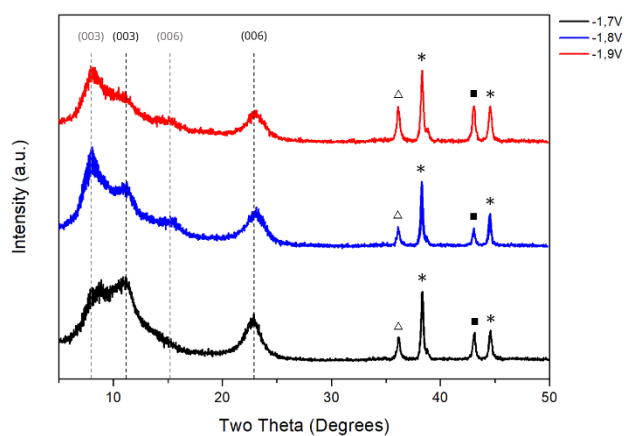


Figure 35 XRD patterns obtained for Zn/Al LDH films electrodeposited from a 12.5 mM $\text{Zn}(\text{NO}_3)_2$ (pH = 3), at different applied potentials, in RT conditions, during 15 min. The marked peaks are generated by the following: **LDH** (● (003) reflection o (006) reflection); **AA2024** substrate (*); **ZnO** (Δ (101) reflection); **Zn(OH)₂·0.5H₂O** (■).

Contrarily to what was observed in the previous experiments when a $\text{Zn}^{2+}/\text{Al}^{3+}$ solution was used, there seems to be two extra (003) and (006) basal peaks at $2\theta \approx 7-8^\circ$ and $2\theta \approx 14-16^\circ$ respectively in addition to those attributed to the Zn/Al-OH/CO₃ LDH phase at $2\theta \approx 11-12^\circ$ and $2\theta \approx 22-24^\circ$. The position of such reflections seems to suggest the existence of an additional LDH phase. Considering the basal spacing d_{003} and the brucite-like layer thickness, which are approximately 1.104-1.261 nm and 0.477 nm respectively, the interlamellar space is estimated as 0.627-0.784 nm (bigger than the diameter of OH^- or CO_3^{2-} ions¹²⁹). Given the lack of anions in solution other than those specified, the expansion of the

interlayer region may be related to a high Zn/Al ratio. For a given LDH structure, the d -spacing and the lattice parameter a strongly depend on the composition of the cationic sheets. Considering the charge number of Zn^{2+} and Al^{3+} , increasing the zinc to aluminum ratio may increase the distance between the positive layers and weaken the bonding between such layers and the intergallery anions, thus causing the interlayer region to expand^{130 131}. Hence, the multiple basal reflections may be generated by two distinct Zn/Al LDH phases with different Zn/Al molar ratios. Regarding the presence of impurities, there is a slight decrease of the peaks attributed to $\text{Zn}(\text{OH})_2 \cdot 0.5\text{H}_2\text{O}$ and ZnO when the intermediate deposition potential is applied. The surface of the Zn/Al LDH films in question is shown below (Figures 36 and 37).

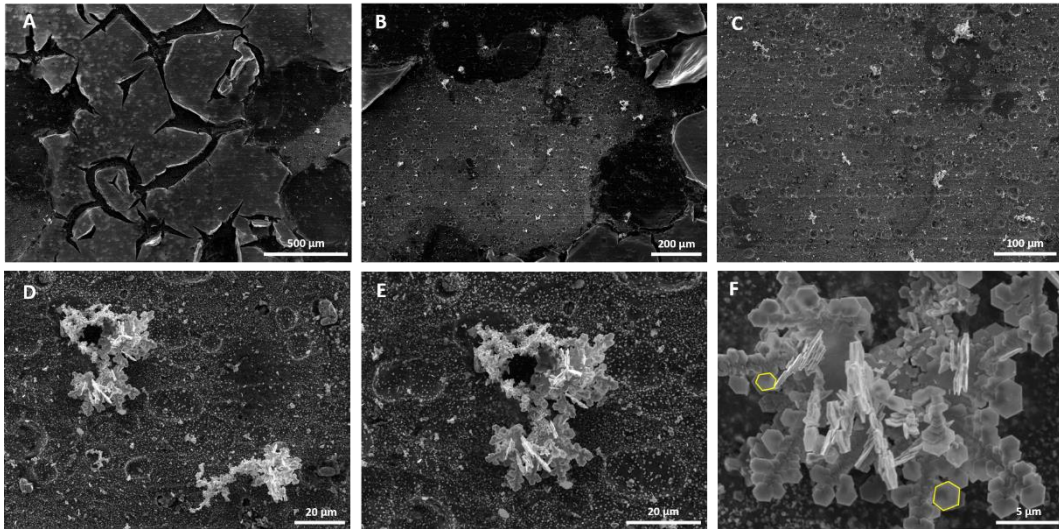


Figure 36 SEM images of the Zn/Al- NO_3 LDH conversion film electrodeposited from a 12.5 mM $\text{Zn}(\text{NO}_3)_2$ solution (pH = 3) with an applied potential of - 1.7 V vs Ag/AgCl. The deposition was carried out in RT conditions, during 15 min.

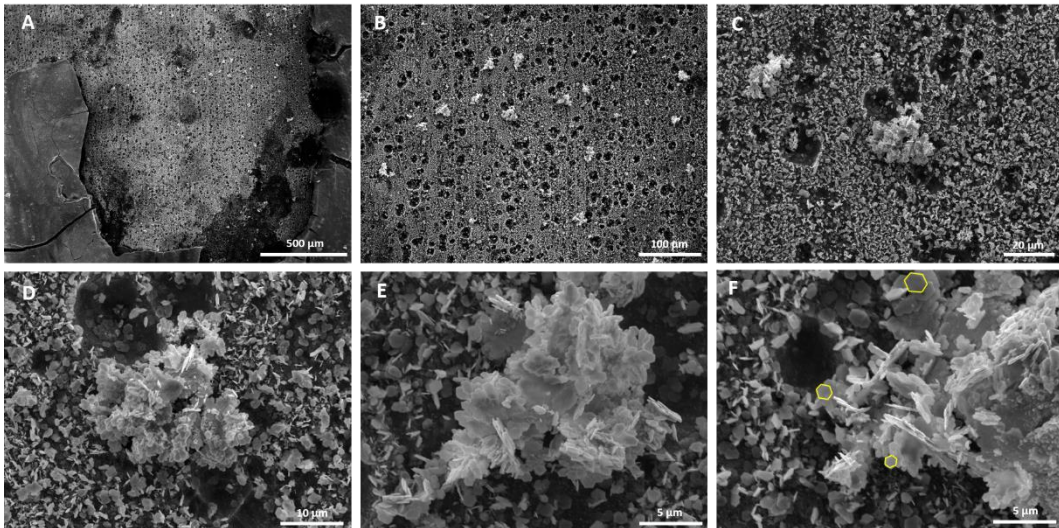


Figure 37 SEM images of the Zn/Al- NO_3 LDH conversion film electrodeposited from a 12.5 mM $\text{Zn}(\text{NO}_3)_2$ solution (pH = 3) with an applied potential of - 1.9 V vs Ag/AgCl. The deposition was carried out in RT conditions, during 15 min.

Regarding the film electrodeposited at -1.7 V vs Ag/AgCl, it is possible to observe an analogous morphology to that depicted in Figure 32, this time with a sporadic distribution of agglomerated perfectly-defined hexagons (Figure 36 - F). On the other hand, a lower potential resulted in a denser,

more uniform coverage by seemingly smaller hexagonal platelets. As previously observed, two different layers can be distinguished, the most superficial one being severely delaminated and revealing the well-defined hexagonal platelets that grew underneath it (Figure 36 - B and Figure 37 - A). The LDH film electrodeposited at an applied potential of -1.8 V vs Ag/AgCl exhibited an identical morphology to that depicted in the figures above and, for that reason, the corresponding SEM images were not included here.

Effect of deposition time ($\text{Zn}(\text{NO}_3)_2$ in solution)

Lastly, while the other parameters were held constant, the deposition time was varied in order to investigate its effect on the quality of the obtained films. Figure 38 illustrates the diffraction patterns of the Zn/Al LDH coatings grown on AA2024 plates from a 12.5 mM solution, whose pH value was adjusted to 3, with an applied potential of -1.9 V and -1.8 V vs Ag/AgCl , for 5, 10 and 15 minutes.

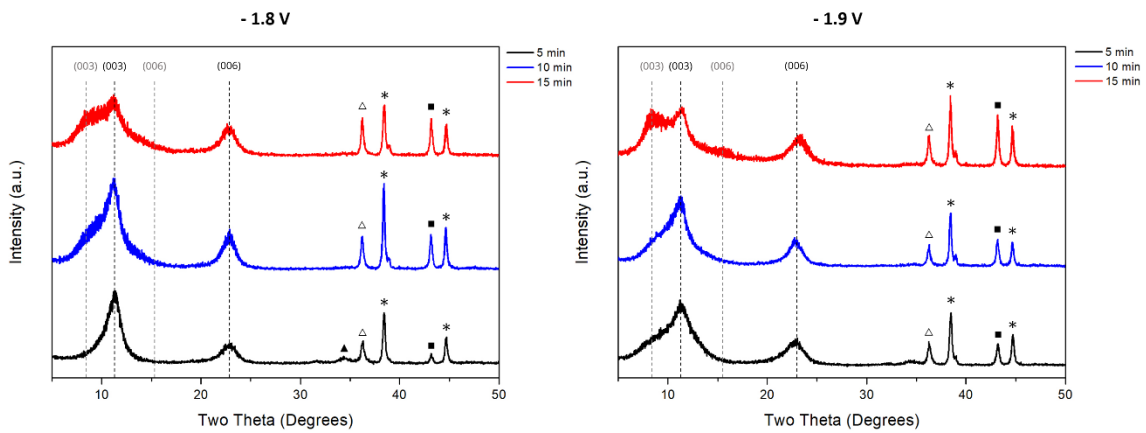


Figure 38 XRD patterns obtained for Zn/Al LDH films electrodeposited from a 12.5 mM $\text{Zn}(\text{NO}_3)_2$ solution ($\text{pH} = 3$), at applied potentials of -1.8 V and -1.9 V vs Ag/AgCl , in RT conditions, during different times. The marked peaks are generated by the following: LDH (● (003) reflection ○ (006) reflection); AA2024 substrate (*); ZnO (Δ (101) reflection \blacktriangle (002) reflection ∇ (100) reflection); $\text{Zn}(\text{OH})_2 \cdot 0.5\text{H}_2\text{O}$ (\blacksquare).

By analysing the presented diffractograms, the formation of an extra LDH phase seems to occur for longer immersion times. This may be associated with increasingly less accessible Al^{3+} as the first LDHs starts depositing, with the subsequent deposition of Zn-rich hydroxide phases since there is Zn^{2+} in solution but not Al^{3+} . As the deposition potential gets more negative, such phenomenon is also observed for shorter times. Longer depositions also seem associated with an increase in intensity of the peaks generated by zinc-containing impurities. Hence, the optimum conditions for the electrochemical deposition of a pure and crystalline Zn/Al LDH phase seem to involve a 5-minute synthesis from a 12.5 mM solution ($\text{pH} = 3$), with an applied potential of -1.8 V vs Ag/AgCl . The system obtained under such conditions is henceforth referred to as LDH-ED-12.5. Its microstructural analysis (Figure 39) confirms the existence of two distinct layers - and the propensity of the outer one to delaminate - and the same nano-sized platelet-like compounds between them. The SEM images obtained for the LDH films electrodeposited at -1.8 V for 10 and 15 minutes and at -1.9 V for 5 and 15 minutes are presented in the Annex as Figures A4, A5, A6 and A7 respectively.

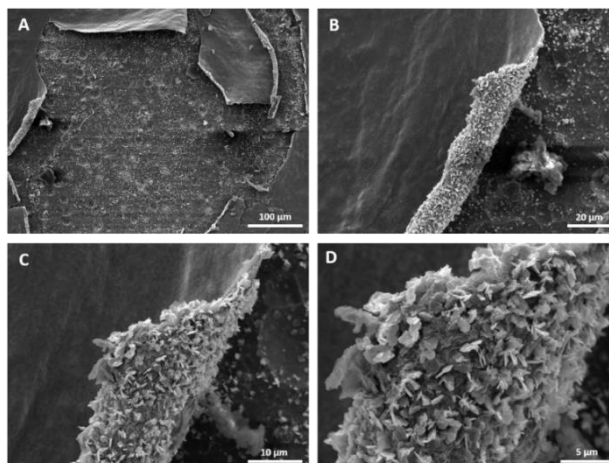


Figure 39 SEM images obtained for the LDH conversion film electrochemically deposited on a AA2024 substrate from a 12,5 mM $\text{Zn}(\text{NO}_3)_2$ solution (pH = 3). The deposition was carried out at $-1,8$ V vs Ag/AgCl, in RT conditions, during 5 min.

Intercalation of corrosion inhibitors in the LDH structure

Although no nitrate-intercalated LDHs were obtained through electrochemical deposition, the anion exchange was undertaken in an attempt to replace the ions present in the interlamellar space with vanadates. The reaction has proved ineffective since no changes were observed when comparing the diffraction data acquired before and after it took place, as seen above (Figure 40).

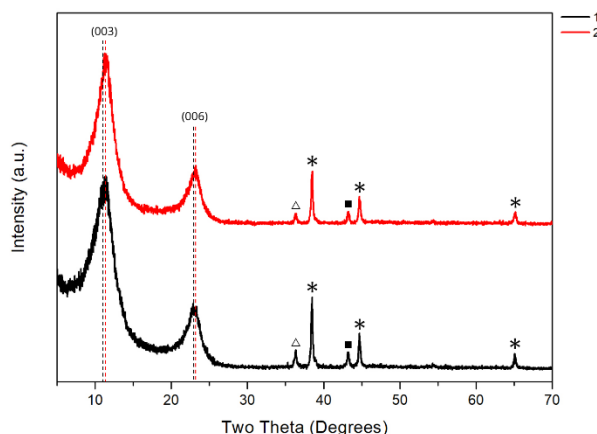


Figure 40 XRD patterns obtained for LDH-ED-1/0.75, before (1) and after (2) anion exchange reaction.

This outcome is consistent with literature since carbonates and hydroxides stand out in terms of anion-exchange selectivity in the case of Zn/Al LDHs ($\text{CO}_3^{2-} > \text{OH}^- > \text{NO}_3^-$)¹³². The high affinity of CO_3^{2-} and OH^- ions towards this specific type of LDH may also explain why nitrates were not intercalated during the electrosynthesis. Notwithstanding what has been stated, the EDS results confirm the presence of vanadium in the surface of the film (Figure A8, in the Annex). Given the unsuccessful attempt to intercalate vanadates into LDH-ED-1/0.75, such procedure was not performed for LDH-ED-12.5 and the adhesion assessment and electrochemical measurements were only implemented for system LDH-ED-1/0.75.

3.3. Characterization of coating properties for anticorrosion applications

3.3.1. Films prepared by hydrothermal treatment

Figure 41 displays the optical microscopy images of the systems LDH-NO₃-50/250 and LDH-NO₃-500/2500 after the cross-cut tape test.

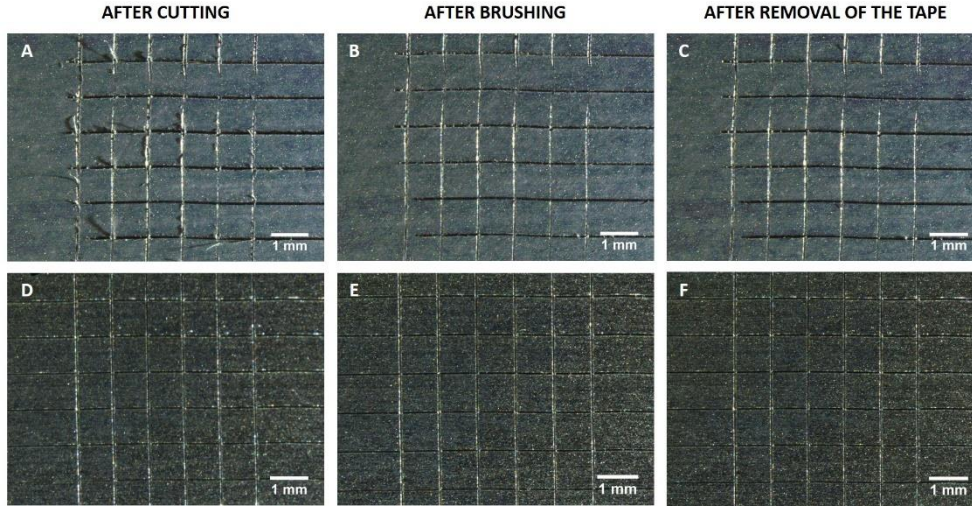


Figure 41 Optical microscope images of the hydrothermally grown Zn/Al LDH films after the cross-cut test: LDH-NO₃-50/250 (A, B and C) LDH-NO₃-500/2500 (D, E and F).

In both cases, none of the squares of the lattice was detached after the removal of the tape and the edges of the cuts were smooth. Even though some peeling of the substrate was observed after cutting the first sample (Figure 41 - A), no major delamination occurred on the cross-cutting surface, suggesting that both films adhered perfectly to the AA2024 substrate. Thus, the adhesion of both coatings to the aluminum surface was considered very high and classified as 0, according to Table 3.

In order to investigate the effect of VO_xⁿ⁻ ions on the corrosion inhibition of AA2024 substrates when intercalated in the LDH films hydrothermally grown under the above-specified conditions, electrochemical impedance spectroscopy measurements were carried out with the samples coated with Zn/Al-NO₃ and Zn/Al-VO_x LDHs, using a bare AA2024 plate as reference. Figures 42 and 43 depict the Bode and Nyquist representations of the EIS spectra acquired for systems LDH-NO₃-50/250, LDH-NO₃-500/2500, LDH-VO_x-50/250 and LDH-VO_x-500/2500 and for the A2024-T3 substrate, during a 21-day immersion test in 0.05 M NaCl solution. It was decided to use a rather dilute NaCl solution in order to avoid high corrosion rates and facilitate the detection of relevant physical parameters not identified otherwise⁹⁹. With the exception of some scattered points observed at low frequencies in the phase angle of Bode plots, associated with nonstationary conditions, the LDH-coated plates show a stable response in the chosen solution. For ease of understanding, the Bode diagrams were divided into three distinct frequency regions in accordance with the different time constants observed: regions I, II and III corresponding to the low ($f \approx 10^{-2}$ - 10^{-1} Hz), intermediate ($f \approx 10^0$ - 10^1 Hz) and high ($f > 10^4$ Hz) frequencies respectively.

Results and discussion

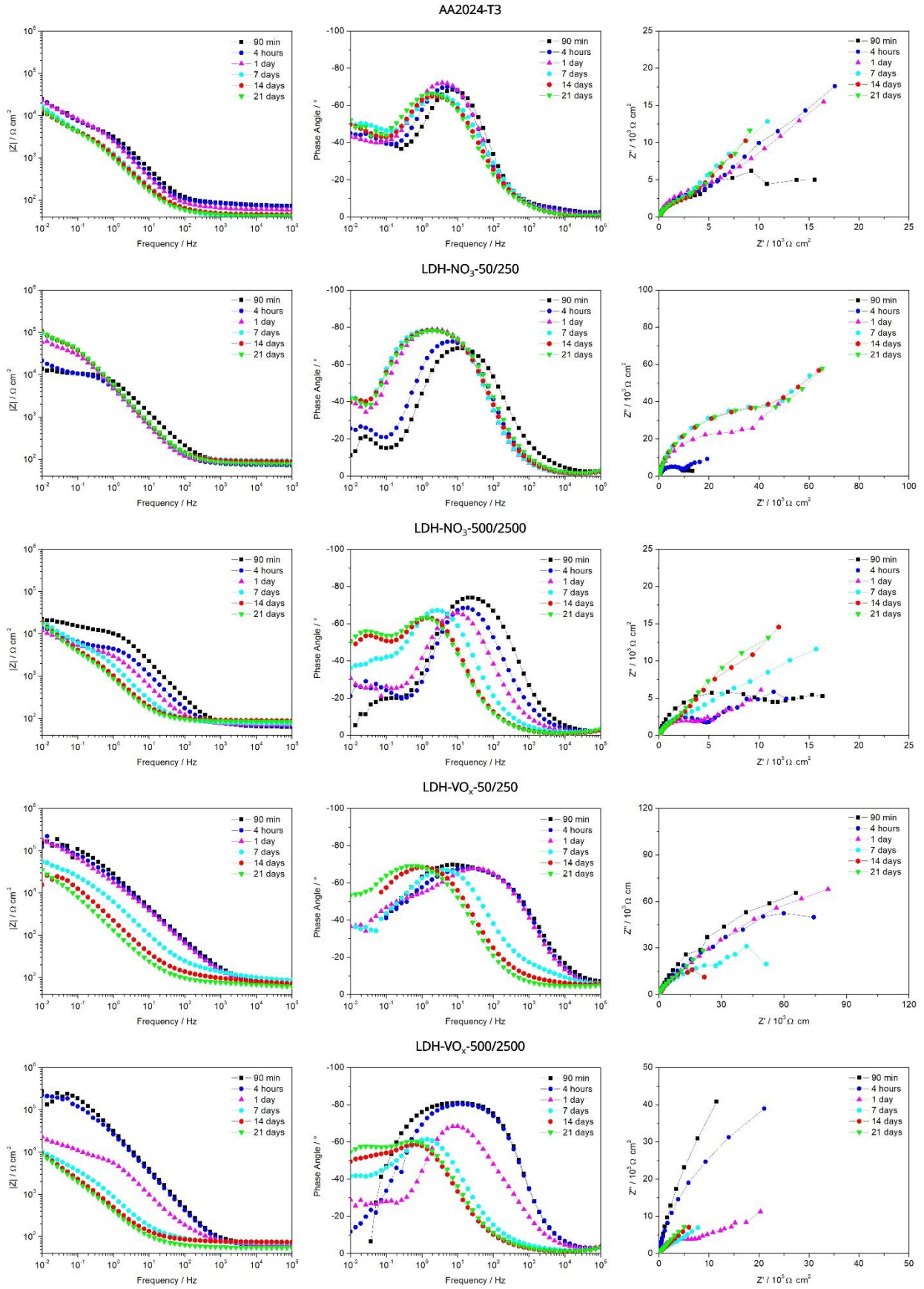


Figure 42 Bode and Nyquist representations of EIS spectra acquired for AA2024-T3, LDH-NO₃-50/250, LDH-NO₃-500/250, LDH-VO_x-50/250, and LDH-VO_x-500/250 in a 0.05 NaCl solution for different immersion times.

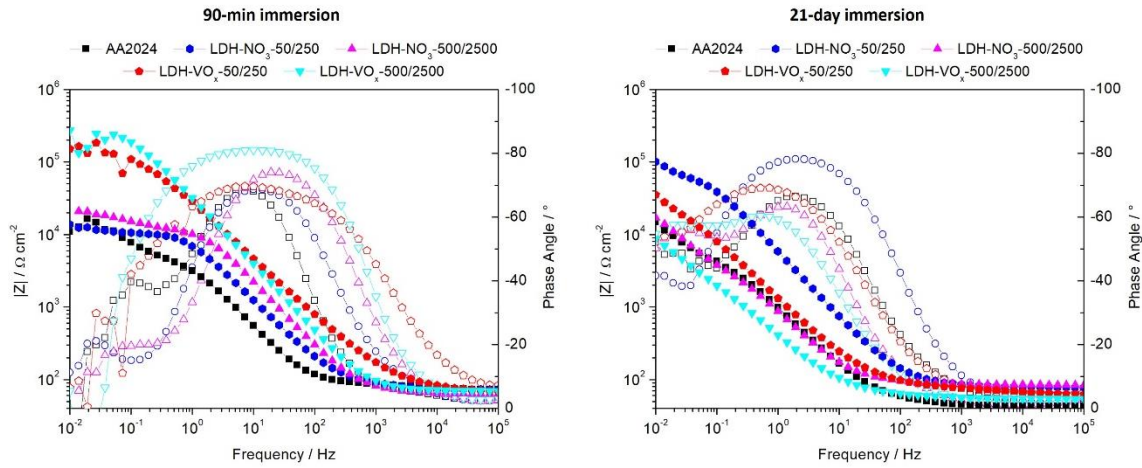


Figure 43 Bode representation of EIS spectra acquired for AA2024-T3, LDH-NO₃-50/250, LDH-NO₃-500/2500, LDH-VO_x-50/250, and LDH-VO_x-500/2500 after 90 min and 21 days of immersion in a 0.05 NaCl solution.

Regarding the reference system (AA2024-T3 substrate), it is possible to distinguish two-time constants. The one in region II is ascribed to the response of the electrochemical activity at the surface (corrosion processes), while the other, in region I, is possibly due to mass transport-controlled processes⁷⁰⁹⁹. After two weeks of immersion, the surface of the bare metal is completely corroded and covered with white corrosion products (Figure 44).

In the beginning of the immersion, the two LDH-NO₃ systems (LDH-NO₃-50/250 and LDH-NO₃-500/2500) are similar to the reference system in terms of their impedance values. However, for longer immersion intervals, there is a clear difference between them. The film synthesized under more diluted conditions of Zn²⁺ for a longer period of time (LDH-NO₃-50/250) shows better performance than those prepared under higher concentrations of Zn²⁺ for only 5 minutes (LDH-NO₃-500/2500). This observation is visually confirmed by the optical photographs depicted below (Figure 44). While LDH-NO₃-50/250 shows only a few black pits after the 21-day immersion in NaCl, LDH-NO₃-500/2500 reveals an extensive deposition by corrosion products, which supports the protective effect provided by the former.

In the case of LDH-NO₃-50/250 systems, the time constant in region II observed for 90 min and 4h of immersion may be ascribed to the LDH/aluminium oxide film. From previous works it was possible to observe that since LDHs are grown at the expense of the aluminium substrate, a thinning of the oxide film (and consequently an increase in capacitance) could be expected. However, after 4 hours the intermediate time constant is found at lower frequencies ($\sim 10^0$ Hz) and may be due to corrosion processes ongoing at the metal-solution interface, whereas the low frequency time constant (10^{-2} - 10^{-1} Hz) may be associated with mass transport-controlled processes. Nevertheless, and contrasting with the reference, low frequency impedance is higher than for the reference which can somehow be related to some active protection effect conferred by the LDH-NO₃. According to the literature, some level of corrosion retardation may be attributed to both NO₃⁻ and Zn²⁺. As reported by Buchheit *et al*²⁷, Zn²⁺ ions entrapped in the synthesized LDH structures can act as cathodic inhibitors by precipitating as hydroxides on the cathodic sites, thus hindering corrosion of the underlying substrate. Nitrates, in turn, have also been described as species with inhibiting properties towards aluminum alloys¹³³.

For the LDH-NO₃-500/2500, a similar assignment of time constants can be done, though with some differences. First the layer grown seems thicker and/or more protective in the short-term as the time constant is centred at higher frequencies and with overall impedance magnitude values higher than those for LDH-NO₃-50/250. Nevertheless, this initial protective effect rapidly disappears and after 4 hours the low frequency impedance magnitude is already lower than for LDH-NO₃-50/250. Similar effect was found in the work of Tedim *et al*³⁵, where the increase in Zn²⁺ concentration led to thick films which failed earlier than those prepared under more diluted conditions. This collapse may occur as a result of the weakening of the oxide film to grow thicker LDH layers.

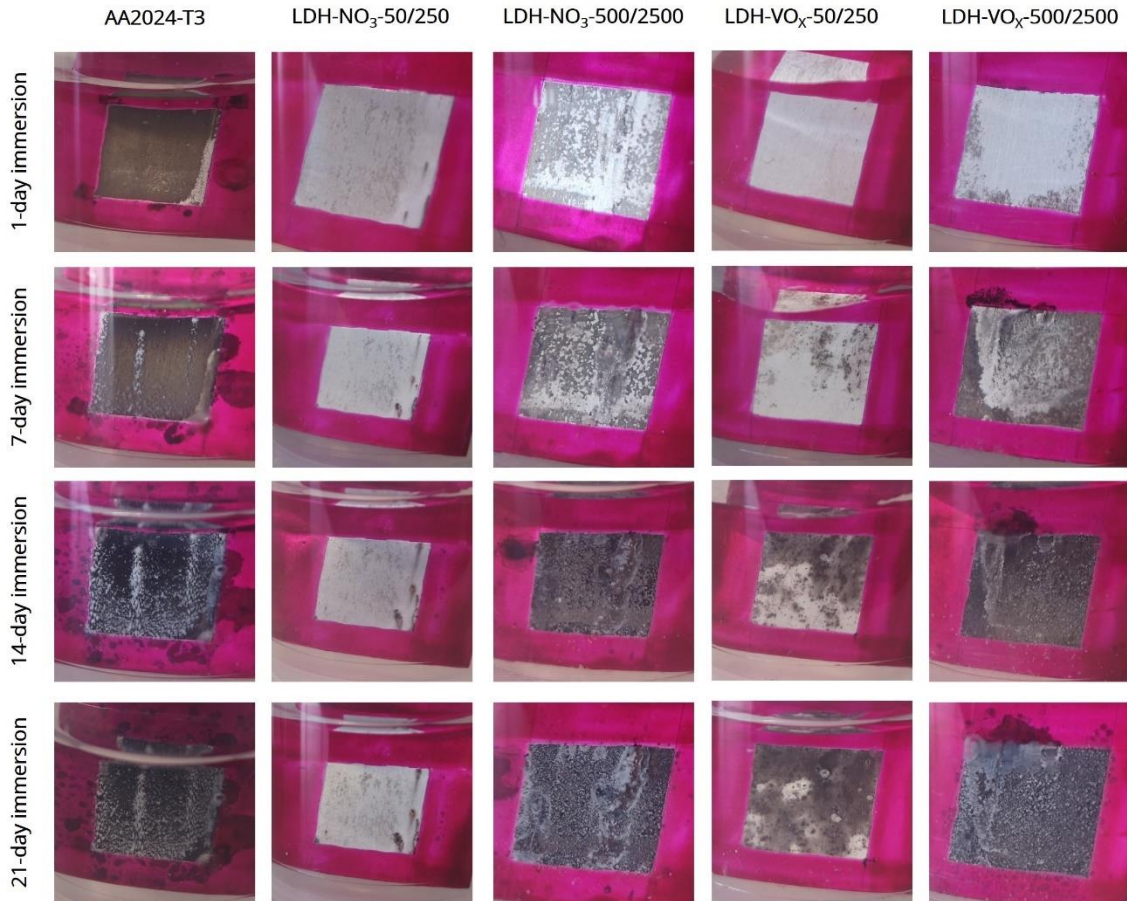


Figure 44 Optical photographs obtained for AA2024-T3, LDH-NO₃ 50/250, LDH-NO₃ 500/2500, LDH-VO_x 50/250, and LDH-VO_x 500/2500 after different immersion periods in a 0.05 NaCl solution.

Considering the vanadate-intercalated systems (LDH-VO_x-50/250 and LDH-VO_x-500/2500), both show impedance values at low frequencies about one order of magnitude higher than their nitrate-containing counterparts in the first hours of immersion. Nonetheless, for longer immersion periods, such values are considerably lower than the initial ones, especially for system LDH-VO_x-500/2500. This is in accordance with the visual assessment in Figure 44. The initial protective effect of vanadates, with the highest impedance magnitude values in the whole frequency range, rapidly vanishes after 1 day of immersion (before 24 hours of immersion, only one broad time-constant associated with the oxide/LDH-VO_x can be observed, although some asymmetry in the phase angle and scattering in the low frequency range may suggest initiation of electrochemical processes). It is worth of mention that after exchange some mechanical fragmentation of LDH phase has occurred upon intercalation of vanadates, which

together with thinning of the native oxide film to grow LDHs can lead to a dramatic failure when immersed in NaCl solutions. For longer immersion times, the two-time constants detected are assigned to the double layer response associated with the ongoing corrosion processes and mass transport-controlled processes. From all the results presented, the best system appears to be LDH-NO₃-50/250.

3.3.2. Films prepared by electrochemical deposition

The adhesion test results of system LDH-ED-1/0.75 depicted on the images below (Figure 45) seem to confirm the existence of the outer layer previously observed (recall Figures 32 and 39), which was detached from the coating after removal of the tape from both samples, exposing a brighter area covered with the LDH flakes. While this may not be clear on Figure 45 - C, a photograph taken after the cross-cut test shows that the superficial part of the film was transferred to the adhesive tape (Figure A9 in the Annex). According to Table 3, the adhesion quality state of the electrodeposited Zn/Al LDH coating corresponds to a 4-5 ranking, which implies that the film adhered poorly to the AA2024 substrate.



Figure 45 Optical microscope images of the system LDH-ED-1/0.75 after the cross-cut test.

Figures 46 and 47 depicts the Bode and Nyquist representations of the EIS spectra acquired for system LDH-ED-1/0.75 before and after the anionic replacement process (from this point onwards designated as LDH-ED-1/0.75 and LDH-ED-1/0.75-V respectively) and for the A2024-T3 substrate, during a 21-day immersion test in 0.05 M NaCl solution. For ease of understanding, the Bode diagrams were divided into three distinct frequency regions in accordance with the different time constants observed: regions I, II and III corresponding to the low ($f \approx 10^{-2}$ - 10^{-1} Hz), intermediate ($f \approx 10^0$ - 10^1 Hz) and high ($f > 10^4$ Hz) frequencies respectively.

Results and discussion

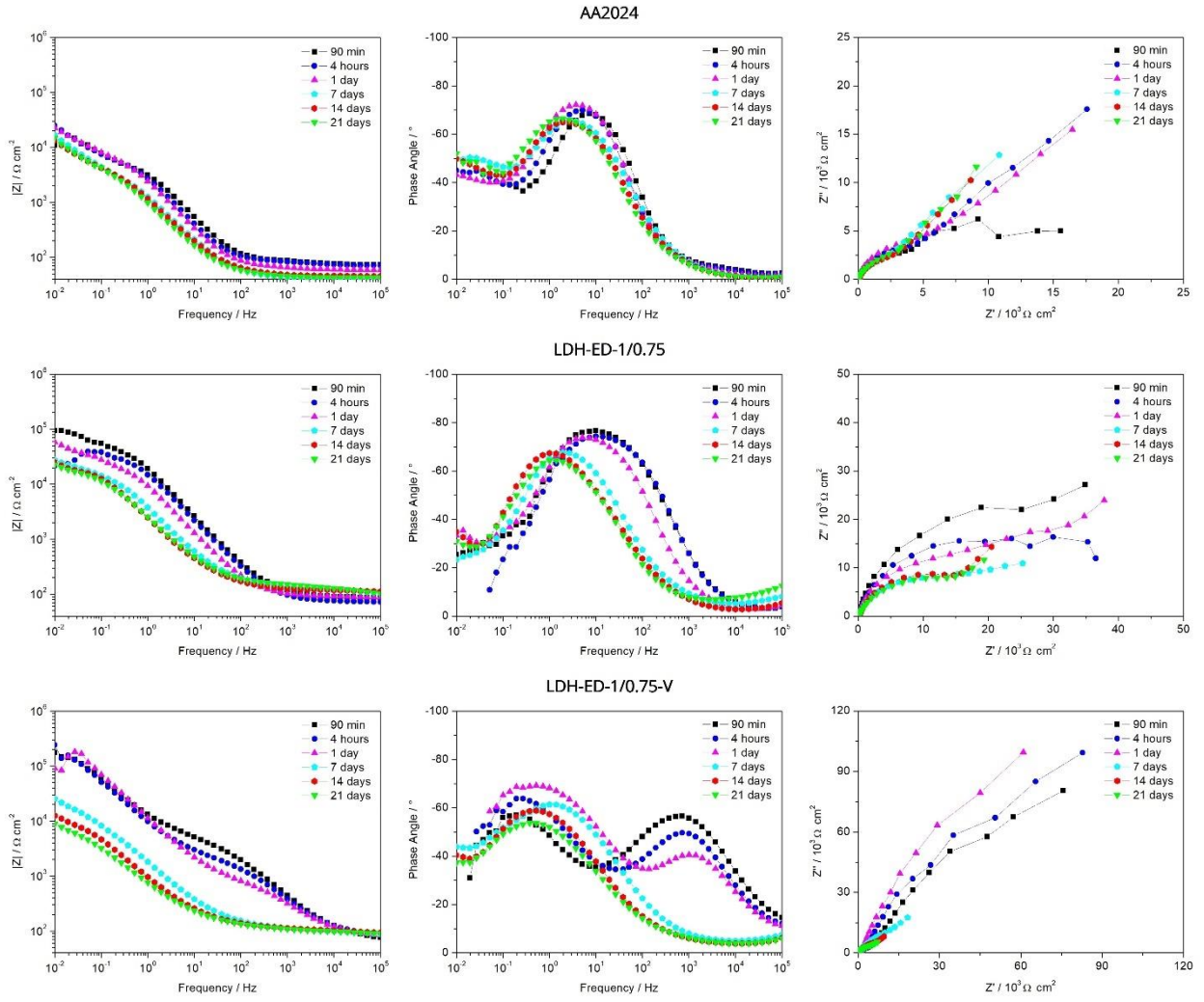


Figure 46 Bode and Nyquist representations of EIS spectra acquired for AA2024-T3, LDH-ED-1/0.75 and LDH-ED-1/0.75-V in a 0.05 NaCl solution for different immersion times.

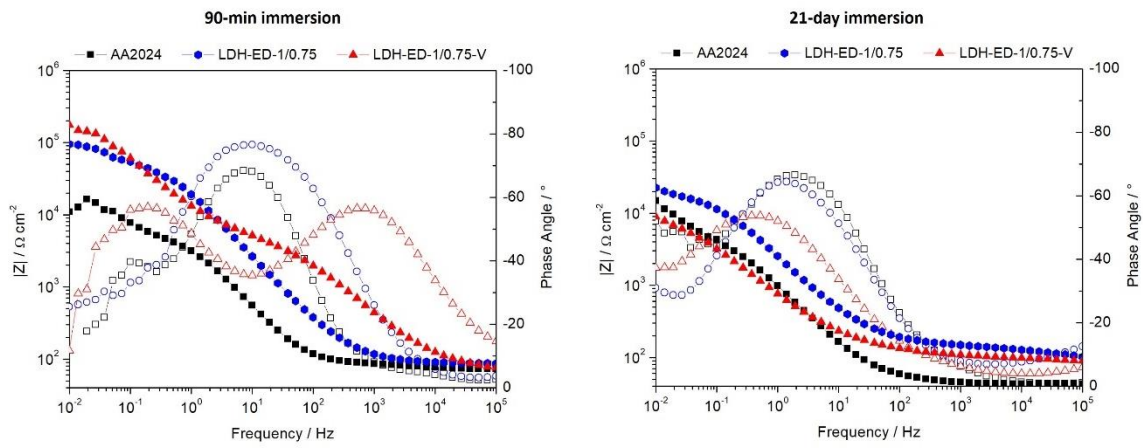


Figure 47 Bode representation of EIS spectra acquired for AA2024-T3, LDH-ED-1/0.75 and LDH-ED-1/0.75-V after 90 min and 21 days of immersion in a 0.05 NaCl solution.

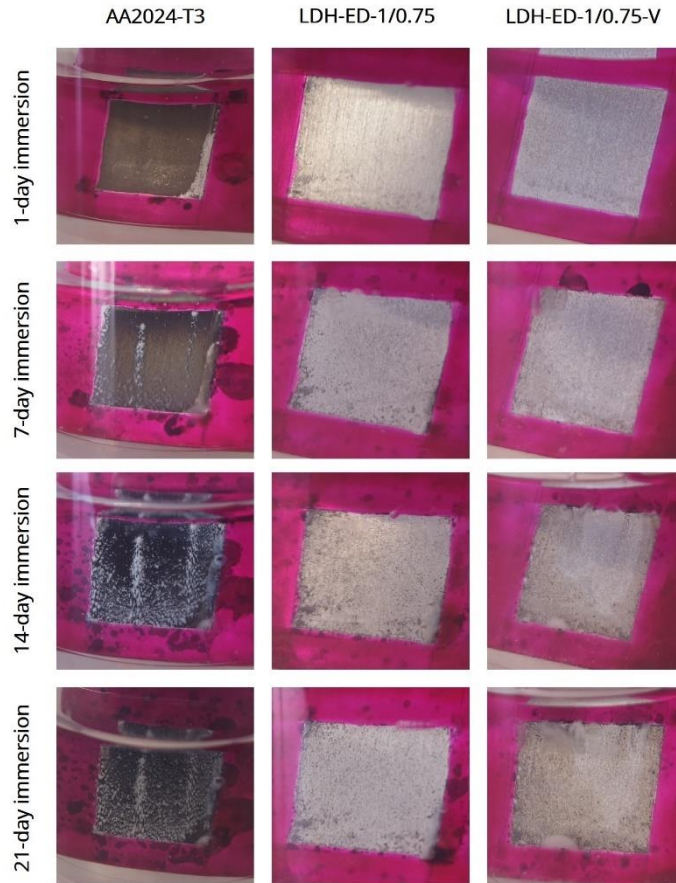


Figure 48 Optical photographs obtained for AA2024-T3, LDH-ED-1/0.75 and LDH-ED-1/0.75-V after different immersion periods in a 0.05 NaCl solution.

In the beginning of the immersion, LDH-coated plates, both with and without vanadates, exhibit higher impedance values from those of the bare metal in all the frequency regions, which is visually corroborated by the photographs depicted above (Figure 48). As time elapses, there is a slight reduction regarding the impedance values of system LDH-ED-1/0.75 in region I. The assignment of time constants for this system is comparable to that made for system LDH-NO₃-50/250. The most relevant results, however, are those corresponding to system LDH-ED-1/0.75-V since it presents two-time constants during the first 24 hours of immersion. The one observed at lower frequencies (10^{-1} - 10^1 Hz) can be ascribed either to the oxide film or ongoing corrosion processes, while the other in region III may be associated with the conversion film response. However, such response is no longer detected after 1 day of immersion. For longer immersion intervals, the time constants found at lower frequencies may be attributed to electrochemical corrosion reactions (10^1 Hz) or mass transport-controlled processes (10^{-2} - 10^{-1} Hz). It is important to note that this is the first case where there seems to be a barrier response provided by the electrodeposited LDH layer, suggesting that the cracks caused by H₂ evolution are probably minimized by the fixation/adsorption/precipitation of vanadates in the defected sites, during the first hours of immersion. As time elapses, the inhibiting effect of vanadates appears to vanish given the significant decrease of the impedance values in region I in respect to the initial ones, which is visually corroborated by the photographs in Figure 48. As shown above, system LDH-ED-1/0.75-V is slightly more corroded than LDH-ED-1/0.75 after being immersed in NaCl for 21 days.

Chapter 4: Holistic overview and critical analysis of the systems developed

The hydrothermal growth of the LDH conversion films on AA2024-T3 was based in a widespread procedure involving the immersion of the pretreated aluminum plates, under the afore-specified conditions, in bath solutions containing part of the reactants required for the process. Such species reacted with the Al^{3+} coming from the substrate, which acted as both reactant and seed for the synthesis, to form Zn/Al LDH phases. Three practical parameters were investigated in detail, namely reactant concentration, immersion time and temperature conditions. It became clear that more concentrated media was associated with thicker, more compact and evenly distributed films, whereas decreasing Zn^{2+} concentrations led to poorly covered surfaces with micrometre sized LDH agglomerates. The combination of high $\text{Zn}(\text{NO}_3)_2$ concentrations with long immersion times, however, resulted in flawed, cracked coatings. Taking this into consideration and prioritizing the quality of the protective system - LDH film and overcoatings - in terms of adhesion, a thinner and more uniformly distributed LDH layer took precedence over a thicker one with more developed flakes. The desired results were achieved when the conversion films were hydrothermally synthesized from more concentrated media, with short immersion periods. Concerning the bath temperature, it was shown to have a significant effect on the growth process and that it is feasible to form LDH layers at a temperature of 50°C . Nonetheless, the most crystalline phases were obtained at higher temperatures ($T \sim 100^\circ\text{C}$). The effect of the addition of sodium nitrate to the reaction media in the purity of the obtained phases was also studied, and was proven to be effective in preventing the development of Zn/Al LDHs containing anions other than nitrates.

Based on the results achieved, two different systems were selected in order to investigate their adherence to the underlying substrate and the influence of VO_x^{n-} ions on the corrosion inhibition of AA2024-T3 substrates, after a successful nitrate-vanadate replacement reaction: LDH- NO_3 -50/250 and LDH- NO_3 -500/2500 (their VO_x -intercalated counterparts being LDH- VO_x -50/250 and LDH- VO_x -500/2500 respectively). Both demonstrated remarkable results in terms of adhesion. As for the impedance measurements, the best anticorrosion performance was attributed to the films synthesized under more diluted conditions, for longer immersion periods, namely LDH- NO_3 -50/250 and LDH- VO_x -50/250, the latter being less efficient regarding long-term protection. Herein, LDHs were grown at the expense of the underlying substrate, which provides the aluminum cations to form such structures. Thus, a thinning of the naturally occurring aluminum oxide film is expected, especially for the LDH films grown under more concentrated conditions. Given the crucial role of the oxide layer in the corrosion protection performance, it was to be expected that thicker films were associated with poorer results. The corrosion retardation observed for system LDH- NO_3 -50/250 may be attributed to both NO_3^- and Zn^{2+} ions. In turn, the poor performance in terms of long-term protection observed for LDH- VO_x -50/250 may be related with the mechanical fragmentation of the LDH phase upon anion exchange reaction which, along with a thinning of the native oxide film, can lead to a dramatic failure when immersed in NaCl solutions.

The electrochemical synthesis of Zn/Al LDH films involved the direct deposition of Zn/Al LDH layers on the AA2024-T3 surface. Two distinct approaches were applied, the difference lying on the bath

composition. The first syntheses were performed with solutions containing several ratios and concentrations of $\text{Zn}(\text{NO}_3)_2$ and $\text{Al}(\text{NO}_3)_3$, while the subsequent tests involved the dissolution of a single salt in the growth solution to provide the divalent metal Zn^{2+} . The trivalent one (Al^{3+}), in turn, was provided by the aluminum plate. Initially, three synthetic conditions were optimized in order to obtain the purer, most crystalline LDH phase: the ratio and concentration of $\text{Zn}(\text{NO}_3)_2$ and $\text{Al}(\text{NO}_3)_3$, the applied potential and the solution pH. All the experiments were conducted at room temperature. Though it was possible to achieve LDH phases at less negative potentials when there was a higher content of aluminum in solution, the most crystalline ones were obtained when the most negative potentials were used (-1.8 V and -1.9 V vs Ag/AgCl). The resulting phase, however, appeared to consist of a Zn/Al LDH intercalated with OH^- or CO_3^{2-} ions instead of nitrates. Generally, the most effective approach to promote both the suppression of undesired zinc-related impurities and the formation of purer Zn/Al LDH phases seemed to be higher concentrations of Al^{3+} in the plating bath. The application of more negative deposition potentials also seemed to have a favourable effect on both processes. Regarding the effect of the solution pH, it was evident that the sharper and more intense LDH peaks were produced when the films were electrodeposited from the most acidic solutions (pH = 3), thus ruling out the more alkaline baths. When the electrodeposition was performed in acidic media, there was an increase in Al^{3+} concentration due to dissolution of the oxide layer naturally formed on aluminum surface. As soon as an appropriate negative potential was applied, water reduction took place and led to a local increase in the pH near the metallic substrate, thereby causing the Zn^{2+} and Al^{3+} ions to precipitate in the metal-solution interface. Contrastingly, as pH increases, the oxide layer becomes more stable and the amount of Al^{3+} ions coming from the substrate decreases. In addition, available Al^{3+} ions from the nitrate salt in solution will start to precipitate not only in the vicinity of the working electrode but also in the bulk solution, which might explain the poor results attained when the pH was adjusted to 4.2.

When the substrate became the source of Al^{3+} species, an additional parameter was investigated: deposition time. In the light of the obtained results, longer deposition appeared to be associated with the formation of multiple Zn/Al LDH phases with different Zn/Al molar ratios. As the deposition potential got more negative, such phenomenon was also observed for shorter times. Longer depositions also seemed associated with an increase in intensity of the peaks generated by zinc-containing impurities.

Regarding the SEM analysis of the electrodeposited structures, it was possible to identify an analogous morphology characterized by two distinct layers, the most superficial one being more or less delaminated and revealing the nano-sized platelet-like compounds between them. While the films obtained from the solutions with $\text{Zn}(\text{NO}_3)_2$ and $\text{Al}(\text{NO}_3)_3$ exhibited poorly-developed hexagonal-shaped crystallites covering the aluminum surface, the LDHs originated from the single-salt solutions were composed of perfectly-defined hexagons. The crystallite size appeared to decrease with lower applied potentials. Despite the ruptured, cracking surface of the films electrodeposited using the more negative potentials, the LDH layers appeared thicker and more compact in the non-delaminated area, in contrast to the hydrothermally grown films. Regarding the orientation of the LDH crystallites, most platelets seemed to grow perpendicularly oriented to the underlying substrate, although not as markedly as in the case of the films prepared by hydrothermal treatment.

The best results were accomplished with the following growth mixtures: a 12.5 mM $\text{Zn}(\text{NO}_3)_2$ + 9.4 mM $\text{Al}(\text{NO}_3)_3$ solution ($\text{Zn}^{2+}:\text{Al}^{3+}$ ratio = 1:0.75), and a 12.5 mM $\text{Zn}(\text{NO}_3)_2$ solution. The 5-minute depositions were carried out at an applied potential of -1.8 V vs Ag/AgCl and the pH was adjusted to 3 (systems LDH-ED-1/0.75 and LDH-ED-12.5 respectively). LDH-ED-1/0.75 evidenced poor results in terms of adherence since the outer layer was completely detached after the removal of the tape during the adhesion measurements. Given the unsuccessful attempt to intercalate VO_x^{n-} ions into LDH-ED-1/0.75, such procedure was not performed for LDH-ED-12.5 and the electrochemical tests were then only implemented for LDH-ED-1/0.75 and LDH-ED-1/0.75-V, corresponding to the system before and after the anion exchange reaction respectively. The most relevant results were those of the LDH-ED-1/0.75-V system, as it was the first case where there seemed to be a barrier response provided by the synthesized LDH layer. However, as time elapsed, the inhibiting effect attributed to vanadates appeared to vanish.

In conclusion, regarding the results obtained with the hydrothermal method, the combination of high $\text{Zn}(\text{NO}_3)_2$ concentrations with short immersion times led to the formation of Zn/Al- NO_3 LDH coatings with the desirable characteristics in terms of morphology, coverage and adhesion. However, the films grown under such conditions failed to effectively protect the underlying substrate against corrosion in the long term. This suggests that emphasis should be placed in the stability of the native oxide film when growing LDHs at the expense of the aluminum substrate. Growing thinner LDH layers from more diluted solutions, thereby maintaining high oxide stability, appears to be of greater importance than having higher amounts of Al^{3+} coming from the substrate (less stable oxide film) and consequently thicker coatings.

As for the films obtained through electrochemical deposition, no nitrate-intercalated seems to have been formed. Instead, the obtained phase appeared to consist of a Zn/Al LDH with OH^- or CO_3^{2-} in the interlamellar space. For this reason, the anion exchange reaction has proved ineffective for the electrodeposited films, which maintained the hydroxide/carbonate-intercalated structure. Adding NaNO_3 to the plating medium as a means to ensure there is an excessive amount of nitrates in it, as has been done for the hydrothermal treatment, may not be the best approach to overcome such problem given the major difference between the water and nitrates concentrations. Water reduction would have a more significant contribution to the cathodic generation of hydroxide ions in relation to the reduction of NO_3^- , and OH^- ions surpass nitrates in terms of anion-exchange selectivity in the case of Zn/Al LDHs. The contamination by easily intercalated CO_3^{2-} ions, in turn, may be prevented by using strict CO_2 -free conditions. Concerning the adhesion and morphology of the electrochemically synthesized films, several aspects need further improvement, such as the flawed surface and the detachment of the outer layer. The solution appears to involve the interplay between the applied potential and the deposition time. It seemed clear that the aforementioned parameters have a tremendous impact on the morphology of the obtained coating layers and probably alter the entire deposition mechanism. Therefore, it may be pertinent to study the hydrogen evolution reaction in more detail.

Chapter 5: Concluding remarks

While there has been an upsurge of interest in LDH-based conversion coatings and significant advancements have been achieved in this regard, there are still a lot of relevant requirements to be met for these thin films to be adopted by the industrial sector. There must be improvements concerning the adhesion properties, substrate coverage and purity/crystallinity of the obtained LDH phases, critical factors for the quality and effectiveness of the protective system as a whole. Such upgrading process entails a refinement of the synthetic methodologies and the practical parameters involved, such as the reaction time, pH and temperature conditions, reactants concentrations, among others.

Although the optimal conditions to grow Zn/Al LDH conversion films with the desirable characteristics have not yet been reached, this investigation provides valuable information concerning the effect of the synthesis parameters in the properties of the obtained LDH coatings on AA2024-T3.

In the case of the hydrothermal treatment, it was concluded that promising results in terms of XRD and SEM analysis do not necessarily imply a satisfactory anti-corrosion performance. It was also found that while the generation of LDHs directly from the dual-purpose substrate - serving as both reactant and seed for the synthesis - benefits the adhesion, maintaining the native oxide film stability is of the utmost importance. For this reason, the hydrothermally grown LDH coatings might have to be combined with thicker oxide layers (anodising) or different pre-treatments in future experiments.

As for the electrochemical deposition, it will be necessary to alter the synthesis conditions in order to intercalate the desired anionic species into the LDH structure and improve the morphology of the electrodeposited films. In addition to the detailed study of the hydrogen evolution reaction, exploring different electrochemical approaches to grow the LDH coatings on AA2024 substrates, such as the electrophoretic deposition of Zn/Al LDH particles dispersed in solution, might also be of relevance.

All things considered, the two applied methodologies present several advantages over more-established preparative techniques of LDHs, like co-precipitation. Both constitute well-suited, cost-effective, less time-consuming, one-step routes for the direct fabrication of films with controllable properties on aluminum surface. The deposit characteristics can be fine-tuned by varying the process parameters. Setup simplicity and rapid film formation are also appealing aspects. Additionally, although only lab-scale experiences were performed during this project, both methods, after fully and properly optimised, are scalable for extensive production. In spite of being far from achieving fool-proof status, the results presented here provide a good starting point from which to proceed with additional investigation.

Bibliographic references

1. M. L. Zheludkevich, J. Tedim, M. G. S. Ferreira, ““Smart” coatings for active corrosion protection based on multi-functional micro and nanocontainers”, *Electrochimica Acta*, 82, 314-323, 2012.
2. J. R. Davis, *Corrosion Of Aluminum and Aluminum Alloys*, ASM International, 262, 1999.
3. A. Makhlof (Ed.), *Handbook of Smart Coatings for Materials Protection*, Woodhead Publishing Series in Metals and Surface Engineering, 64, 659, 2014.
4. A. F. Carreira, A. M. Pereira, E. P. Vaz, A. M. Cabral, T. Ghidini, L. Pigliaru, T. Rohr, “Alternative corrosion protection pretreatments for aluminum alloys”, *Journal of Coatings Technology and Research*, 14 (4), 879-892, 2017.
5. M. Fontana, *Corrosion Engineering*, McGraw-Hill, 576, 1987.
6. Z. Ahmad, *Principles of Corrosion Engineering and Corrosion Control*, Elsevier Science & Technology Books, 660, 2006.
7. S. Benavides, *Corrosion control in the aerospace industry*, Woodhead Publishing, 319, 2014.
8. J. N. Balaraju, “Assessment of chromate and chromate-free conversion coatings for the corrosion protection of aerospace aluminum alloy”, *Workshop on Advanced Materials and Manufacturing Methods, National Institute of Technology*, Tiruchirappalli, 2013.
9. A. Katunin, K. Krukiewicz, A. Herega, G. Catalanotti, "Concept of a Conducting Composite Material for Lightning Strike Protection", *Advanced Materials Science*, 16(2), 32-46, 2016.
10. M. Maria, "Advanced composite materials of the future in aerospace industry", 5(3), 139-150, 2013.
11. J. G. Kaufman, *Introduction to Aluminum Alloys and Tempers*, ASM International, 237, 2000.
12. P. A. Schweitzer, *Fundamentals of Metallic Corrosion: Atmospheric and Media Corrosion of Metals, Second Edition*, CRC Press, 752, 2006.
13. P. Rambabu, N. Eswara Prasad, V. V. Kutumbarao, R. J. H. Wanhill, "Aluminium Alloys for Aerospace Applications", *Aerospace Materials and Material Technologies: Volume 1: Aerospace Materials*, Springer; 29-52, 2017.
14. R. G. Buchheit, "A Compilation of Corrosion Potentials Reported for Intermetallic Phases in Aluminum Alloys", *Journal of The Electrochemical Society*, 142, 3994-3996, 1995.
15. R. G. Buchheit, R. K. Boger, M. C. Carroll, R. M. Leard, C. Paglia, J. L. Searles, "The Electrochemistry of Intermetallic Particles and Localized Corrosion in Al Alloys", *The Journal of The Minerals, Metals & Materials Society*, 53(7), 29-33, 2001.
16. M. B. Vukmirovic, N. Dimitrov, K. S. Sieradski, "Dealloying and Corrosion of Al Alloy 2024-T3", *Journal of The Electrochem Society*, 149(9), B428-B439, 2002.

Bibliographic references

17. N. Birbilis, R. G. Buchheit, "Electrochemical Characteristics of Intermetallic Phases in Aluminum Alloys", *Journal of The Electrochemical Society*, 152(4), B140-B151, 2005.
18. T. Hashimoto, X. Zhang, X. Zhou, P. Skeldon, S. J. Haigh, G. E. Thompson, "Investigation of dealloying of S phase (Al₂CuMg) in AA2024-T3 aluminium alloy using high resolution 2D and 3D electron imaging", *Corrosion Science*, 103, 157-164, 2015.
19. R. W. Revie, H. H. Uhlig, *Corrosion and Corrosion Control: An Introduction to Corrosion Science and Engineering*, Wiley Interscience, 512, 2008.
20. M. Pourbaix, "Atlas of electrochemical equilibrium in aqueous solutions", *National Association of Corrosion Engineers*, Houston, Texas, 1974.
21. L. J. Korb (Ed.), *ASM Handbook Volume 13: Corrosion*, ASM Handbooks, 3455, 1992.
22. A. Groysman, *Corrosion for Everybody*, Springer Science+Business Media, 377, 2010.
23. P. R. Roberge, *Handbook of Corrosion Engineering*, McGraw-Hill, 976, 2012.
24. P. A. Schweitzer, *Corrosion of Linings & Coatings: Cathodic and Inhibitor Protection and Corrosion Monitoring*, *Corrosion Engineering Handbook*, CRC Press, 570, 2006.
25. X. D. Zhao, J. Yang J, X. Q. Fan, "Review on Research and Progress of Corrosion Inhibitors", *Applied Mechanics and Materials*, 44-47, 4063-4066, 2010.
26. M. L. Zheludkevich, "Self-healing Anticorrosion Coatings", *Self-healing Materials: Fundamentals, Design Strategies and Applications* (S. K. Ghosh, Ed.), Wiley-VCH, 101-139, 2009.
27. R. G. Buchheit, H. Guan, S. Mahajanam, F. Wong, "Active corrosion protection and corrosion sensing in chromate-free organic coatings", *Progress in Organic Coatings*, 47, 174-182, 2003.
28. S. P. V. Mahajanam, "Characterization of Inhibitor Release from Zn-Al-[V₁₀O₂₈]⁶⁻ Hydrotalcite Pigments and Corrosion Protection from Hydrotalcite-Pigmented Epoxy Coatings", *Corrosion*, 64(3), 230-240, 2008.
29. M. Iannuzzi, G. S. Frankel, "Mechanisms of corrosion inhibition of AA2024-T3 by vanadates", *Corrosion Science*, 49(5), 2371-2391, 2007.
30. K. D. Ralston, S. Chrisanti, T. L. Whitmer, R. G. Buchheit, "Corrosion Inhibition of Aluminum Alloy 2024-T3 by Aqueous Vanadium Species", *Journal of The Electrochemical Society*, 155(7), C350, 2008.
31. J. Tedim, S. K. Poznyak, A. Kuznetsova, D. Raps, T. Hack, M. L. Zheludkevich, M. G. S. Ferreira, "Enhancement of Active Corrosion Protection via Combination of Inhibitor-Loaded Nanocontainers", *ACS Applied Materials & Interfaces*, 2, 1528-1535, 2010.
32. T. P. Schuman, "Protective Coatings for Aluminum Alloys", *Handbook of Environmental Degradation of Materials: Second Edition* (Myer Kutz, Ed.), Elsevier Inc., 503-538, Sep 2012.
33. C. M. Cotell, J. A. Sprague, F. A. Smidt, Jr. (Eds.), "Surface Engineering of Aluminum and

- Aluminum Alloys”, *ASM Handbook Volume 5: Surface Engineering Surface Engineering Volume 5*, ASM International, 784-804, 1994.
- 34.** M. F. Montemor, “Functional and smart coatings for corrosion protection: A review of recent advances”, *Surface and Coatings Technology*, 258, 17-37, 2014.
- 35.** J. Tedim, M. L. Zheludkevich, A. C. Bastos, A. N. Salak, A. D. Lisenkov, M. G. S. Ferreira, “Influence of preparation conditions of Layered Double Hydroxide conversion films on corrosion protection”, *Electrochimica Acta*, 117, 164 – 171, 2014.
- 36.** D. G. Shchukin, M. Zheludkevich, K. Yasakau, S. Lamaka, M. G. S. Ferreira, H. Möhwald, “Layer-by-Layer Assembled Nanocontainers for Self-Healing Corrosion Protection”, *Advanced Materials*, 18 (13), 1672–1678, 2006.
- 37.** M. L. Zheludkevich, S. K. Poznyak, L. M. Rodrigues, D. Raps, T. Hack, L. F. Dick, T. Nunes, M. G. S. Ferreira, “Active protection coatings with layered double hydroxide nanocontainers of corrosion inhibitor”, *Corrosion Science*, 52 (2), 602-611, 2010.
- 38.** M. Kendig, M. Hon, L. Warren, “‘Smart’ corrosion inhibiting coatings”, *Progress in Organic Coatings*, 47 (3–4), 183-189, 2003.
- 39.** M. L. Zheludkevich, J. Tedim, C. S. R. Freire, S. C. M. Fernandes, S. Kallip, A. Lisenkov, A. Gandini, M. G. S. Ferreira, “Self-healing protective coatings with “green” chitosan based pre-layer reservoir of corrosion inhibitor”, *Journal of Materials Chemistry*, 21, 4805, 2011.
- 40.** J. Carneiro, J. Tedim, S. C. M. Fernandes, C. S. R. Freire, A. J. D. Silvestre, A. Gandini, M. L. Zheludkevich, M. G. S. Ferreira, “Chitosan-based self-healing protective coatings doped with cerium nitrate for corrosion protection of aluminum alloy 2024”, *Progress in Organic Coatings*, 75 (1–2), 8-13, 2012.
- 41.** J. Carneiro, J. Tedim, S. C. M. Fernandes, C. S. R. Freire, A. Gandini, M. G. S. Ferreira, M. L. Zheludkevich, “Chitosan as a Smart Coating for Controlled Release of Corrosion Inhibitor 2-Mercaptobenzothiazole”, *ECS Electrochemistry Letters*, 2 (6), C19 - C22, 2013.
- 42.** J. Carneiro, J. Tedim, S. C. M. Fernandes, C. S. R. Freire, A. Gandini, M. G. S. Ferreira, M. L. Zheludkevich, “Functionalized chitosan-based coatings for active corrosion protection”, *Surface and Coatings Technology*, 226, 51–59, 2013.
- 43.** F. Mansfeld, V. Wang, H. Shih, "Development of ‘Stainless Aluminum’". *Journal of The Electrochemical Society*, 138(12), L74-L75, 1991.
- 44.** M. Dabala, L. Armelao, A. Buchberger, I. Calliari, "Cerium-based conversion layers on aluminum alloys", *Applied Surface Science*, 172, 312-322, 2001.
- 45.** W. G. Fahrenholtz, M. J. O’Keefe, H. Zhou, J. T. Grant, "Characterization of cerium-based conversion coatings for corrosion protection of aluminum alloys", *Surface and Coatings Technology*, 155, 208-213, 2002.

46. M. Dabalà, E. Ramous, M. Magrini, "Corrosion resistance of cerium-based chemical conversion coatings on AA5083 aluminium alloy", *Materials and Corrosion*, 55(5), 381-386, 2004.
47. B. F. Rivera, B. Y. Johnson, M. J. O'Keefe, W. G. Fahrenholtz, "Deposition and characterization of cerium oxide conversion coatings on aluminum alloy 7075-T6", *Surface and Coatings Technology*, 176, 349-356, 2004.
48. P. Campestrini, H. Terry, A. Hovestad, J. H. W. de Wit, "Formation of a cerium-based conversion coating on AA2024: relationship with the microstructure", *Surface and Coatings Technology*, 176, 365-381, 2004.
49. A. Decroly, J. Petitjean, "Study of the deposition of cerium oxide by conversion on to aluminium alloys", *Surface and Coatings Technology*, 194(1), 1-9, 2005.
50. J. F. Ying, B. J. Flinn, M. Y. Zhou, P. C. Wong, K. A. R. Mitchell, T. Fostert, "Optimization of zinc phosphate coating on 7075-T6 aluminum alloy", *Progress in Surface Science*, 50, 259-267, 1995.
51. D. Susac, X. Sun, R. Y. Li, K. C. Wong, P. C. Wong, K. A. R. Mitchell, R. Champaneria, "Microstructural effects on the initiation of zinc phosphate coatings on 2024-T3 aluminum alloy", *Applied Surface Science*, 239(1), 45-59, 2004.
52. J. Bibber, "An update on chrome-free pretreatments for aluminum", *Metal Finishing*, 96(4), 30-31, 1998.
53. J. W. Bibber, "An overview of nonhexavalent chromium conversion coatings - Part I: aluminum and its alloys", *Metal Finishing*, 99(12), 15-22, 2001.
54. A. E. Hughes, J. D. Gorman, T. G. Harvey, A. E. Galassi, G. E. McAdam, "Development of Permanganate-Based Coatings on Aluminum Alloy 2024-T3", *Corrosion*, 62(9), 773-780, 2006.
55. S. A. Kulinich, A. S. Akhtar, P. C. Wong, K. C. Wong, K. A. R. Mitchell, "Growth of permanganate conversion coating on 2024-Al alloy", *Thin Solid Films*, 515(23), 8386-8392, 2007.
56. T. Schram, G. Goeminne, H. Terry, W. Vanhoolst, P. V. Espen, "Study of the Composition of Zirconium based Chromium free Conversion Layers on Aluminium", *Transactions of the IMF*, 73(3), 91-95, 1995.
57. L. Fedrizzi, F. Deflorian, P. L. Bonora, "Corrosion behaviour of fluotitanate pretreated and painted aluminium sheets", *Electrochimica Acta*, 42(6), 969-978, 1997.
58. L. Fedrizzi, A. Bianchi, F. Deflorian, S. Rossi, P. L. Bonora, "Effect of chemical cleaning on the corrosion behaviour of painted aluminium alloys". *Electrochimica Acta*, 47(13-14), 2159-2168, 2002.
59. H. Guan, R. G. Buchheit, "Corrosion Protection of Aluminum Alloy 2024-T3 by Vanadate Conversion Coatings", *Corrosion*, 60(3), 284-296, 2004.
60. F. Mansfeld, Y. Wang, H. Shih, "The Ce-Mo process for the development of a stainless aluminum", *Electrochimica Acta*, 37(12), 2277-2282, 1992.

61. F. Mansfeld, F. J. Pérez, "Surface modification of aluminum alloys in molten salts containing CeCl_3 ", *Thin Solid Films*, 270(1-2), 417-421, 1995.
62. C. Wang, F. Jiang, F. Wang, "Cerium Chemical Conversion Coating for Aluminum Alloy 2024-T3 and its Corrosion Resistance", *Corrosion*, 60(3), 237-243, 2004.
63. L. E. M. Palomino, I. V. Aoki, M. H. G., "Microstructural and electrochemical characterization of Ce conversion layers formed on Al alloy 2024-T3 covered with Cu-rich smut", *Electrochimica Acta*, 51(26), 5943-5953, 2006.
64. C. B. Breslin, G. Treacy, W. M. Carroll, "Studies on the passivation of aluminium in chromate and molybdate solutions". *Corrosion Science*, 36(7), 1143-1154, 1994.
65. K. C. Emregül, A. A. Aksüt, "The effect of sodium molybdate on the pitting corrosion of aluminum", *Corrosion Science*, 45(11), 2415-2433, 2003.
66. B. A. Shaw, G. D. Davis, T. L. Fritz, "A Molybdate Treatment for Enhancing the Passivity of Aluminum in Chloride-Containing Environments". *Journal of The Electrochemical Society*, 137(1), 359-360, 1990.
67. R. B. Leggat, W. Zhang, R. G. Buchheit, S. R. Taylor, "Performance of Hydrotalcite Conversion Treatments on AA2024-T3 When Used in a Coating System", *Corrosion*, 58(4), 322, 2002.
68. W. Zhang, R. G. Buchheit, "Hydrotalcite Coating Formation on Al-Cu-Mg Alloys from Oxidizing Bath Chemistries", *Corrosion*, 58(7), 591, 2002.
69. R. G. Buchheit, S. B. Mamidipally, P. Schmutz, H. Guan, "Active Corrosion Protection in Ce-Modified Hydrotalcite Conversion Coatings", *Corrosion*, 58(1), 3, 2002.
70. J. Tedim, M. L. Zheludkevich, A. N. Salak, A. Lisenkov, M. G. S. Ferreira, "Nanostructured LDH-container layer with active protection functionality", *Journal of Materials Chemistry*, 21 (39), 15464-15470, 2011.
71. F. Zhang, C. Zhang, L. Song, R. Zeng, Z. Liu, H. Cui, "Corrosion of in-situ grown MgAl-LDH coating on aluminum alloy", *Transactions of Nonferrous Metals Society of China*, 25(10), 3498-3504, 2015.
72. Y. Liu, T. Yu, R. Cai, Y. Li, W. Yang, J. Caro, "One-pot synthesis of NiAl- CO_3 LDH anti-corrosion coatings from CO_2 -saturated precursors", *RSC Advances*, 5(37), 29552-29557, 2015.
73. C. Zhang, X. Luo, X. Pan, L. Liao, X. Wu, Y. Liu, "Self-healing Li-Al layered double hydroxide conversion coating modified with aspartic acid for 6N01 Al alloy", *Applied Surface Science*, 394, 275-281, 2017.
74. J. Wu, D. Peng, Y. He, X. Du, Z. Zhang, B. Zhang, X. Li, Y. Huang, "In Situ Formation of Decavanadate-Intercalated Layered Double Hydroxide Films on AA2024 and their Anti-Corrosive Properties when Combined with Hybrid Sol Gel Films", *Materials (Basel)*, 10(4), 426, 2017.

75. K. A. Yasakau, A. Kuznetsova, S. Kallip, M. Starykevich, J. Tedim, M. G. S. Ferreira, M. L. Zheludkevich, "A novel bilayer system comprising LDH conversion layer and sol-gel coating for active corrosion protection of AA2024", *Corrosion Science*, 143, 299-313, 2018.
76. M. A. Iqbal, M. Fedel, "Effect of Synthesis Conditions on the Controlled Growth of MgAl-LDH Corrosion Resistance Film: Structure and Corrosion Resistance Properties", *Coatings*, 9(1), 30, 2019.
77. M. A. Iqbal, L. Sun, A. M. LaChance, Hao Ding, M. Fedel, "In situ growth of a CaAl-NO₃-layered double hydroxide film directly on an aluminum alloy for corrosion resistance", *Dalton Transactions*, 2019.
78. S. Li, Y. Sheng, D. Liu, L. Fan, X. Zheng, J. Yang, "One-step fabrication of oriented Mg/Al-layered double hydroxide film on magnesium substrate with urea hydrolysis and its corrosion resistance", *Composite Interfaces*, 19(8), 489-498, 2012.
79. R. Zeng, X. Li, Z. Liu, F. Zhang, S. Li, H. Cui, "Corrosion resistance of Zn-Al layered double hydroxide/poly(lactic acid) composite coating on magnesium alloy AZ31", *Frontiers of Material Science*, 9(4), 355-365, 2015.
80. X. Zhang, P. Jiang, C. Zhang, B. Buhe, B. Liu, Y. Zhao, T. Zhang, G. Meng, F. Wang, "Anticorrosion Performance of LDH Coating Prepared by CO₂ Pressurization Method", *International Journal of Corrosion*, 1-10, 2018.
81. T. N. Shulha, M. Serdechnova, S. V. Lamaka, D. C. F. Wieland, K. N. Lapko, M. L. Zheludkevich, "Chelating agent-assisted in situ LDH growth on the surface of magnesium alloy", *Scientific Reports*, 8(1), 2018.
82. K. Hoshino, S. Furuya, R. G. Buchheit, "Effect of NO₃⁻ Intercalation on Corrosion Resistance of Conversion Coated Zn-Al-CO₃ LDHs on Electrogalvanized Steel", *Journal of The Electrochemical Society*, 165(9), C461-C468, 2018.
83. A. Mikhailau, H. Maltanova, S. K. Poznyak, A. N. Salak, M. L. Zheludkevich, K. A. Yasakau, M. G. S. Ferreira, "One-step synthesis and growth mechanism of nitrate intercalated ZnAl LDH conversion coatings on zinc", *Chemical Communications*, 48, 2019.
84. E. Manasse, *Atti della Società Toscana di Scienze Naturali*, 24, 92, 1915.
85. W. Feitknecht, M. Gerber, *Helvetica Chimica Acta*, 25, 131, 1942.
86. R. Allmann, *Acta Crystallographica*, Sect. B, 24, 972, 1968.
87. H. G. W. Taylor, *Mineralogical Magazine*, 37, 338, 1969.
88. H. G. W. Taylor, *Mineralogical Magazine*, 39, 338, 1973.
89. X. Duan, D. G. Evans, "Layered Double Hydroxides", *Structure and Bonding*, 119, Springer, 2006.
90. V. Rives (Ed.), *Layered Double Hydroxides: Present and Future*, Nova Science Publishers, Inc., 513, 2001.

91. A. I. Khan, D. O'Hare, "Intercalation chemistry of layered double hydroxides: recent developments and applications", *Journal of Materials Chemistry*, 12 (11), 3191-3198, 2002.
92. Y. Kuang, L. Zhao, S. Zhang, F. Zhang, M. Dong, S. Xu, "Morphologies, preparations and applications of layered double hydroxide micro-/nanostructures", *Materials*, 3 (12), 5220-5235, 2010.
93. P. S. Braterman, Z. P. Xu, F. Yarberry, "Layered Double Hydroxides (LDHs)", *Handbook of Layered Materials* (S. M. Auerbach, K. A. Carrado, P. K. Dutta, Eds.), Marcel Dekker, Inc., 373-474, 2004.
94. J. J. Bravo-Suárez, E. A. Páez-Mozo, S. T. Oyama, "Review of the synthesis of layered double hydroxides: a thermodynamic approach", *Química Nova*, 27 (4), 601-614, 2004.
95. C. Forano, T. Hibino, F. Leroux, C. Taviot-Guého, "Layered Double Hydroxides", *Handbook of Clay Science* (F. Bergaya, B. K. G. Theng, G. Lagaly, Eds.), Elsevier, 1021-1096, 2006.
96. X. Guo, F. Zhang, D. G. Evans, X. Duan, "Layered double hydroxide films: Synthesis, properties and applications", *Chemical Communications*, 46(29), 5197-5210, 2010.
97. U. Unal, "Short-time hydrothermal synthesis and delamination of ion exchangeable Mg/Ga layered double hydroxides", *Journal of Solid State Chemistry*, 180(9), 2525-2533, 2007.
98. J. Tedim, M. L. Zheludkevich, A. C. Bastos, A. N. Salak, J. Carneiro, F. Maia, A. D. Lisenkov, A. B. Oliveira, M. G. S. Ferreira, "Effect of Surface Treatment on the Performance of LDH Conversion Films", *ECS Electrochemistry Letters*, 3 (1), C4 - C8, 2014.
99. J. Tedim, A. C. Bastos, S. Kallip, M. L. Zheludkevich, M. G. S. Ferreira, "Corrosion protection of AA2024-T3 by LDH conversion films. Analysis of SVET results", *Electrochimica Acta*, 210, 215-224, 2016.
100. T. Galvão, C. Neves, M. L. Zheludkevich, J. Gomes, J. Tedim, M. Ferreira, "How DFT Surface Energies May Explain the Morphology of Particles, Nanosheets and Conversion Films based on Layered Double Hydroxides", *The Journal of Physical Chemistry C*, 121(4), 2016.
101. L. Liao, N. Zhao, Z. Xia, "Hydrothermal synthesis of Mg-Al layered double hydroxides (LDHs) from natural brucite and Al(OH)₃", *Materials Research Bulletin*, 47, 3897-3901, 2012.
102. Z. P. Xu, G. Q. Lu, "Hydrothermal Synthesis of Layered Double Hydroxides (LDHs) from Mixed MgO and Al₂O₃: LDH Formation Mechanism", *Chemistry of Materials*, 17(5), 1055-1062, 2005.
103. X. Guo, S. Xu, L. Zhao, W. Lu, F. Zhang, D. G. Evans, X. Duan, "One-Step Hydrothermal Crystallization of a Layered Double Hydroxide/Alumina Bilayer Film on Aluminum and Its Corrosion Resistance Properties", *Langmuir*, 25(17), 9894-9897, 2009.
104. G. Abellán, J. A. Carrasco, E. Coronado, J. P. Pietro-Ruiz, H. García, "In-Situ Growth of Ultrathin Films of NiFe-LDHs: Towards a Hierarchical Synthesis of Bamboo-Like Carbon Nanotubes", *Advanced Materials Interfaces*, 1(6), 2014.
105. F. Zhang, C. Zhang, L. Song, R. C. Zeng, L. Y. Cui, H. Z. Cui, "Corrosion resistance of

superhydrophobic mg-al layered double hydroxide coatings on aluminum alloys", *Acta Metallurgica Sinica (English Letters)*, 28(11), 1373-138, 2015.

106. F. Wu, J. Liang, Z. Peng, B. Liu, "Electrochemical deposition and characterization of Zn-Al layered double hydroxides (LDHs) films on magnesium alloy", *Applied Surface Science*, 313, 834-840, 2014.

107. A. Lavacchi, H. Miller, F. Vizza, *Nanotechnology in Electrocatalysis for Energy*, Springer Science+Business Media, 334, 2013.

108. M. Shao, R. Zhang, Z. Li, M. Wei, D. G. Evans, X. Duan, "Layered double hydroxides toward electrochemical energy storage and conversion: design, synthesis and applications", *Chemical Communications*, 51(88), 2015.

109. E. Scavetta, B. Ballarin, M. Gazzanob, D. Tonelli, "Electrochemical behaviour of thin films of Co/Al layered double hydroxide prepared by electrodeposition", *Electrochimica Acta*, 54, 1027-1033, 2009.

110. J. Syu, J. Uan, M. Lin, Z. Lin, "Optically transparent Li-Al-CO₃ layered double hydroxide thin films on an AZ31 Mg alloy formed by electrochemical deposition and their corrosion resistance in a dilute chloride environment", *Corrosion Science*, 68, 238-248, 2013.

111. V. Gupta, S. Gupta, N. Miura, "Al-substituted α -zinc cobalt hydroxide synthesized by potentiostatic deposition method as an electrode material for redox-supercapacitors", *Journal of Power Sources*, 177(2), 685-689, 2008.

112. Y. Li, L. Zhang, X. Xiang, D. Yan, F. Li, "Engineering of ZnCo-layered double hydroxide nanowalls toward high-efficiency electrochemical water oxidation", *Journal of Materials Chemistry A*, 2(33), 13250, 2014.

113. M. S. Yarger, E. M. P. Steinmiller, K.-S. Choi, "Electrochemical Synthesis of Zn-Al Layered Double Hydroxide (LDH) Films", *Inorganic Chemistry*, 47, 5859-5865, 2008.

114. D. L. Bish, *Bulletin de Minéralogie*, 103, 175, 1980.

115. G. Fan, F. Li, D. G. Evans, X. Duan, "Catalytic applications of layered double hydroxides: recent advances and perspectives", *Chemical Society Reviews*, 20, 2014.

116. S. Nichitus, G. Calin, A. Burlui, V. Burlui, "Layered Double Hydroxides (LDHs) Type Materials Used in Water Treatment", *Key Engineering Materials*, 660, 273-278, 2015.

117. N. Chubar, R. Gilmour, V. Gerda, M. Mičušík, M. Omastova, K. Heister, P. Man, J. Fraissard, V. Zaitsev, "Layered double hydroxides as the next generation inorganic anion exchangers: Synthetic methods versus applicability", *Advances in Colloid and Interface Science*, 245, 62-80, 2017.

118. X. Bi, H. Zhang, L. Dou, "Layered Double Hydroxide-Based Nanocarriers for Drug Delivery", *Pharmaceutics*, 6, 298-332, 2014.

119. A. N. Salak, J. Tedim, A. I. Kuznetsova, M. L. Zheludkevich, M. G. S. Ferreira, "Anion exchange in

- Zn–Al layered double hydroxides: In situ X-ray diffraction study”, *Chemical Physics Letters*, 495, 73–76, 2010.
- 120.** GAMRY Instruments Application Note: Basics of Electrochemical Impedance Spectroscopy, April, 2018.
- 121.** J. R. Scully, D. W. Taylor, “Electrochemical Methods of Corrosion Testing”, *ASM Handbook Volume 13 Corrosion*, Metals Park, OH: ASM International, 481-483, 1987.
- 122.** A. Forsgren, *Corrosion Control Through Organic Coatings*, CRC Press, 256, 2006
- 123.** ISO 2409:2013, Paints and varnishes - Cross-cut test, International Organization for Standardization, Geneva, Switzerland.
- 124.** j. Lin, J. Uan, C. Wu, H. Huang, "Direct growth of oriented Mg-Fe layered double hydroxide (LDH) on pure Mg substrates and in vitro corrosion an cell adhesion testing of LDH-coated Mg samples", *Journal of Materials Chemistry*, 21(13), 5011-5020, 2011.
- 125.** T. M. Letcher, *Development and Applications in Solubility*, Royal Society of Chemistry, 2007.
- 126.** A. N. Salak, A. D. Lisenkov, M. L. Zheludkevich, M. G. S. Ferreira, “Carbonate-Free Zn-Al (1:1) Layered Double Hydroxide Film Directly Grown on Zinc-Aluminum Alloy Coating”, *ECS Electrochemistry Letters*, 3 (1), C9 – C11, 2014.
- 127.** A. K. Zak, R. Razali, W. H. Majid, M. Darroudi, "Synthesis and characterization of a narrow size distribution of zinc oxide nanoparticles", *International Journal of Nanomedicine*, 6(1), 1399-1403, 2011.
- 128.** M. Paunovic, M. Schlesinger, *Fundamentals of Electrochemical Deposition Second Edition*, Wiley, 368, 2006.
- 129.** H. D. B. Jenkins, K. P. Thakur, "Reappraisal of thermochemical radii for complex ions", *Journal of Chemical Education*, 56(9), 576, 1979.
- 130.** Y. Wang, H. Gao, "Compositional and structural control on anion sorption capability of layered double hydroxides (LDHs)", *Journal of Colloid and Interface Science*, 301(1), 19-26, 2006.
- 131.** M. Tong, H. Chen, Z. Yang, R. Wen, "The Effect of Zn-Al-Hydrotalcites Compositied with Calcium Stearate and β -Diketone on the Thermal Stability of PVC", *International Journal of Molecular Sciences*, 12(3), 1756-1766, 2011.
- 132.** T. Hibino, "Anion Selectivity of Layered Double Hydroxides: Effects of Crystallinity and Charge Density", *European Journal Inorganic Chemistry*, 6, 722-730, 2018.
- 133.** Q. Meng, T. Ramgopal, G. S. Frankel, "The Influence of Inhibitor Ions on Dissolution Kinetics of Al and Mg Using the Artificial Crevice Technique", *Electrochemical and Solid-State Letters*, 5(2), B1-B4, 2002.

Annex

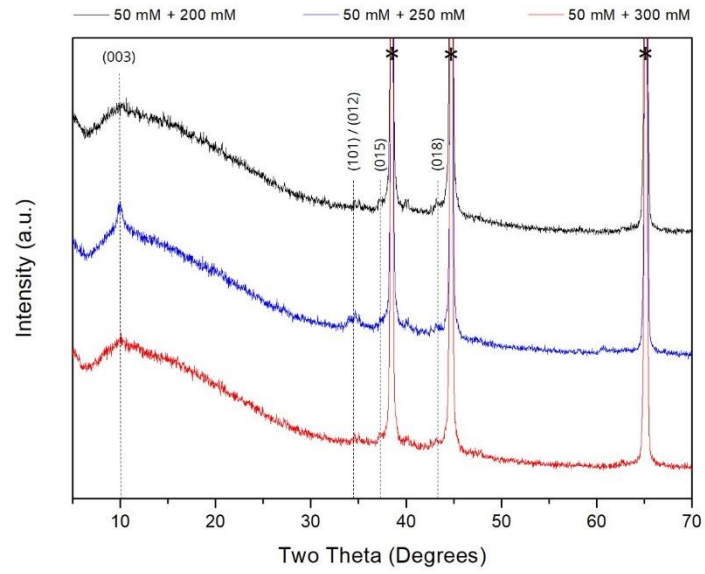


Figure A1 XRD patterns obtained for LDH conversion films grown on the AA2024 substrates through hydrothermal synthesis (~100 °C, 30 min) using solutions with 50 mM Zn(NO₃)₂ and varying concentrations of NaNO₃.

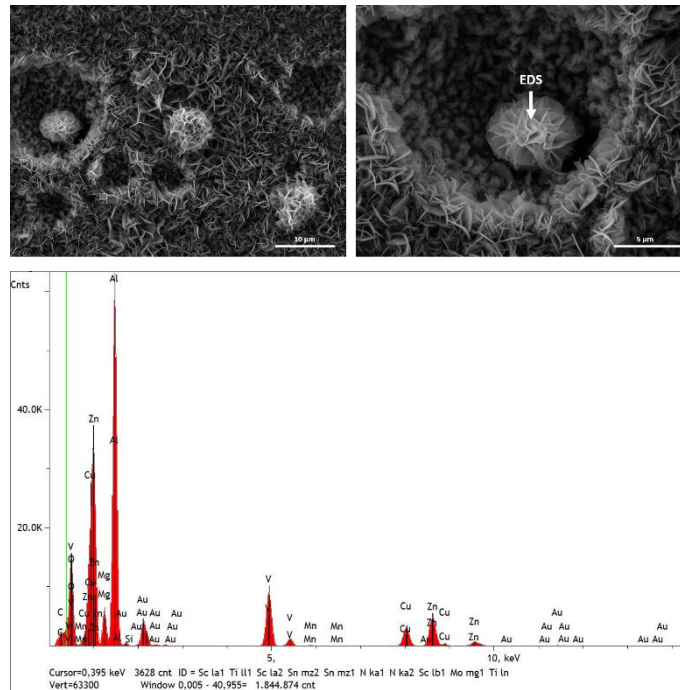


Figure A2 SEM/EDS data acquired for system LDH-VO_x-50/250.

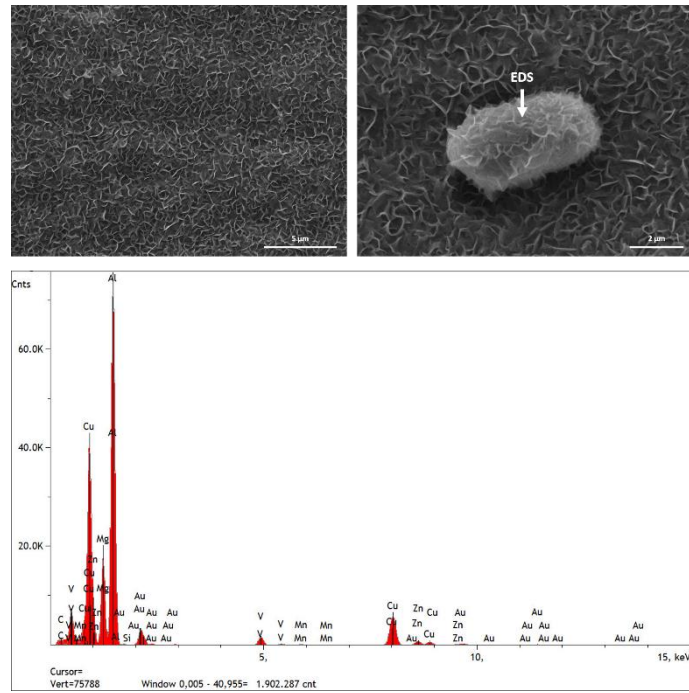


Figure A3 SEM/EDS data acquired for system LDH-VO_x-500/2500.

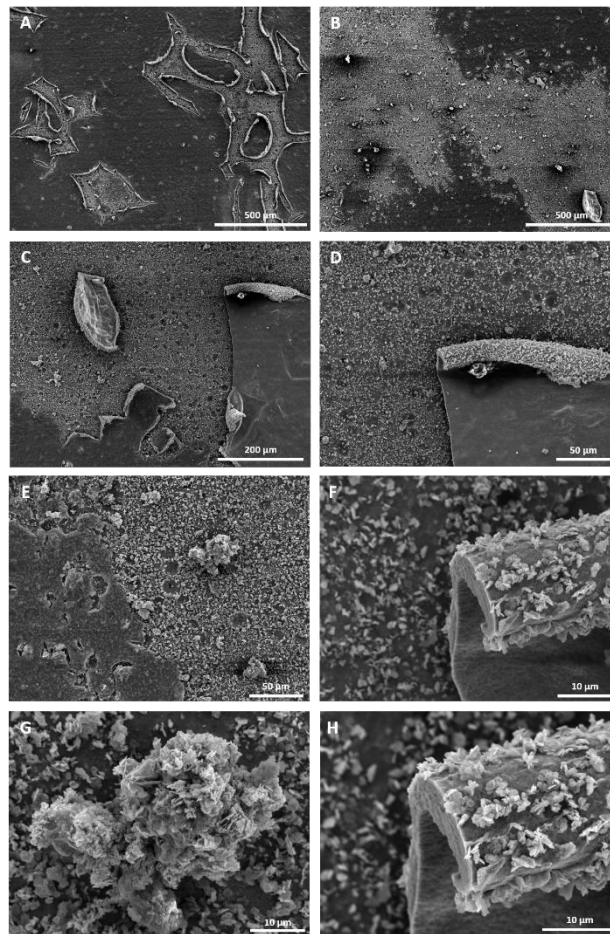


Figure A4 SEM images obtained for the LDH conversion film electrochemically deposited on a AA2024 substrate from a 12,5 mM Zn(NO₃)₂ solution (pH = 3). The deposition was carried out at -1,8 V vs Ag/AgCl, in RT conditions, during 10 min.

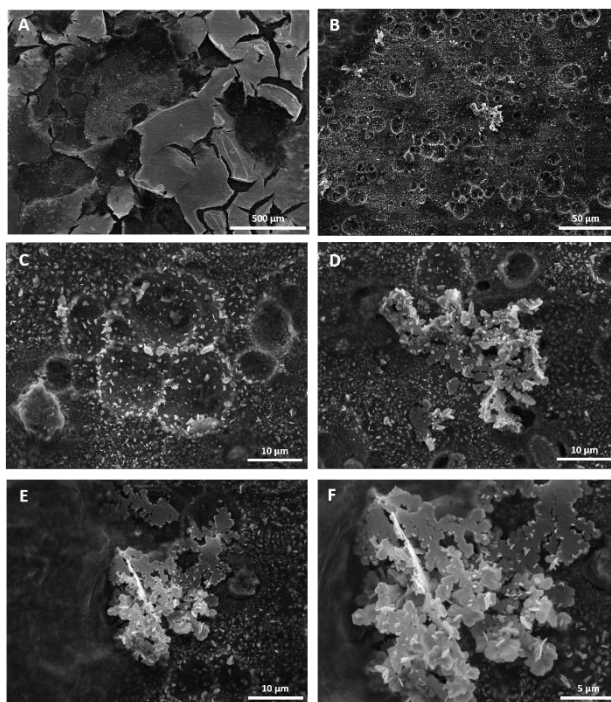


Figure A5 SEM images obtained for the LDH conversion film electrochemically deposited on a AA2024 substrate from a 12,5 mM $\text{Zn}(\text{NO}_3)_2$ solution (pH = 3). The deposition was carried out at -1,8 V vs Ag/AgCl, in RT conditions, during 15 min.

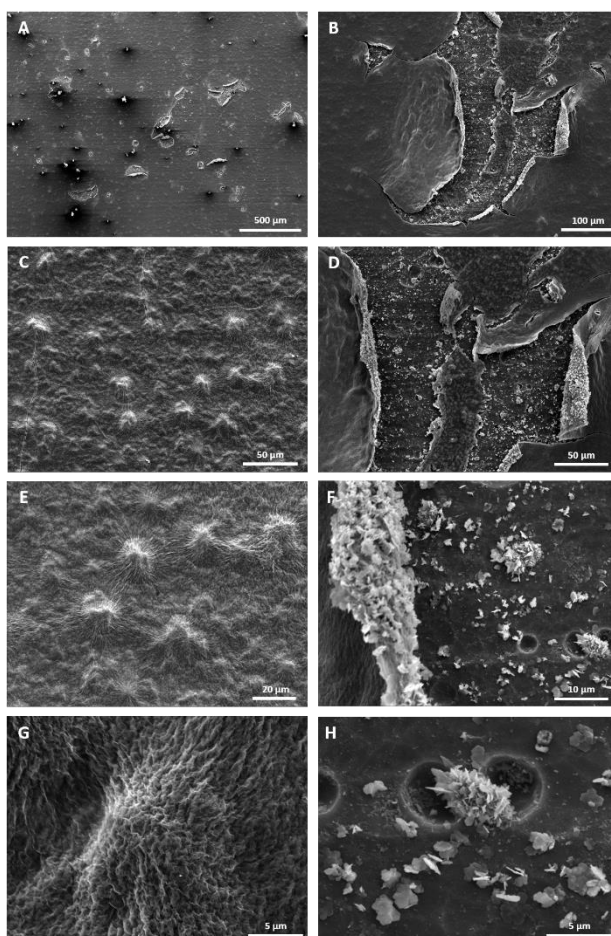


Figure A6 SEM images obtained for the LDH conversion film electrochemically deposited on a AA2024 substrate from a 12,5 mM $\text{Zn}(\text{NO}_3)_2$ solution (pH = 3). The deposition was carried out at -1,9 V vs Ag/AgCl, in RT conditions, during 5 min.

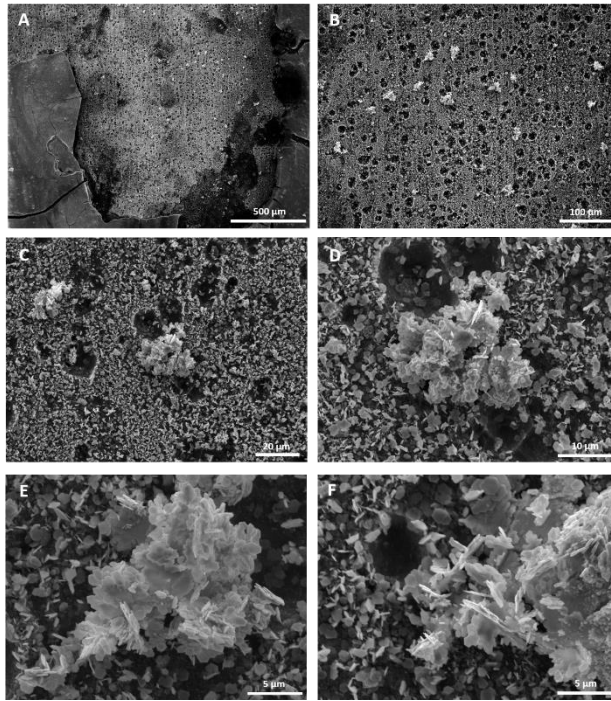


Figure A7 SEM images obtained for the LDH conversion film electrochemically deposited on a AA2024 substrate from a 12,5 mM $\text{Zn}(\text{NO}_3)_2$ solution (pH = 3). The deposition was carried out at - 1,9 V vs Ag/AgCl, in RT conditions, during 15 min.

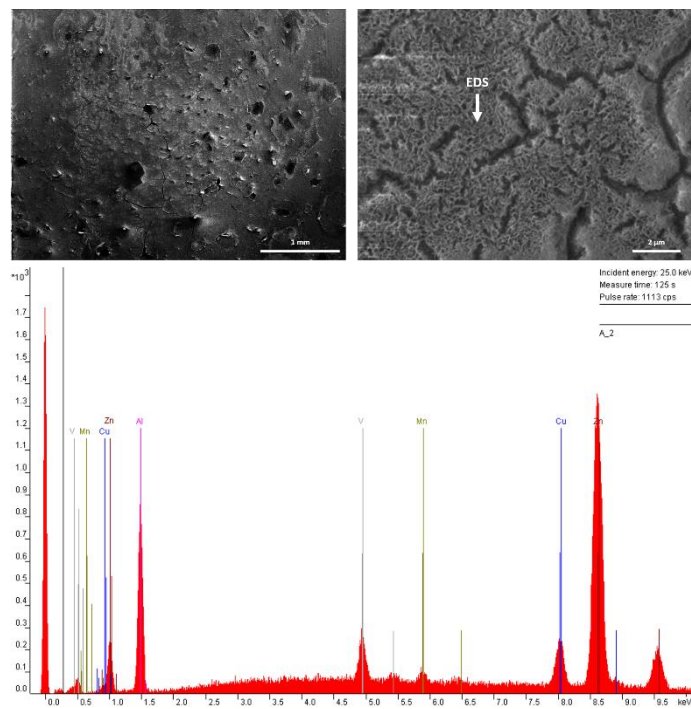


Figure A8 SEM/EDS data acquired for system LDH-ED-1/0.75.



Figure A9 Photograph taken after removal of the tape when performing the cross-cut test on system LDH-ED-1/0.75.